Young-Jin Park

Applications of Photonic Bandgap Structures with Arbitrary Surface Impedance to Luneburg Lenses for Automotive Radar

Foreword

Antennas in the millimeter wave range require a number of different considerations and exhibit constraints which we do not face at lower frequencies, for example in the mobile communication bands. The most severe problems are introduced by the increased losses and the thereby reduced efficiencies. Another problem is that millimeter wave antennas, especially if they require higher gain, are more conveniently considered with ray optical techniques. The usually most stringent problems are the involved cost because of the special materials and the high absolute precision. This, all together, leads to the task to avoid in millimeter waves antennas any dielectric materials, to reduce surface currents as much as possible and to develop a mechanical design that can be reproduced by casting and if required metallization of dielectric parts.

Dr. Park was able to handle these multiple problems in his PhD thesis extremely well. He uses a planar parallel-plate Luneburg Lens without any dielectric material. The wave propagation speed is influenced by quasi photonic bandgap structures, so called nail beds. These are shaped in a proper way to generate plane waves from cylindrical or spherical input waves. The design procedures are highly sophisticated but the final product is mass producable with specific casting procedures. The electrical parameters, for example beamforming, side lobes, losses and so on surpass anything presently available at millimeter waves. The antenna is applicable for multiple beams for example in automotive cruise control radars or for point to multi point communications.

I wish that the results of this thesis are wide spread in our community and that the ideas are realized in industrial products. We wish Dr. Park, who has been at our Institute as guest scientist from Korea, the best for his future carrier.

Prof. Dr.-Ing. Werner Wiesbeck
- Institutsleiter -

Institut für Höchstfrequenztechnik und Elektronik
der Universität Karlsruhe (TH)

Herausgeber: Prof. Dr.-Ing. Werner Wiesbeck

Band 1   Daniel Kähny
Modellierung und meßtechnische Verifikation polarimetrischer, mono-
und bistatischer Radarsignaturen und deren Klassifizierung

Band 2   Eberhardt Heidrich
Theoretische und experimentelle Charakterisierung der polarimet-
rischen Strahlungs- und Streueigenschaften von Antennen

Band 3   Thomas Kürner
Charakterisierung digitaler Funksysteme mit einem breitbandigen
Wellenausbreitungsmodell

Band 4   Jürgen Kehrbeck
Mikrowellen-Doppler-Sensor zur Geschwindigkeits- und Wegmessung
- System-Modellierung und Verifikation

Band 5   Christian Bornkessel
Analyse und Optimierung der elektrodynamischen Eigenschaften von
EMV-Absorberkammern durch numerische Feldberechnung

Band 6   Rainer Speck
Hochempfindliche Impedanzmessungen an Supraleiter / Festelektrolyt-
Kontakten

Band 7   Edward Pillai
Derivation of Equivalent Circuits for Multilayer PCB and Chip Package
Discontinuities Using Full Wave Models

Band 8   Dieter J. Cichon
Strahlenoptische Modellierung der Wellenausbreitung in urbanen
Mikro- und Pikofunkzellen

Band 9   Gerd Gottwald
Numerische Analyse konformer Streifenleitungsantennen in mehrla-
gigen Zylindern mittels der Spektralbereichsmethode

Band 10 Norbert Geng
Modellierung der Ausbreitung elektromagnetischer Wellen in Funk-
systemen durch Lösung der parabolischen Approximation der Helm-
holtz-Gleichung

**Institut für Höchstfrequenztechnik und Elektronik
der Universität Karlsruhe (TH)**

**Institut für Höchstfrequenztechnik und Elektronik
der Universität Karlsruhe (TH)**

**Institut für Höchstfrequenztechnik und Elektronik
der Universität Karlsruhe (TH)**

Band 33 Young-Jin Park
**Applications of Photonic Bandgap Structures with Arbitrary Surface
Impedance to Luneburg Lenses for Automotive Radar**

Band 34 Alexander Herschlein
**Entwicklung numerischer Verfahren zur Feldberechnung konformer
Antennen auf Oberflächen höherer Ordnung**

To my father and mother

Applications of Photonic Bandgap Structures with Arbitrary Surface Impedance to Luneburg Lenses for Automotive Radar

Zur Erlangung des akademischen Grades eines

DOKTOR-INGENIEURS

von der Fakultät für
Elektrotechnik und Informationstechnik
der Universität Fridericiana Karlsruhe

genehmigte

DISSERTATION

von

M.S. Young-Jin Park
aus Ma-San, Südkorea

Tag der mündlichen Prüfung:	08. Februar 2002
Hauptreferent:	Prof. Dr.-Ing. Werner Wiesbeck
Korreferent:	Prof. Dr. rer. nat. Manfred Thumm

Acknowledgments

14

Contents

Abbreviations and acronyms

1-D	one-dimensional
2-D	two-dimensional
ACC	Adaptive/Automatic/Autonomous Cruise Control
APWLL	Asymmetric Parallel-Plate Waveguide Luneburg Lens
BF	Beam Factor
CNC	Computer Numeric Control
EBG	Elcetromagnetic Bandgap
F	Fourier Transform
FEM	Finite Element Method
FMCW	Frequency Modulation Continuous Wave
GO	Geometrical Optics
HFSS	High Frequency Structure Simulator
HPBW	Half Power Beam Width
MBA	Multibeam Antenna
PBG	Photonic Bandgap
PEC	Perfect Magnetic Conductor
PMC	Perfect Magnetic Conductor
PPLL	Parallel-Plate Luneburg Lens
RADAR	RAdio Detection And Ranging
TE	Transverse Electric (to the wave propagation)
TEM	Transverse Electromagnetic (to the wave propagation)
TM	Transverse Magnetic (to the wave propagation)
TRM	Transverse Resonance Method
co-pol	copolarization
cross-pol	cross polarization
deg	Degree

List of symbols and variables

Mathematical notations

a , A	scalar real value
$\underline{a}$, $\underline{A}$	scalar complex value
$\vec{a}$, $\vec{A}$	vector scalar value
$\underline{\vec{a}}$, $\underline{\vec{A}}$	vector complex value
ja , jA	imaginary value
$\mathrm{Im}(\underline{A})$	imaginary part of $\underline{A}$
$\mathrm{Re}(\underline{A})$	real part of $\underline{A}$
$\hat{a}$	unit vector
$\sqrt{a}$, $\sqrt{A}$	square root of a and A
$a/A = \frac{a}{A}$	division
$A_1 \cdot A_2$	multiplication of two numbers
$A_1 \times A_2$	multiplication of two numbers
$\vec{A}_1 \cdot \vec{A}_2$	scalar (or dot) product
$\vec{A}_1 \times \vec{A}_2$	vector (or cross) product
$a \approx A$	approximation
$|a|, |A|$	absolute value
$e^{j\omega t}$	time factor
a° , A°	degree
∞	infinity
$\int \int (\cdot)$	double integration
A^+	forward-going wave or incident wave
A^-	backward-going wave or reflected wave
$\overleftarrow{A}_{x=a}$	the direction looking into the $-x$ direction at $x = a$
$\overrightarrow{A}_{x=a}$	the direction looking into the $+x$ direction at $x = a$

Greek letters

ω	angular frequency $\omega = 2\pi f$
ε, ε_i	permittivity of the medium i, $\varepsilon_i = \varepsilon_0 \varepsilon_{ri}$
ε_0	permittivity in free space
ε_r, ε_{ri}	dielectric constant of the medium i
μ, μ_i	permeability of the medium i, $\mu_i = \mu_0 \mu_{ri}$
μ_0	permeability of free space
μ_r, μ_{ri}	relative permeability of the medium i
λ	wavelength
λ_0	wavelength in free space
∇	vector differential operator *del*, $\nabla = \hat{x}\frac{\partial}{\partial x} + \hat{y}\frac{\partial}{\partial y} + \hat{z}\frac{\partial}{\partial z}$ in cartesian coordinates
∇^2	Laplacian operator *del* square, $\nabla^2 = \frac{\partial^2}{\partial x^2} + \frac{\partial^2}{\partial y^2} + \frac{\partial^2}{\partial z^2}$ in cartesian coordinates
$\underline{\Gamma}(\cdot)$	reflection coefficient
$\underline{\overrightarrow{\Gamma}}(y')$	reflection coefficient looking into the $+y$ direction at $y = y'$
$\underline{\overleftarrow{\Gamma}}(y')$	reflection coefficient looking into the $-y$ direction at $y = y'$
β	wave propagation constant of the medium
η_i	intrinsic wave impedance of the medium i
η_0	intrinsic wave impedance of free space
ϕ, θ	sperical coordinates
θ	scan angle
θ_i	angle of an incident wave
θ_t	angle of a transmitted wave
ρ	flare length of a H-plane sectoral horn in H-plane
ρ_e	flare length of a E-plane corrugated horn in E-plane
θ_e	flare angle of a E-plane corrugated horn in E-plane
α	a maximum scan angle in the offset reflector
θ_{HPBW}	half power beam width
$\theta_{10\,dB}$	angle at which the power of the feed radiates $10\,\text{dB}$ below from the feed direction

Latin letters

$\underline{\vec{A}}$	vector magnetic potential

$BF_{\text{sim:H}}$	Beam factor of the APWLL from the calculation in H-plane
C	a shunt capacitance per unit length in a transmission line
D	width of square metal posts
D	diameter of circular metal posts
D	thickness of corrugation
D_E	a maximum overall dimension
D_{a}	a projected cylindrical parabolic length
$\underline{E}_a(\zeta)$	electric field distribution of the real lens aperture
$\underline{E}_p(\zeta)$	electric field distribution of a primary feed of the lens
$\underline{E}$	electric field
$\vec{\underline{F}}$	vector electric potential
F	focal point
F	Fourier transform
G	gain
$\underline{H}$	magnetic field
$HPBW_{H°}$	half power beam width in H-plane in degree
$HPBW_{E°}$	half power beam width in E-plane in degree
$\underline{I}(\cdot)$	current wave in a transmission line
$\vec{\underline{J}}$	equivalent magnetic current
L	a series inductance per unit length in a transmission line
$\vec{\underline{M}}$	equivalent electric current
P	period of corrugation
P	period of square and circular metal posts
R_{F}	necessary minimum distance for far-field measurement, $R_{\text{F}} = \frac{2D_{\text{E}}^2}{\lambda_0}$
S_{11}, S_{21}	S parameters of a scattering matrix
$\underline{V}(\cdot)$	voltage wave in a transmission line
W	weighting factor
$\underline{Y}$	a shunt admittance per unit length in a transmission line
$\underline{Z}$	a series impedance per unit length in a transmission line
$\overrightarrow{\underline{Z}}(y')$	reflection coefficient looking into the $+y$ direction at $y = y'$
$\overleftarrow{\underline{Z}}(y')$	reflection coefficient looking into the $-y$ direction at $y = y'$
$\underline{Z}_0$	characteristic impedance of transmission line, $\underline{Z}_0 = \sqrt{L/C}$
$\underline{Z}_{\text{ISO}}$	surface impedance of metal post structure
$\underline{Z}_{\text{in}}$	input impedance
$\underline{Z}_{\text{in}}$	input wave impedance
$\underline{Z}_L$	a load impedance

$\underline{Z}_{\mathrm{PBG}}$	surface impedance of metal post structure with capacitive thin metal plates
$\underline{Z}_{\mathrm{TEi}}$	wave impedance of the TE wave in the medium i
$\underline{Z}_{\mathrm{TMi}}$	wave impedance of the TM wave in the medium i
a	spacing of a parallel-plate waveguide
a'	width of the aperture of a corrugated pyramidal horn
a_1	width of the aperture of a H-plane sectoral horn
b'	length of the aperture of a corrugated pyramidal horn
d	error distance between the feed horn and the lens
d	distance between the other plate and the surface of metal posts PBG structure
d_1	nearest distance between the lens and the offset cylindrical parabolic reflector
dI	differential increment of shunt current
f	frequency
f_0	resonance frequency
h	spacing of a parallel-plate waveguide
k_0	propagation constant of free space, $k_0 = 2\pi/\lambda_0 = \omega\sqrt{\mu_0/\varepsilon_0}$
k_i	propagation constant of the medium i
k_{xi}	transverse propagation constant of the medium i
l	distance from the load
l	length of the lens source
n	refraction index in a medium
$n(r')$	required refraction index for a Luneburg lens. r' is normalized radius of Luneburg lens.
$\hat{n}$	outward unit vector normal to the lens aperture
r_0	radius of a parallel-plate Luneburg lens
t	height of metal posts
t	height of a corrugated surface
$\mathrm{w}_{\mathrm{ref}}$	optimal reflector length

Constants

μ_0	permeability of free space, $\mu_0 = 4\pi \cdot 10^{-7}$ [H/m]
ε_0	permittivity of free space, $\varepsilon_0 = 1/(c^2\mu_0) \cong 8.854 \cdot 10^{-12}$ [F/m]
c	speed of light in free space $c = 1/\sqrt{\varepsilon_0\mu_0} \cong 3 \cdot 10^8$ [m/s]

η_0 intrinsic wave impedance, $\eta_0 = \sqrt{\mu_0/\varepsilon_0} = 120\pi$ $[\Omega]$

j $j = \sqrt{-1}$

Chapter 1

Introduction

1.1 Adaptive Cruise Control (ACC) Radar

Every year, car accidents will take away not only a great number of lives, but also damage property very much. For Germany alone, car accidents injured at least half million people seriously and about eight thousands of them lost their life last year [Sta01]. Up to the present, much effort has been given to reduce the damage of avoidable car accidents. Also many facilities such as the air bag have been developed and are available in market.

Recently, as a modern technique to diminish car accidents, an adaptive cruise control (ACC[1]) radar is receiving much attention in car industry. This ACC system is so valuable to be elected as a promising future technology in this century [Bre00]. The purpose of the radar is to help a car driver to drive his car safely by informing the car driver of the distance from his car to the vehicles ahead and its speed [Raf96], [Wen98], [Rob98]. Especially in conditions of poor visibility such as in dense fog or heavy rain, the ACC radar system is very helpful [Jon01].

In Fig. 1.1, an ACC radar system is displayed. In the system, three beams which are controlled electronically by three pin diodes are transmitted sequentially [Men99], [Wie01]. As is shown, the system is mostly mounted inside a car's front grille.

For the ACC system, a frequency band of 76-77 GHz has been allocated. Pulse radar or frequency modulation continuous wave (FWCW) radar are com-

---

[1] ACC is also called autonomous or automatic cruise control.

Figure 1.1: An ACC radar system at 76-77 GHz in Mercedes Benz S-Class models. Courtesy by A.D.C. GmbH.

monly used [Sko80], [Mei95], [Wol97].

In an ACC radar system, one of the most important components is the antenna. The antenna should have at least three beams to detect targets ahead in front lanes. Further, each beam has a narrow half power beam width to support a sufficient resolution for the detection of targets ahead in each lane [All98], [Sch98], [Wie01]. In the vertical plane perpendicular to the lanes (road), a medium-high resolution should be achieved. Since the size of the antenna dominates the overall system size, the antenna should be compact in order to be mounted inside a car's front grille. Also, it should be robust against the outer impact. Moreover, for public usage as a future system, the cost of the antenna should be low. In addition, several unexpected and unusual problems of antennas which happen in millimeter wave frequencies, not in microwave frequencies should be considered.

Unfortunately, due to the above special and hard specifications of the ACC radar, conventional antennas such as low-cost microstrip antennas and classical reflector antennas are inappropriate to be directly applied. In other words, new antenna concepts dedicated to the special purpose of the 76-77 GHz ACC radar are required.

The motivation of this thesis is to develop a proper antenna for the ACC radar at 76.5 GHz which meets the above requirements.

1.2 Scope and purpose of the thesis

1.2.1 Proposal of parallel-plate Luneburg lens

In this thesis, a new modified and improved parallel-plate Luneburg lens (PPLL) is proposed to make a new antenna for the 76.5 GHz ACC radar.

In many cases, a spherical Luneburg lens has been used for a circular polarization and a high resolution both in azimuth and in elevation [Sch95], [Par00a], [Atn01]. However, the spherical Luneburg lens has some disadvantages such as its difficult fabrication and large size [Ing97], [Kim98], [Mos01]. Until now, several suggestions have been offered for a size reduction and easy fabrication. For the reduction of lens size, for example, a virtual-source Luneburg lens was proposed [Rud62], [Han64], [Sch95]. However, the problem of easy fabrication still is not solved.

In some applications like the ACC radar [Sch98], [Wen98], [Per99] and short- and medium-range high resolution imaging [Vog82] the system requires a high resolution only in azimuth together with a linear polarization, a low cost production, and a compact size. Due to large size and complicated fabrication, the spherical Luneburg lens is unsuitable in spite of several well-matched characteristics.

Therefore we consider a parallel-plate Luneburg lens (PPLL) shown in Fig. 1.2. This is also called a TEM flat-plate Luneburg lens [Cul55], [Han64]. Figure 1.2(a) illustrates the top view and the behavior of the rays for the center feed denoted by feed II in azimuth of the PPLL. As shown in Fig. 1.2(b), in the PPLL a homogeneous isotropic dielectric is embedded and the thickness of the dielectric is varied in a radial direction. Using the dielectric in the lens, the lens converts a cylindrical wave from a primary feed into a plane wave at the aperture. Since the PPLL is completely rotationally symmetric, it has the property of a wide beam scan angle as shown in Fig. 1.2(a). Also, since the spacing between two plates is usually less than $\lambda_0/2$, it has a very thin profile. Thus, this lens is considered as a promising device for use in wide angle scanning applications which require a thin lens [Han64]. Furthermore, its fabrication is much easier than the spherical Luneburg lens since it uses only a homogeneous isotropic dielectric for the inhomogeneous profile in the lens (see the dielectric profile in Fig. 1.2(b)).

However, the lens in Fig. 1.2 is practically difficult to realize due to an insufficient durability and a weak contact at the interface between dielectric and metal in millimeter wave frequencies. Also, the PPLL has a rather poor performance in elevation. In [Joh62], [Han64] and [Vog82], the dual reflector and
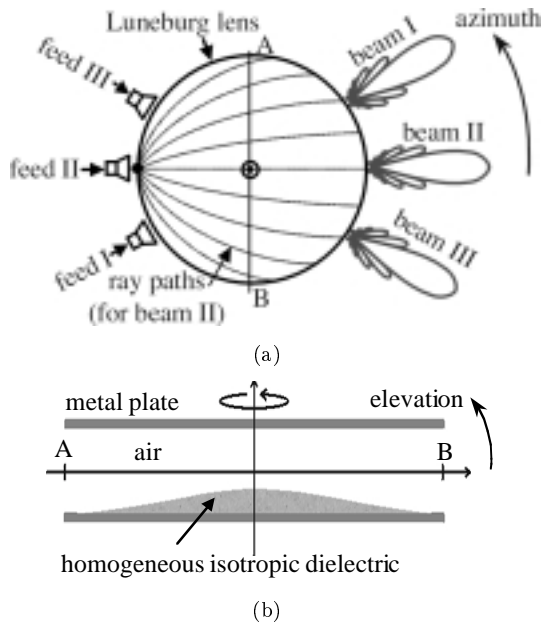
Figure 1.2: (a) Top view of a PPLL and illustration of the behavior of a wide scan angle. (b) Cross-sectional view.

the plane flares were applied to overcome the limitation in elevation. But the dual reflector system seems to be too complex and sensitive for the ACC radar application and the plane flares gave little improvement. Up to the present, these critical drawbacks have hindered the application of the PPLL.

Here, with the help of modified one-dimensional (1-D) and two-dimensional (2-D) corrugated structures, which we call metallic photonic bandgap (PBG) structures, the above problems will be solved.

1.2.2 PBG structures and parallel-plate Luneburg lens

The terminology of the photonic bandgap (PBG[2]) is described as a frequency band in which no photon modes in optics are allowed. In optics, Yablonovitch

---

[2]Since key physical ideas and general features of PBG structures within PBGs are common to those of electromagnetic waves, the term of PBG is commonly used in electromagnetics as well. However, some authors call the term of PBG electromagnetic bandgap (EBG) at microwave frequencies [Smi93], [Shu99], [Bar01].

[Yab87] reported for the first time that photons in periodic structures have forbidden bands such as electrons in solids. The periodic structures where PBGs exist are called photonic crystals or PBG structures. Up to now, a number of publications have appeared [JOS93], [Joa95], [Sou96], [Pho02]. Also, as operating frequencies of PBG structures move to microwave and millimeter wave frequencies, the applications of the PBG structures have been widely extended [MTT99], [MTT01].

Figure 1.3(a) shows a periodic structure composed of regular and periodic metal posts with thin metal plates. Figure 1.3(b) shows the surface imped-ance of the periodic structure. It shows that the structure has high surface impedance near the resonance frequency f_0, so that the periodic structure is called high-impedance electromagnetic surface [Sie99]. Since no surface waves can match high surface impedance of the structure, the high-impedance sur-face prevents surface waves from propagating along the material and hence this frequency range is called a forbidden band for surface waves. Thus, this high-impedance surface can be considered as a kind of 2-D photonic crystal (PBG structure) which stops the propagation of surface waves within the bandgap [Sie99]. In antenna applications, the property of high surface impedance helps to suppress surface waves which often influence the antenna performance and cause unwanted mutual coupling [Bro93], [Sie99], [Gon99]. In this thesis, the property of high impedance is applied to build rotationally corrugated flares of the PPLL and then the shortcomings of the PPLL in elevation are overcome.

In addition to the property of high surface impedance near f_0, this kind of PBG structure has the property of having arbitrary surface impedances at lower and higher frequencies than f_0 as displayed in Fig. 1.3(b). This means that PBG structures offer electromagnetic properties of dielectrics and act hence as artificial dielectrics.

In antenna design, the property of supporting arbitrary surface impedance is often used to guide surface waves [Wal65], [Ell81]. Therefore, using PBG materials, very compact and low profile surface-wave or traveling-wave antennas can be designed. In this thesis, the property of the metallic PBG structure is applied to make an asymmetric parallel-plate waveguide Luneburg lens by replacing a homogeneous isotropic dielectric. Therefore, the problems of the dielectric in the PPLL are solved.

The purposes of the thesis are as follows:

- to present and analyze metallic PBG structures having arbitrary surface impedance, especially in a parallel-plate waveguide.
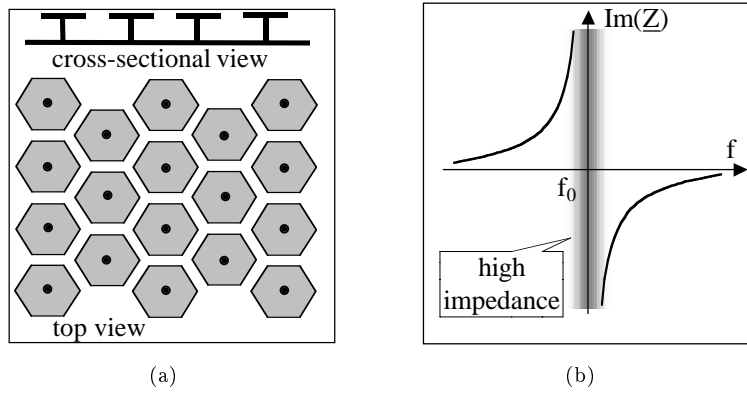
Figure 1.3: (a) High-impedance electromagnetic surface presented by Sievenpiper, et al. [Sie99]. (b) Illustration of the property of high impedance in the forbidden band and supporting arbitrary surface impedance at lower and higher than f_0. $\underline{Z}$ is surface impedance of the structure.

- to show a practical application of metallic PBG structures to a modified and improved parallel-plate Luneburg lens, called an asymmetric parallel-plate waveguide Luneburg lens (APWLL) antenna composed of an APWLL and rotationally symmetric corrugated flares.

- to propose a single offset cylindrical parabolic reflector antenna composed of the APWLL, a pair of symmetric corrugated flares, and a single offset cylindrical parabolic reflector for a 76.5 GHz ACC radar.

1.3   Outline of the thesis

This thesis is divided into three parts in terms of its main ideas. The first part deals with the theoretical background of the analysis of PBG materials. Ch. 2 belongs to this part. The second part is about the analysis of two metallic PBG structures and their application to the APWLL antenna, Ch. 3 and Ch. 4 are devoted to this part. The third part introduces the numerical and experimental verification and optimization for the ACC radar at 76.5 GHz.

In Ch. 2, first, the analogy of the transmission line theory for plane waves is introduced and then it is shown that many useful results of transmission line theory can directly be used to obtain the surface impedance and the reflection coefficients for the plane wave problems. Second, the transverse resonance

condition is introduced and the important expressions of the condition about wave impedance and reflection coefficient are derived. Third, the transverse resonance method (TRM) is applied to find the propagation constants in multilayer dielectrics. At the same time, some useful equations are derived for the analysis of the PBG structures used in Ch. 3.

In Ch. 3, metallic PBG structures of a corrugated surface, periodic and regular metal post structures, and modified *bed-of-nail* structures are investigated. The quantitative and qualitative analyses of the above PBG structures in a parallel-plate waveguide are performed. It will be shown that the PBG structures have not only high surface impedances in forbidden bands, but they also have theoretically any surface impedance in the passband for guiding surface waves. The TRM derives the transverse propagation constants for the surface waves.

In Ch. 4, the above PBG structures are applied to make an APWLL antenna. It will be shown that a periodic and regular metal post structure can substitute the homogeneous isotropic dielectric in the PPLL. A corrugated surface is used for a rotationally symmetric flare to enhance the performance of the APWLL in elevation. For the design of the APWLL and the corrugated flares, their far fields are derived with the aid of geometrical optics (GO) and the aperture field integration method. Also, design procedures of the corrugated flares and the APWLL are described in detail.

In Ch. 5, a prototype APWLL antenna for the 76-77 GHz ACC radar is presented. As far as the corrugated flares are concerned, a pair of the rotationally symmetric corrugated flares is designed for the APWLL. In order to determine the proper dimensions of the APWLL and the flares for a desired pattern, their far fields are computed at 76.5 GHz. With the help of HFSS[3], APWLLs composed of different lattices and metal posts are investigated and then proper post dimensions, post shapes, and lattices are determined. By measurement, the theory and the design procedure are verified. At the end, the limitation of the corrugated flares will be shortly discussed for a desired narrower half power beam width (HPBW).

In Ch. 6, the APWLL antenna with the corrugated flares is improved by combining an offset cylindrical parabolic reflector and a pair of symmetric corrugated flares. Using GO, the far field of the reflector is obtained. Then, the optimization of the reflector and the the corrugated extension is conducted for the ACC radar application. Design procedures of the complete antenna are described and verified by measurement. It will be seen that the usage of

---

[3] HFSS version 2.0.55, Ansoft corporation, Pittsburgh, 1999.

the reflector makes the complete antenna clearly compact, simultaneously a medium-high resolution is achieved.

In Ch. 7, the thesis is summarized. Some comments on further works are made, especially about mass production and new applications of the new antenna.

Chapter 2

Transmission line theory and transverse resonance method (TRM)

In this chapter, two useful analysis methods are described. The first is about transmission line theory for a plane wave using the analogy between a transmission line and a plane wave. The second is the transverse resonance method for computing the transverse propagation constant in a composite structure. The time factor of $e^{j\omega t}$ is suppressed throughout the thesis.

2.1 Transmission line theory for a plane wave

2.1.1 Wave propagation on a transmission line

A transmission line is a distributed-parameter network, where voltages and currents can vary in magnitude and phase over its geometrical dimension. It is analyzed from the point of view of field analysis and the point of view of lumped circuit concept [Har61], [Chr95], [Ra96].

In Fig. 2.1, a two-wire lossless transmission line terminated by a load impedance $\underline{Z}_L$ at $z = 0$ and its lumped equivalent circuit model are displayed. $\underline{Z}_0$ is the characteristic impedance of the transmission line and β is the propagation constant of a wave supported by the line. Assuming that a) no mutual impedance exists between incremental sections of the line and b) the shunt

9
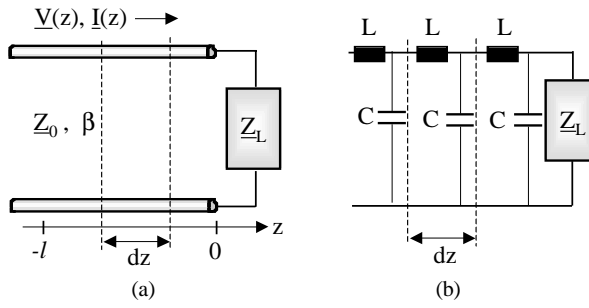
Figure 2.1: (a) A physical two-wire lossless transmission line terminated in a load impedance $\underline{Z}_L$. (b) Lumped equivalent circuit model.

current dI flows in planes transverse to the z-directed wave propagation, the one-dimensional Helmholtz equations of a voltage wave $\underline{V}(z)$ and a current wave $\underline{I}(z)$ for a uniform transmission line are obtained as follows:

$$\frac{d^2\underline{V}(z)}{dz^2} - \underline{Z}\,\underline{Y}\,\underline{V}(z) = 0 \tag{2.1a}$$

$$\frac{d\underline{I}^2(z)}{dz^2} - \underline{Z}\,\underline{Y}\,\underline{I}(z) = 0 \tag{2.1b}$$

where

$\underline{Z} = j\omega L$ \qquad a series impedance per unit length

L \qquad a series inductance per unit length

$\underline{Y} = j\omega C$ \qquad a shunt admittance per unit length

C \qquad a shunt capacitance per unit length.

The equation is analogous to the Helmholtz equation for a plane wave. The general wave solution of Eq. (2.1) is

$$\underline{V}(z) = \underline{V}_0^+ e^{-j\beta z} + \underline{V}_0^- e^{j\beta z} \tag{2.2}$$

where $\beta = \omega\sqrt{LC}$ is the eigenvalue of the differential operator. From the relation $\frac{d\underline{V}(z)}{dz} - \underline{Z}\,\underline{I}(z) = 0$ obtained by the lumped circuit model in Fig. 2.1(b), the current wave in the transmission line is

$$\underline{I}(z) = \underline{I}_0^+ e^{-j\beta z} + \underline{I}_0^- e^{j\beta z} = \frac{\underline{V}_0^+}{\underline{Z}_0} e^{-j\beta z} - \frac{\underline{V}_0^-}{\underline{Z}_0} e^{j\beta z} \tag{2.3a}$$

where $\underline{Z}_0$ is a characteristic impedance defined as

$$\underline{Z}_0 \quad = \quad \frac{V_0^+}{\underline{I}_0^+} = -\frac{V_0^-}{\underline{I}_0^-}$$

$$= \quad \sqrt{\frac{L}{C}}. \tag{2.3b}$$

As shown in Eq. (2.2) and Eq. (2.3a), the whole waves are composed of a forward propagating wave, $\underline{V}_0^+ e^{-j\beta z}$ that travels in the $+z$ direction and a backward propagating wave, $\underline{V}_0^- e^{+j\beta z}$ that travels in the $-z$ direction due to the mismatch of two impedances $\underline{Z}_L \neq \underline{Z}_0$.

From $\underline{Z}_L = \underline{V}(z)/\underline{I}(z)|_{z=0}$, the voltage reflection coefficient $\underline{\Gamma}(0)$ at $z = 0$ is derived as

$$\underline{\Gamma}(0) = \frac{V_0^-}{\underline{V}_0^+} = \frac{\underline{Z}_L - \underline{Z}_0}{\underline{Z}_L + \underline{Z}_0}. \tag{2.4}$$

Eq. (2.2) and Eq. (2.3a) are rewritten in terms of $\underline{\Gamma}(0)$ using Eq. (2.4). The result is

$$\underline{V}(z) \quad = \quad \underline{V}_0^+ (e^{-j\beta z} + \underline{\Gamma}(0)e^{j\beta z}) \tag{2.5a}$$

$$\underline{I}(z) \quad = \quad \frac{V_0^+}{\underline{Z}_0}(e^{-j\beta z} - \underline{\Gamma}(0)e^{j\beta z}). \tag{2.5b}$$

These equations show that if knowing the reflection coefficient at $z = 0$, the voltage and the current on the transmission line at any distance $z = -l\,(l \geq 0)$ are obtained. Thus, the input impedance looking toward the load $\underline{Z}_L$ can be derived at a distance $z = -l$. The result is

$$\underline{Z}_{\text{in}} = \frac{\underline{V}(-l)}{\underline{I}(-l)} = \underline{Z}_0 \frac{1 + \underline{\Gamma}(0)e^{-2j\beta l}}{1 - \underline{\Gamma}(0)e^{-2j\beta l}}. \tag{2.6}$$

Using Eq. (2.4), Eq. (2.6) leads to a very important result referred to as the transmission line impedance equation. That is,

$$\underline{Z}_{\text{in}} = \underline{Z}_0 \frac{\underline{Z}_L + j\underline{Z}_0 \tan \beta l}{\underline{Z}_0 + j\underline{Z}_L \tan \beta l}. \tag{2.7}$$

Eq. (2.7) is a very useful result giving the input impedance of a transmission line of length l with the characteristic impedance $\underline{Z}_0$ and the load $\underline{Z}_L$. It is very often used for impedance matching design using a transmission line [Poz93], [Chr95].

In the following section, it is shown that the equations derived in this section can be true to the plane wave.

2.1.2 Transmission line analogy for plane waves
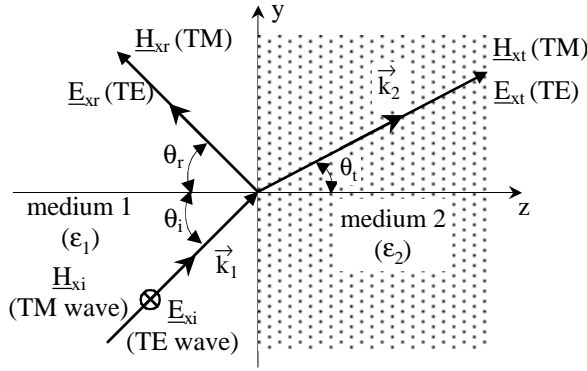
Figure 2.2: Reflected wave ($\underline{E}_{xr}$ for TE wave and $\underline{H}_{xr}$ for TM wave) and transmitted wave ($\underline{E}_{xt}$ and $\underline{H}_{xt}$) on the interface of two different media for the oblique incident uniform plane wave ($\underline{E}_{xi}$ and $\underline{H}_{xi}$).

In Fig. 2.2, a uniform plane wave is obliquely incident on a plane interface between two media. Since the oblique incident wave is uniform, the transmitted and reflected wave are also uniform [Har61], [Ish91], [Gen98]. The Helmholtz equations for the electric field $\underline{E}$ and the magnetic field $\underline{H}$ in source free and homogeneous mediums are given as

$$\nabla^2 \underline{E} + k_i^2 \underline{E} = 0 \tag{2.8a}$$
$$\nabla^2 \underline{H} + k_i^2 \underline{H} = 0 \tag{2.8b}$$

where $\nabla^2 = \frac{\partial^2}{\partial x^2} + \frac{\partial^2}{\partial y^2} + \frac{\partial^2}{\partial z^2}$ and $k_i^2 = \omega^2 \mu_i \varepsilon_i$ for $i = 1,2$.

First, we consider the case of the electric field parallel to the interface, called TE wave (transverse electric wave), that is, $\frac{\partial^2}{\partial x^2} \underline{E}_{xi} = 0$. By a separation of variables, the general solution of Eq. (2.8) in medium 1 is

$$
\begin{aligned}
\underline{E}_{x1}(y,z) &= \underline{E}_{xi} + \underline{E}_{xr} \\
&= \underline{E}_{x1}^{+} e^{-jk_{y1}y - jk_{z1}z} + \underline{E}_{x1}^{-} e^{-jk_{y1}y + jk_{z1}z}
\end{aligned}
\tag{2.9a}
$$

where

$$
\begin{aligned}
k_1 &= \omega \sqrt{\mu_1 \varepsilon_1} \\
k_{y1} &= k_1 \sin \theta_i \\
k_{z1} &= k_1 \cos \theta_i = \sqrt{k_1^2 - k_{y1}^2}.
\end{aligned}
\tag{2.9b}
$$

Using Maxwell's curl equation, $\vec{H} = \frac{-1}{j\omega\mu}\nabla \times \vec{E}$, the magnetic field $\vec{H}$ is derived as

$$
\begin{aligned}
\underline{H}_{y1}(y,z) &= \underline{H}_{y1}^{+}e^{-jk_{y1}y-jk_{z1}z} + \underline{H}_{y1}^{-}e^{-jk_{y1}y+jk_{z1}z} \\
&= \frac{\cos\theta_i}{\eta_1}(\underline{E}_{x1}^{+}e^{-jk_{y1}y-jk_{z1}z} - \underline{E}_{x1}^{-}e^{-jk_{y1}y+jk_{z1}z}) \quad (2.10a) \\
\underline{H}_{z1}(y,z) &= -\frac{\sin\theta_i}{\eta_1}(\underline{E}_{x1}^{+}e^{-jk_{y1}y-jk_{z1}z} + \underline{E}_{x1}^{-}e^{-jk_{y1}y+jk_{z1}z}) \quad (2.10b)
\end{aligned}
$$

where $\eta_1 = \sqrt{\mu_1/\varepsilon_1}$ is the intrinsic wave impedance of the medium 1. As is shown in Eqs. (2.9) and (2.10), both of the electric field $\underline{E}$ and the magnetic field $\underline{H}$ in the medium 1 are composed of an incident wave with the term $\underline{E}_{x1}^{+}$ and a reflected wave with the term $\underline{E}_{x1}^{-}$, respectively such as the solutions of the voltage and current waves in Eq. (2.5).

In the same way, the solution in medium 2 is

$$
\begin{aligned}
\underline{E}_{x2}(y,z) &= \underline{E}_{xt} = \underline{E}_{2}^{+}e^{-jk_{y2}y-jk_{z2}z} && (2.11a) \\
\underline{H}_{y2}(y,z) &= \frac{\cos\theta_t}{\eta_2}\underline{E}_{2}^{+}e^{-jk_{y2}y-jk_{z2}z} && (2.11b) \\
\underline{H}_{z2}(y,z) &= -\frac{\sin\theta_t}{\eta_2}\underline{E}_{2}^{+}e^{-jk_{y1}y-jk_{z2}z} && (2.11c)
\end{aligned}
$$

where

$$
\begin{aligned}
k_2 &= \omega\sqrt{\mu_2\varepsilon_2} \\
k_{y2} &= k_2\sin\theta_t \\
k_{z2} &= k_2\cos\theta_t = \sqrt{k_2^2 - k_{y2}^2} \\
\eta_2 &= \sqrt{\mu_2/\varepsilon_2}. && (2.11d)
\end{aligned}
$$

We consider the wave impedance in the direction determined by the cross-product rule applied to a tangential electric field and a tangential magnetic field. The wave impedance is defined as the ratio of the tangential electric field to the tangential magnetic field. Thus, the wave impedance of the TE wave in the $+z$ direction in the medium 1 is

$$
\underline{Z}_{\text{TE1}} = \frac{\underline{E}_{x1}^{+}}{\underline{H}_{y1}^{+}} = \frac{\eta_1}{\cos\theta_i}. \quad (2.12a)
$$

Similarly, the wave impedance in the medium 2 is expressed as

$$\underline{Z}_{\text{TE2}} = \frac{\underline{E}_{x2}^+}{\underline{H}_{y2}^+} = \frac{\eta_2}{\cos\theta_t}. \qquad (2.12b)$$

In Fig. 2.3, the equivalent circuit of the plane wave problem in Fig. 2.2 is displayed.

$\underline{E}_x(y, z)$, $\underline{H}_x(y, z) \longrightarrow$

$\underline{Z}_{\text{TE1}}$, k_{z1}

$\underline{Z}_{\text{TM1}}$, k_{z1}

$\underline{Z}_{\text{TE2}}$
$\underline{Z}_{\text{TM2}}$

z=-l

0

z
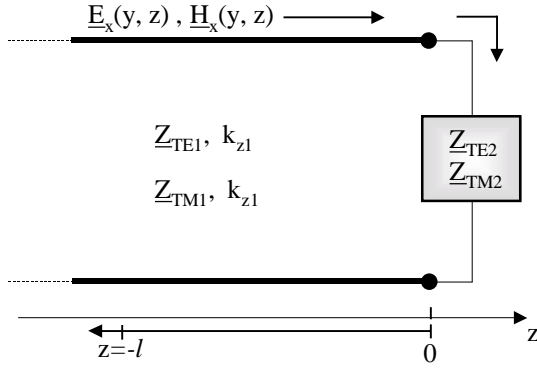
Figure 2.3: Equivalent circuit of the uniform plane wave problem in Fig. 2.2. For the TE wave case, the total electric field is $\underline{E}_x(y,z)$ in the medium 1 and the wave impedances are $\underline{Z}_{\text{TE1}}$ and $\underline{Z}_{\text{TE2}}$ in each medium. For the TM wave case, $\underline{H}_x(y,z)$ and $\underline{Z}_{\text{TM1}}$ and $\underline{Z}_{\text{TM2}}$.

It is true that due to the continuity of the tangential electric field $\underline{E}_{x1} = \underline{E}_{x2}$ and the tangential magnetic field $\underline{H}_{y1} = \underline{H}_{y2}$, the wave impedances normal to an interface at $z = 0$ should be continuous. From Eq. (2.9) and Eq. (2.10a),

$$\frac{\underline{E}_{x1}(y,0)}{\underline{H}_{y1}(y,0)} = \underline{Z}_{\text{TE1}} \frac{\underline{E}_{x1}^+ + \underline{E}_{x1}^-}{\underline{E}_{x1}^+ - \underline{E}_{x1}^-} \qquad (2.13a)$$

$$\frac{\underline{E}_{x2}(y,0)}{\underline{H}_{y2}(y,0)} = \underline{Z}_{\text{TE2}}. \qquad (2.13b)$$

Therefore, the continuity of the two impedances results in

$$\underline{Z}_{\text{TE2}} = \underline{Z}_{\text{TE1}} \frac{\underline{E}_{x1}^+ + \underline{E}_{x1}^-}{\underline{E}_{x1}^+ - \underline{E}_{x1}^-}. \qquad (2.13c)$$

Now, the reflection coefficient at $z = 0$ is defined as the ratio of the reflected electric field $\underline{E}_{x1}^-$ to the incident electric field $\underline{E}_{x1}^+$ at the interface $z = 0$. From

Eq. (2.13c), the reflection coefficient $\underline{\Gamma}(0)$ looking into the medium 2 at $z = 0$ is derived as

$$\underline{\Gamma}(0) = \frac{\underline{E}_1^-}{\underline{E}_1^+} = \frac{\underline{Z}_{\text{TE2}} - \underline{Z}_{\text{TE1}}}{\underline{Z}_{\text{TE2}} + \underline{Z}_{\text{TE1}}}. \tag{2.14}$$

Note that the above result for $\underline{\Gamma}(0)$ is the same as the one of the transmission line problem given by Eq. (2.4) previously if letting $\underline{Z}_{\text{TE1}} = \underline{Z}_0$ and $\underline{Z}_{\text{TE2}} = \underline{Z}_L$. By combining $\underline{\Gamma}(0)$ with Eq. (2.9) and Eq. (2.10a), the solutions of $\underline{E}_{x1}(y,z)$ and $\underline{H}_{y1}(y,z)$ in Eqs. (2.9) and (2.10a) are rewritten as

$$\underline{E}_{x1}(y,z) = \underline{E}_1^+ (e^{-jk_{y1}y - jk_{z1}z} + \underline{\Gamma}(0)e^{-jk_{y1}y + jk_{z1}z}) \tag{2.15a}$$

$$\underline{H}_{y1}(y,z) = \frac{\underline{E}_1^+}{\underline{Z}_{\text{TE1}}}(e^{-jk_{y1}y - jk_{z1}z} - \underline{\Gamma}(0)e^{-jk_{y1}y + jk_{z1}z}). \tag{2.15b}$$

Similar to the transmission line problem, Eq. (2.15) is used to define a generalized input wave impedance $\underline{Z}_{\text{in}}$ of a plane wave traveling in the $+z$ direction. At $z = -l$, this is given by:

$$\underline{Z}_{\text{in}}(z = -l) = \frac{\underline{E}_{x1}(y, -l)}{\underline{H}_{y1}(y, -l)} = \underline{Z}_{\text{TE1}}\frac{1 + \underline{\Gamma}(-l)}{1 - \underline{\Gamma}(-l)} \tag{2.16}$$

where $\underline{\Gamma}(-l) = \underline{\Gamma}(0)e^{-j2k_{z1}l}$ is the reflection coefficient at $z = -l$. In Eq. (2.14), $\underline{\Gamma}(0)$ is given in terms of the two wave impedances $\underline{Z}_{\text{TE1}}$ and $\underline{Z}_{\text{TE2}}$ in each medium. Thus,

$$\underline{Z}_{\text{in}}(z = -l) = \underline{Z}_{\text{TE1}}\frac{\underline{Z}_{\text{TE2}} + j\underline{Z}_{\text{TE1}}\tan(k_{z1}l)}{\underline{Z}_{\text{TE1}} + j\underline{Z}_{\text{TE2}}\tan(k_{z1}l)}. \tag{2.17}$$

For the case of the magnetic field parallel to the interface, called TM wave (transverse magnetic), the equations are obtained in the same way as the case of TE wave. Therefore, the derivation of these equations is left out and only the final results are shown. For the TM case, the input wave impedance at any distance $z = -l$ is

$$\underline{Z}_{\text{in}}(z = -l) = \underline{Z}_{\text{TM1}}\frac{\underline{Z}_{\text{TM2}} + j\underline{Z}_{\text{TM1}}\tan(k_{z1}l)}{\underline{Z}_{\text{TM1}} + j\underline{Z}_{\text{TM2}}\tan(k_{z1}l)} \tag{2.18a}$$

with

$$\begin{aligned}\underline{Z}_{\text{TM1}} &= \eta_1 \cos\theta_i \\ \underline{Z}_{\text{TM2}} &= \eta_1 \cos\theta_t.\end{aligned} \tag{2.18b}$$

It is necessary to note that with $\theta_i = 0°$, $\underline{Z}_{\mathrm{TE1}}$ is minimum while $\underline{Z}_{\mathrm{TM1}}$ is maximum and is identical with the intrinsic wave impedance of the medium 1.

In the following section, two equations for the input wave impedance, Eq. (2.17) and Eq. (2.18) are often used while applying the transverse resonance method.

2.2 Transverse resonance method (TRM)

The transverse resonance method (TRM) is often used to determine the modes propagating in composite waveguide structures [Mar51], [Col91]. Also, in [Wal65], the method is applied to design traveling-wave antennas. In the following sections, the principle of the method and several applications are presented. Furthermore, several important and useful equations for the analysis of PBG structures that are presented in Ch. 3 are derived from the TRM.

2.2.1 Transverse resonance condition

First, in order to explain the transmission resonance phenomenon, consider a parallel-plate waveguide depicted in Fig. 2.4. The waveguide is filled with a lossless and homogeneous medium (μ, ε). It is assumed that the wall of the waveguide is a perfect electric conductor (PEC).
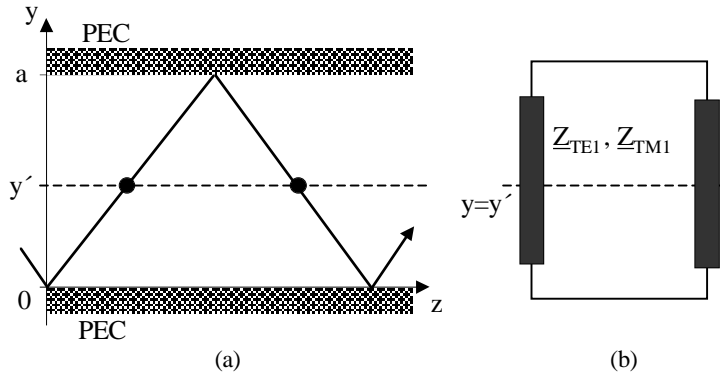
Figure 2.4: (a) A parallel-plate waveguide and (b) its transmission line equivalent circuit. $\underline{Z}_{\mathrm{TM1}}$ and $\underline{Z}_{\mathrm{TE1}}$ denote wave impedances for the TM wave and the TE wave, respectively.

In order to obtain the electric field for the TE wave (transverse electric wave to the z-directed wave propagation), the Helmholtz equations in Eq. (2.8a) is referred to. By applying the radiation boundary condition in the $+z$ direction, the electric field is given as the superposition of mode functions:

$$\underline{E}_x(y,z) = \sum_{m=1,2,\ldots} e^{-jk_{zm}z}(\underline{E}_m^+ e^{-jk_{ym}y} + \underline{E}_m^- e^{+jk_{ym}y}) \qquad (2.19a)$$

with

$$k_{zm} = \sqrt{k_1^2 - k_{ym}^2} \quad \text{and} \quad k_1 = \omega\sqrt{\mu\varepsilon}. \qquad (2.19b)$$

The terms of $\underline{E}_m^+ e^{-jk_{ym}y}$ and $\underline{E}_m^- e^{-jk_{ym}y}$ are waves which travel in the $+y$ and the $-y$ direction, respectively. Now, by applying the boundary conditions of $\underline{E}_x(y=0,z) = \underline{E}_x(y=a,z) = 0$, Eq. (2.19a) is

$$
\begin{aligned}
\underline{E}_x(y,z) &= \sum_{m=1,2,\ldots} \underline{E}_m^+ (e^{-jk_{ym}y} - e^{+jk_{ym}y})e^{-jk_{zm}z} \\
&= -\sum_{m=1,2,\ldots} 2j\underline{E}_m^+ \sin(k_{ym}y)e^{-jk_{zm}z} \qquad (2.20)
\end{aligned}
$$

where $k_{ym} = (m\pi)/a$ is the transverse propagation constant or the eigenvalue of the m-th mode function in the y direction. Note that standing waves $\sin(k_{ym}y)$ exist in transverse direction, the y direction and the medium is lossless. Thus, by self-reproduction, electromagnetic fields have the same amplitude and phase at $y = y'$ [Ra96]. In other words, the forward wave which returns to $y = y'$ through the path $y = y' \Rightarrow y = a \Rightarrow y = 0 \Rightarrow y = y'$ is identical with the original forward wave at $y = y'$. It is said that a resonance in the transverse direction occurs, especially, this phenomenon is called the transverse resonance.

In Fig. 2.5, the path of the forward wave and its equivalent model are displayed. The equivalent values of the paths are

1) $= e^{-jk_{my}(a-y)} =$ traveling from $y = y'$ to $y = a$
2) $= \overrightarrow{\Gamma}_m(a) =$ reflection coefficient looking into the $+y$ direction at $y = a$
3) $= e^{-jk_{my}a} =$ traveling from $y = a$ to $y = 0$
4) $= \overleftarrow{\Gamma}_m(0) =$ reflection coefficient looking into the $-y$ direction at $y = 0$
5) $= e^{-jk_{my}y'} =$ traveling from $y = 0$ to $y = y'$.

Using Eq. (2.14), $\overrightarrow{\Gamma}_m(a) = -1$ and $\overleftarrow{\Gamma}_m(0) = -1$ are simply obtained due to
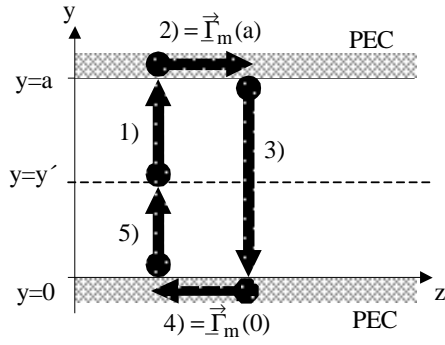
Figure 2.5: The path of the forward wave and its equivalent model.

$\underline{Z}_{\text{TE2}} = 0$. Now the forward wave traveling through the path is then

$$
\begin{aligned}
\underline{E}_m(y') &= \underline{E}_m^+ e^{-jk_{ym}y'} \cdot e^{-jk_{ym}(a-y')} \cdot \overrightarrow{\underline{\Gamma}}_m(a) \cdot e^{-jk_{ym}(a)} \cdot \overleftarrow{\underline{\Gamma}}_m(0) \cdot e^{-jk_{ym}y'} \\
&= \underline{E}_m^+ e^{-jk_{ym}y'} \cdot e^{-j2k_{ym}a}.
\end{aligned}
\tag{2.21}
$$

The transverse resonance condition requires that the wave in Eq. (2.21) is identical with the original forward wave, $\underline{E}_m^+ e^{-jk_{ym}y'}$. That is,

$$
\underline{E}_m^+ e^{-jk_{ym}y'} = \underline{E}_m^+ e^{-jk_{ym}y'} \cdot e^{-j2k_{ym}a}.
\tag{2.22}
$$

As a result, the transverse propagation constant is derived as

$$
e^{-j2k_{ym}a} = 1 \text{ or } k_{ym} = \frac{m\pi}{a}, \quad m = 1,2,\dots.
\tag{2.23}
$$

Now using the result of Eq. (2.23), the transverse resonance condition is derived in terms of the reflection coefficients at $y = y'$.

From Eq. (2.16), $\overrightarrow{\underline{\Gamma}}_m(y')$, the reflection coefficient looking into the $+y$ direction at $y = y'$ is expressed by

$$
\overrightarrow{\underline{\Gamma}}_m(y') = \overleftarrow{\underline{\Gamma}}_m(0)e^{-j2k_{ym}y'}.
\tag{2.24a}
$$

Also $\overleftarrow{\underline{\Gamma}}_m(y')$, the reflection coefficient looking into the $-y$ direction at $y = y'$ is obtained as

$$
\overleftarrow{\underline{\Gamma}}_m(y') = \overrightarrow{\underline{\Gamma}}_m(a)e^{-j2k_{ym}(a-y')}.
\tag{2.24b}
$$

By combining Eq. (2.23) with Eq. (2.24b), the representation of the transverse resonance condition in terms of the reflection coefficients at $y = y'$ results in:

$$\overrightarrow{\Gamma}_m(y') \cdot \overleftarrow{\Gamma}_m(y') = e^{-j2k_{ym}a} = 1. \tag{2.25}$$

In order to derive the expression of the transverse resonance condition in terms of the impedances at $y = y'$, consider the wave impedances looking into the $+y$ and $-y$ direction at $y = y'$, $\overrightarrow{Z}_m(y')$ and $\overleftarrow{Z}_m(y')$. Using Eq. (2.16), the impedances are

$$\overrightarrow{Z}_m(y') = Z_{\mathrm{TE}_m}\frac{1 + \overrightarrow{\Gamma}_m(y')}{1 - \overrightarrow{\Gamma}_m(y')} \tag{2.26a}$$

$$\overleftarrow{Z}_m(y') = Z_{\mathrm{TE}_m}\frac{1 + \overleftarrow{\Gamma}_m(y')}{1 - \overleftarrow{\Gamma}_m(y')} \tag{2.26b}$$

where Z_{TE_m} is the wave impedance of the m-th mode in the medium. With Eq. (2.25), the impedance $\overleftarrow{Z}_m(y')$ is hence expressed in terms of $\overrightarrow{\Gamma}_m(y')$:

$$
\begin{aligned}
\overleftarrow{Z}_m(y') &= Z_{\mathrm{TE}_m}\frac{1 + \frac{1}{\overrightarrow{\Gamma}_m(y')}}{1 - \frac{1}{\overrightarrow{\Gamma}_m(y')}} \\
&= Z_{\mathrm{TE}_m}\frac{\overrightarrow{\Gamma}_m(y') + 1}{\overrightarrow{\Gamma}_m(y') - 1} \\
&= -\overrightarrow{Z}_m(y'). \tag{2.27}
\end{aligned}
$$

As a result, the transverse resonance condition requires that in terms of the wave impedance, the summation of two wave impedances looking into the $+y$ and $-y$ direction at $y = y'$ should be zero. That is,

$$\overrightarrow{Z}_m(y = y') + \overleftarrow{Z}_m(y = y') = 0. \tag{2.28}$$

The two impedances of $\overrightarrow{Z}_m(y = y')$ and $\overleftarrow{Z}_m(y = y')$ are given by Eq. (2.17) for TE wave as follows:

$$\overrightarrow{Z}_m(y = y') = j\eta \tan(k_{ym}y') \tag{2.29a}$$
$$\overleftarrow{Z}_m(y = y') = j\eta \tan(k_{ym}(a - y')) \tag{2.29b}$$

with

$$\eta = \sqrt{\frac{\mu}{\varepsilon}}. \tag{2.29c}$$

Eq. (2.28) results in

$$\tan(k_{ym}y') = -\tan(k_{ym}(a - y')) \tag{2.30a}$$

so that

$$-k_{ym}(a - y') = m\pi + k_{ym}y, \quad m = 1, 2, \ldots . \tag{2.30b}$$

Thus, the solution for the transverse propagation constant is

$$k_{ym} = \frac{m\pi}{a}. \tag{2.31}$$

and the dispersion relation of $k_{zm} = \sqrt{k_1^2 - k_{ym}^2}$ is completed. The result of Eq. (2.31) is equivalent to that of Eq. (2.23). It is shown above that by calculating the wave impedances and solving Eq. (2.28), the transverse propagation constant in the medium is found and the dispersion relation is determined.

Here the representations of the TRM in terms of the impedance and the reflection coefficients are derived only for TE waves. Note that since for TM waves, the same results, Eqs. (2.25) and (2.28) are derived, the derivation is left out. In the next section, the application of the transverse resonance condition for multilayer media is introduced.

2.2.2 Applications of the TRM for multilayer dielectrics

A partially dielectric-slab-loaded parallel-plate waveguide is illustrated in Fig. 2.6(a). Three dielectric layers ($\varepsilon_1 = \varepsilon_0\varepsilon_{r1}, \varepsilon_2 = \varepsilon_0\varepsilon_{r2}, \varepsilon_3 = \varepsilon_0\varepsilon_{r3}$) are homogeneous and isotropic in the direction of propagation, i.e. the z direction.

2.2.2.1 TM-case

First, the TM wave is considered. In the case of $\varepsilon_{r2} < \varepsilon_{r1}$, ε_{r3}, waves will propagate in the media 1 and 3. That is, the parallel-plate waveguide guides surface waves. Their energy will be confined and transmitted in the media 1 and 3. It should be noted that the phase velocity of the surface waves can be changed by modifying the dielectric thickness and dielectric constants.

In order to determine the relation between the phase velocity in the media and the thickness of the dielectrics, the transverse propagation constants in each region are required. Fig. 2.6(b) shows the transverse resonance equivalent circuit for the structure. $\underline{Z}_{TM1}$, $\underline{Z}_{TM2}$, and $\underline{Z}_{TM3}$ represent the wave
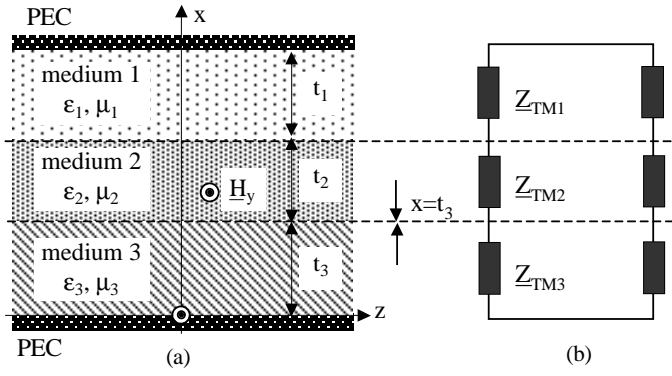
Figure 2.6: For TM wave case, (a) a parallel-plate waveguide filled with three dielec-
tric layers. (b) Its transverse resonance equivalent model.

impedances in the transverse direction, i.e. the x direction in each medium.
Thus,

$$\underline{Z}_{\mathrm{TMi}} = \frac{k_{xi}}{\omega \varepsilon_i} \; , \; i = 1, 2, 3 \tag{2.32a}$$

where

$$k_{xi} = \sqrt{k_i^2 - k_{zi}^2} \text{ and } k_i = \omega \sqrt{\mu_i \varepsilon_i}. \tag{2.32b}$$

Using Eq. (2.18) and Eq. (2.32), the input wave impedance looking into the
$+x$ direction at $x = t_2 + t_3$ is

$$\overrightarrow{\underline{Z}}(x = t_2 + t_3) = j \frac{k_{x1}}{\omega \varepsilon_1} \tan(k_{x1} t_1). \tag{2.33}$$

In a similar way, the input wave impedance looking into the $-x$ direction at
$x = t_3$ is

$$\overleftarrow{\underline{Z}}(x = t_3) = j \frac{k_{x3}}{\omega \varepsilon_3} \tan(k_{x3} t_3). \tag{2.34}$$

With Eqs. (2.18), (2.32), and (2.33), the input wave impedance looking into

the $+x$ direction at $x = t_3$ is obtained as

$$\overrightarrow{\underline{Z}}(x = t_3) = jZ_{\text{TM2}} \frac{\overrightarrow{\underline{Z}}(x = t_2 + t_3) + j\underline{Z}_{\text{TM2}} \tan(k_{x2}t_2)}{\underline{Z}_{\text{TM2}} + j\overrightarrow{\underline{Z}}(t_2 + t_3)\tan(k_{x2}t_2)}$$

$$= j\frac{k_{x2}}{\varepsilon_{r2}} \cdot \frac{\frac{k_{x1}}{\varepsilon_{r1}}\tan(k_{x1}t_1) + \frac{k_{x2}}{\varepsilon_{r2}}\tan(k_{x2}t_2)}{\frac{k_{x2}}{\varepsilon_{r2}} - \frac{k_{x1}}{\varepsilon_{r1}}\tan(k_{x2}t_2)\tan(k_{x1}t_1)}. \tag{2.35}$$

If the transverse resonance condition at $x = t_3$ is applied,

$$\overrightarrow{\underline{Z}}(x = t_3) + \overleftarrow{\underline{Z}}(x = t_3) =$$

$$\frac{k_{x3}}{\varepsilon_{r3}}\tan(k_{x3}t_3) + \frac{k_{x2}}{\varepsilon_{r2}} \cdot \frac{\frac{k_{x1}}{\varepsilon_{r1}}\tan(k_{x1}t_1) + j\frac{k_{x3}}{\omega\varepsilon_3}\tan(k_{x2}t_2)}{\frac{k_{x2}}{\varepsilon_{r2}} - \frac{k_{x1}}{\varepsilon_{r1}}\tan(k_{x2}t_2)\tan(k_{x1}t_1)} = 0. \tag{2.36}$$

This equation for the transverse propagation constant is solved numerically or graphically.

As an example of calculating the transverse propagation constants, consider the symmetric case of the structure in Fig. 2.6(a), that is, $t_1 = t_3$ and $\varepsilon_1 = \varepsilon_3$ [Abe00]. With these conditions, Eq. (2.36) is rewritten as

$$A^2 - \frac{2k_{x2}}{\varepsilon_{r2}\tan(k_{x2}t_2)}A + \frac{k_{x2}}{\varepsilon_{r2}^2}\tan(k_{x2}t_2) = 0 \tag{2.37a}$$

where

$$A = \frac{k_{x3}}{\varepsilon_{r3}}\tan(k_{x3}t_3). \tag{2.37b}$$

Snell's law requires that the propagation constant k_{z3} in the medium 3 should be equal to k_{z2} in the medium 2 at $x = t_3$. That is, the refraction index n at $x = t_3^+$ in the medium 3 is equal to that at $x = t_3^-$ in the medium 2:

$$n = \sqrt{\varepsilon_{r3} - \left(\frac{k_{x3}}{k_0}\right)^2} = \sqrt{\varepsilon_{r2} - \left(\frac{k_{x2}}{k_0}\right)^2} \tag{2.38}$$

where $k_0 = \omega\sqrt{\mu_0\varepsilon_0}$. By substituting Eq. (2.38) for k_{x2} and k_{x3} in Eq. (2.37), Eq. (2.37) contains only one variable, the refraction index n. Therefore, the second order equation determines the variable A from Eq. (2.37a) and then A has to be equal to that in Eq. (2.37b). Therefore, Eq. (2.37b) for the refraction index n is solved, that is, the transverse propagation constant k_{x2} or the transverse propagation constant k_{x3}.

Especially, for the above case, i.e. $\varepsilon_1 = \varepsilon_3$ and $t_1 = t_3$, the calculation can be further simplified. Due to $\varepsilon_1 = \varepsilon_3$ and $t_1 = t_3$, the entire structure becomes symmetric with respect to the plane $x = \frac{t_2}{2} + t_3$. Since the tangential magnetic field or current at the plane of symmetry $x = \frac{t_2}{2} + t_3$ must be continuous, the plane of symmetry can be replaced by a PEC. In Fig. 2.7(b), its equivalent model is displayed. Note that the symmetry plane is equivalent to a short just like a PEC for TM surface waves. To get the transverse propagation constants,

Figure 2.7: For TM wave case, (a) a half structure equivalent to the composite waveguide in Fig. 2.6 in case $\varepsilon_1 = \varepsilon_3$ and $t_1 = t_3$. (b) Its transverse resonance equivalent model.

the transverse resonance condition at $x = t_3$ is applied. $\overleftarrow{Z}(x = t_3)$ in Eq. (2.34) is

$$\overrightarrow{Z}(x = t_3) = j\frac{k_{x2}}{\omega\varepsilon_2}\tan(k_{x2}\frac{t_2}{2}).\tag{2.39}$$

Therefore, using Eq. (2.38),

$$\overrightarrow{Z}(x = t_3) \quad + \quad \overleftarrow{Z}(x = t_3) =$$

$$\frac{\sqrt{\varepsilon_{r3} - n^2}}{\varepsilon_{r3}}\tanh(k_0\sqrt{\varepsilon_{r3} - n^2}\,t_3) \quad + \quad \frac{\sqrt{\varepsilon_{r2} - n^2}}{\varepsilon_{r2}}\tan(k_0\sqrt{\varepsilon_{r2} - n^2}\,t_2) = 0.\tag{2.40}$$

As shown in Eq. (2.40), the result becomes much simpler than that in Eq. (2.37). Eq. (2.40) is solved for the refraction index n, numerically or graphically.

2.2.2.2 TE-case
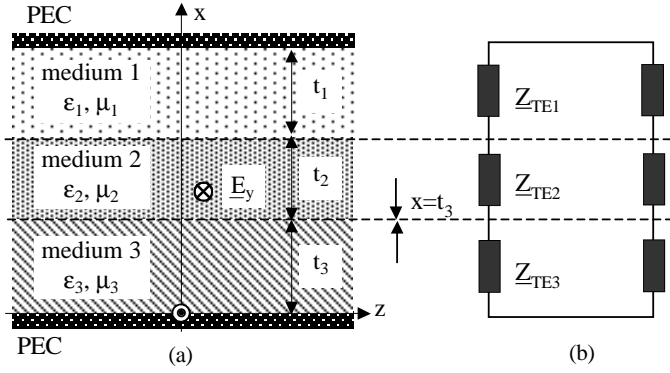
Figure 2.8: For TE wave case, (a) a parallel-plate waveguide filled with three dielectric layers. (b) Its transverse resonance equivalent model.

Now we consider the case of the TE wave in Fig. 2.8. From the definition of the wave impedances for TE waves in Eq. (2.12), the wave impedances are expressed by

$$\underline{Z}_{\text{TE}i} = \frac{\omega \mu_i}{k_{xi}} \ , \ i = 1, 2, 3. \tag{2.41}$$

By assuming $\mu_i = \mu_0$, Eq. (2.36) for the TE wave is

$$k_{x2} \tan(k_{x3} t_2) + \frac{k_{x2} k_{x3} \tan(k_{x1} t_1) + j k_{x1} k_{x2} \tan(k_{x2} t_2)}{k_{x1} - k_{x2} \tan(k_{x2} t_2) \tan(k_{x1} t_1)} = 0. \tag{2.42}$$

For the case of $t_1 = t_3$ and $\varepsilon_1 = \varepsilon_3$ in Fig. 2.9(a), the tangential magnetic field from the point of view of field theory and voltage from the point of view of circuit theory must be continuous at the symmetry plane $x = \frac{t_2}{2} + t_3$ for the TE wave. Therefore, the symmetry plane can be replaced with a perfect magnetic conductor (PMC) while for the TM wave it is replaced with a PEC. In Fig. 2.9(b), the equivalent model is depicted. Here the symmetry plane is represented as an open. Thus,

$$\overrightarrow{\underline{Z}}(x = t_3) = -j \frac{\omega \mu}{k_{x2}} \cot(k_{x2} \frac{t_2}{2}). \tag{2.43}$$

Using Eq. (2.34),

$$\overleftarrow{\underline{Z}}(x = t_3) = j \frac{\omega \mu}{k_{x3}} \tan(k_{x3} t_3). \tag{2.44}$$
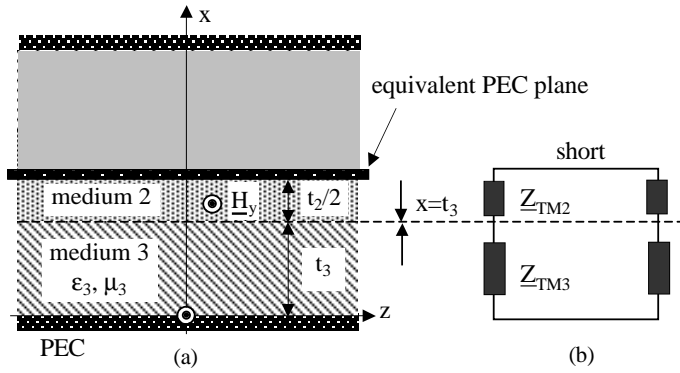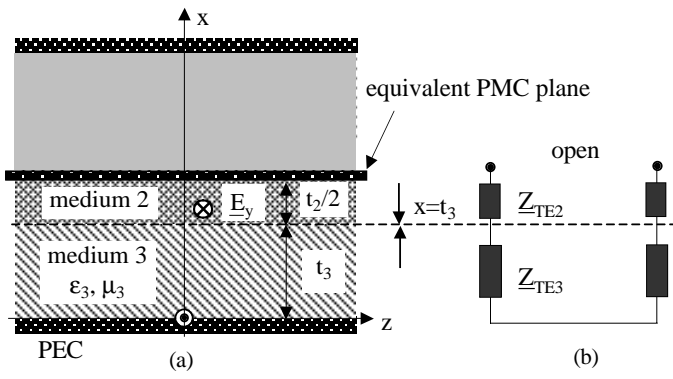
Figure 2.9: For TE wave case, (a) a half structure equivalent to the composite wave-guide in Fig. 2.6 in case $\varepsilon_1 = \varepsilon_3$ and $t_1 = t_3$. (b) Its transverse resonance equivalent model.

As a result,

$$k_{x2} \tan(k_{x3} t_3) - k_{x3} \cot(k_{x2} \frac{t_2}{2}) = 0. \qquad (2.45)$$

In the similar way, the transverse propagation constants, k_{x2} and k_{x3} are solved graphically or numerically.

Chapter 3

PBG Structures for Arbitrary Surface Impedance

This chapter presents two PBG structures that support arbitrary surface impedance for guiding and suppressing surface waves. The first structure is a conventional corrugated surface. The second is a periodic and regular metal post structure. The similarities and differences between both are illustrated by applying the transmission line theory and the TRM in the previous chapter.

3.1 Corrugated surface

The properties of the corrugated surfaces are well described in [Ell81], [Kil90], [Col91], [Eom01]. Many applications have been proposed. In this section, behaviors of the corrugated surface in a parallel-plate waveguide are presented by using the transmission line theory and the TRM, especially related to the surface impedance of the corrugated surface and surface waves.

3.1.1 Corrugated surface in a parallel-plate waveguide

Figure 3.1 shows a conventional corrugated surface within an air-filled parallel-plate waveguide and its cross-sectional view. It will be assumed that the thickness between the corrugations, called the tooth width thickness D is infinitely thin, so that the influence of the thickness can be neglected as described in [Bri48], [Wal65]. The length of the corrugation in the y direction

is infinite whereas the height t is constant. As shown in the cross-sectional view, the entire structure is divided into two regions. $\underline{Z}_1$ and $\underline{Z}_2$ are the wave impedances of region I and II, respectively.

(a)

(b)
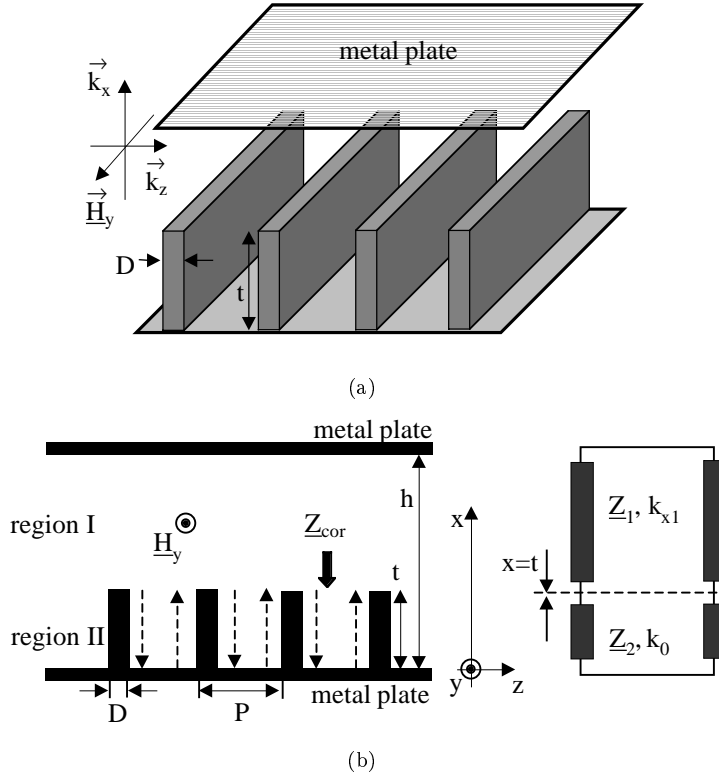
Figure 3.1: (a) Corrugated surface in a parallel-plate waveguide. (b) Cross-sectional view [left] and its equivalent transverse resonance model [right]. The dotted lines indicate the propagating paths of the surface wave.

For an incident magnetic field parallel to the y axis $\underline{H}_{y1}$ (TM wave), the Helmholtz equation for the magnetic field in region I ($t < x < h$) is expressed by

$$\left(\frac{\partial^2}{\partial x^2} + \frac{\partial^2}{\partial z^2} + k_0^2\right)\underline{H}_{y1}(x, z) = 0. \tag{3.1}$$

With $\underline{H}_{y1}(x, \infty) = 0$, the magnetic field $\underline{H}_{y1}(x,z)$ results in

$$\underline{H}_{y1}(x,z) \quad = \quad (\underline{H}_{y1}^{+}e^{-jk_{x1}(x-h)} + \underline{H}_{y1}^{-}e^{jk_{x1}(x-h)})e^{-jk_{z1}z} \qquad (3.2\text{a})$$

with

$$\begin{aligned} k_{x1}^2 &= k_0^2 - k_{z1}^2 \\ k_0 &= \omega\sqrt{\mu_0\varepsilon_0}. \end{aligned} \qquad (3.2\text{b})$$

From the relation of $\vec{\underline{E}}(x,z) = \frac{1}{j\omega\varepsilon_0}\nabla \times \vec{\underline{H}}(x,z)$, the electric field is

$$\underline{E}_{x1}(x,z) \quad = \quad \frac{k_{z1}}{\omega\varepsilon_0}\underline{H}_{y1} \qquad (3.2\text{c})$$

$$\begin{aligned} \underline{E}_{z1}(x,z) \quad &= \quad \frac{k_{x1}}{\omega\varepsilon_0}(-\underline{H}_{y1}^{+}e^{-jk_{x1}(x-h)} + \underline{H}_{y1}^{-}e^{jk_{x1}(x-h)}))e^{-jk_{z1}z} \\[2mm] &= \quad (\underline{E}_{z1}^{+}e^{-jk_{x1}(x-h)} + \underline{E}_{z1}^{-}e^{jk_{x1}(x-h)})e^{-jk_{z1}z} \qquad (3.2\text{d}) \end{aligned}$$

with

$$\underline{E}_{z1}^{+} = -\frac{k_{x1}}{\omega\varepsilon_0}\underline{H}_{y1}^{+}$$

$$\underline{E}_{z1}^{-} = \frac{k_{x1}}{\omega\varepsilon_0}\underline{H}_{y1}^{-}. \qquad (3.2\text{e})$$

Using the boundary condition $\underline{E}_{z1}(x = h, z) = 0$,

$$\underline{H}_{y1}^{+} = \underline{H}_{y1}^{-} \quad \text{and} \quad \underline{E}_{z1}^{+} = -\underline{E}_{z1}^{-}. \qquad (3.2\text{f})$$

In order to derive the field in a corrugation ($0 < z < P$ and $0 < x < t$), the boundary conditions, $\underline{E}_{z2}(x = 0, z) = 0$, $\underline{E}_{x2}(x, z = 0) = 0$ and $\underline{E}_{x2}(x, z = P) = 0$ should be used [Col91]. Thus, the magnetic and electric fields in the corrugation are

$$\underline{H}_{y2}(x, z) \quad = \quad \sum_{i=0}^{\infty}\cos\left(\frac{i\pi z}{P}\right)(e^{jk_{x2}x} + e^{-jk_{x2}x}) \qquad (3.3\text{a})$$

$$\underline{E}_{x2}(x, z) \quad = \quad \frac{1}{\omega\varepsilon_0}\sum_{i=0}^{\infty}\left(\frac{i\pi}{P}\right)\sin\left(\frac{i\pi z}{P}\right)(e^{jk_{x2}x} + e^{-jk_{x2}x}) \qquad (3.3\text{b})$$

$$\underline{E}_{z2}(x, z) \quad = \quad \frac{1}{\omega\varepsilon_0}\sum_{i=0}^{\infty}k_{x2}\cos\left(\frac{i\pi z}{P}\right)(e^{jk_{x2}x} - e^{-jk_{x2}x}) \qquad (3.3\text{c})$$

where

$$k_{x2} = \sqrt{k_0^2 - \left(\frac{i\pi}{P}\right)^2} \text{ and } 0 < z < P. \tag{3.3d}$$

Moreover, it will be assumed that the period P is much smaller than a wavelength in free space λ_0 ($P \ll \lambda_0$). Therefore, without $i \neq 0$ in Eq. (3.3) the propagation constant k_{x2} is always imaginary, that is, no propagating modes exist. From Eq. (3.3d), $i = 0$ leads to $k_{x2} = k_0$, thus, only the lowest mode in the parallel-plate waveguide, the TEM mode exists in the x direction in the corrugations. The incident wave propagating in the $-x$ direction is $e^{jk_{x2}x}$, and the reflected wave is $e^{-jk_{x2}x}$. The dotted lines in Fig. 3.1(b) are the propagating paths of surface wave.

The equivalent transverse resonance model of the corrugated surface is illustrated in Fig. 3.1. According to the definition of the wave impedance in Ch. 2, the wave impedance $\underline{Z}_{\mathrm{TM2}}$ is obtained as

$$\underline{Z}_{\mathrm{TM2}} = \underline{Z}_2 = \sqrt{\frac{\mu_0}{\varepsilon_0}} = \eta_0 \tag{3.4}$$

while the transverse wave impedance in region I is specified as

$$\underline{Z}_1 = -\frac{\underline{E}_{z1}^+(x,z)}{\underline{H}_{y1}^+(x,z)} = \frac{k_{x1}}{\omega\varepsilon_0}. \tag{3.5}$$

Now using transmission line theory, the surface impedance looking into the corrugation at $x = t$, $\underline{Z}_{\mathrm{cor}} = \overleftarrow{\underline{Z}}(x = t)$ is obtained as

$$
\begin{aligned}
\underline{Z}_{\mathrm{cor}} = \overleftarrow{\underline{Z}}(x = t) &= j\underline{Z}_2 \tan(k_0 t) \\
&= j\eta_0 \tan(k_0 t).
\end{aligned}
\tag{3.6}
$$

In Fig. 3.2, the surface impedance is plotted as a function of the corrugation height. As shown, depending on the corrugation height t, the corrugated surface provide arbitrary surface impedance. It is also seen that the surface impedance $\underline{Z}_{\mathrm{cor}}$ is divided into three kinds of the surface impedance depending on the height t.

First, for the height of about $t = (2m + 1)\lambda_0/4$ ($m = 0, 1, 2, \dots$) (range I), the surface impedance becomes theoretically infinite. However, the impedance of the wave in the range I in Fig. 3.1(b) cannot be infinite. Therefore, due to impedance mismatch at the boundary $x = t$, no surface waves are allowed on the surface. It should be noted that although there are no surface waves, it
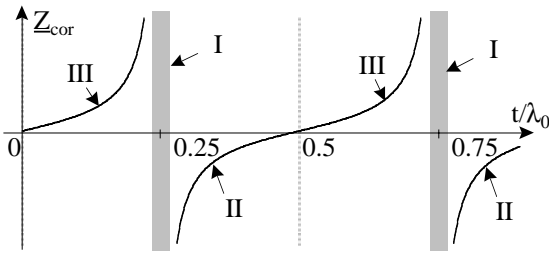
Figure 3.2: Surface impedance as a function of the corrugation height normalized by the free-space wave length λ_0.

is possible that propagating modes exist. For instance, consider a corrugated horn [Men74]. In a traveling-wave antenna using the corrugated surface, the energy is radiated in free space [Ell81] instead of flowing along the corrugated surface. In other words, the bandgaps are true to the surface waves, not the wave propagating in the direction perpendicular to the corrugations [Thu02].

In case $(2m+1)\lambda_0/4 < t < (2m+2)\lambda_0/4$ (range II), the surface impedance becomes capacitive. This range of the height is very often utilized for suppressing TM surface waves which requires inductive surface impedance. From this fact above, the range (or frequency range) is generally called as a forbidden band for the TM surface waves. It is important to note that the corrugation height t plays the most important role in suppressing TM surface waves or in capacitive surface impedance. This fact is applied to the design of circular corrugated flares in Ch. 4.

Finally, for $(2m)\lambda_0/4 < t < (2m+1)\lambda_0/4$ (range III), the surface impedance becomes inductive, so that TM surface waves can propagate along the corrugated surface. Thus, since the surface wave propagates along the corrugated surface, there is no power flux in the x direction and hence the transverse propagation constant k_{x1} is imaginary.

Now provided that the corrugated surface guides TM surface waves, the transverse propagation constant k_{x1} in Eq. (3.2) becomes imaginary. Thus, the field in the region I given by Eq. (3.2) can be written as follows.

$$\underline{H}_{y1} = \cosh\big(|k_{x1}|(x-h)\big)e^{-jk_{z1}z} \tag{3.7a}$$

$$\underline{E}_{x1} = \frac{k_{z1}}{\omega\varepsilon_0}\underline{H}_{y1} \tag{3.7b}$$

$$\underline{E}_{z1} = \frac{|k_{x1}|\sinh\big(|k_{x1}|(x-h)\big)}{j\omega\varepsilon_0}e^{-jk_{z1}z} \tag{3.7c}$$

where

$$k_{z1}^2 = k_0^2 + |k_{x1}|^2 = k_0^2(1 + \kappa_1^2) \qquad (3.7\text{d})$$

$$k_{x1} = j|k_{x1}| \qquad (3.7\text{e})$$

$$\kappa_1 = \frac{|k_{x1}|}{k_0}. \qquad (3.7\text{f})$$

It should be pointed out that due to $k_{z1} > k_0 (= 2\pi/\lambda_0)$ and therfore $\lambda_{z1} (= 2\pi/k_{z1}) < \lambda_0$ in Eq. (3.7d), the phase velocity of the surface wave is slower than the speed of light, whereas in general the phase velocity in the waveguide is faster [Bri48]. This phenomenon of *slow wave* can be explained using the principle of charge and discharge of electric energy storage at the interface in circuit theory. The quantitative analysis of the phase velocity is given later.

Guiding a TE surface wave in the range II in Fig. 3.2 is different from that of a TM surface wave in the range III [Col91], [Ufi01]. The lowest mode for the TE case is a TE_1 mode. Thus to support the TE_1 mode, the spacing between the parallel-plate waveguide P must be larger than $\lambda_0/2$. However, with $P \geq \lambda_0/2$, the edge of the thin plate between two corrugations acts as a diffraction grating. Thus, the corrugated surface will not support the TE surface wave without the case that a high-dielectric-constant material would be filled in the corrugation [Col91].

In practice, the tooth width D cannot be infinite, so that the influence of the finite thickness D on the surface impedance should be taken into account. From the point of view of circuit theory, the volume filled by a tooth does not store any electric energy in the corrugation. Thus, the surface impedance should be reduced by the ratio of the tooth width D to the period P. Therefore, the surface impedance in Eq. (3.5) is rewritten as

$$\underline{Z}_{\text{cor}} = \overleftarrow{\underline{Z}}(x = t) = jW\eta_0 \tan(k_0 t) \qquad (3.8)$$

where the weighting factor $W = \left(\frac{P-D}{P}\right)$ is the ratio of the length unfilled by the corrugation to the period. It is necessary to note that the thinner the tooth width D is, the better Eq. (3.8) predicts the impedance.

Also, practically the length of the corrugation can not be infinite. Therefore, depending on the incident angle of the TM surface wave, the weighting factor W in Eq. (3.8) varies and then the magnitude of the surface impedance changes, especially in the ranges II and III. In other words, the corrugated surface acts as an anisotropic dielectric in the range I where the surface impedance is inductive. However, although the magnitude of the impedance varies according to W, the kind of reactance is determined only by the depth of the corrugation as mentioned previously.

3.1.2 Propagation constant and phase velocity of TM surface waves

In order to determine the propagation constant and phase velocity of surface waves, the propagation constant k_{z1} in Eq. (3.7d) should be calculated. First, k_{x1} is found using the TRM. Second, k_{z1} is determined by the dispersion relation in Eq. (3.7d). The surface impedance looking into the $-x$ direction at $x = t$ (see Fig. 3.1(b)), $\overleftarrow{\underline{Z}}(x = t)$ is given in Eq. (3.8) and the input impedance looking into the $+x$ direction, $\overrightarrow{\underline{Z}}(x = t)$ is

$$\overrightarrow{\underline{Z}}(x = t) = j\underline{Z}_1 \tan(k_{x1}(h - t)) \tag{3.9}$$

where $\underline{Z}_1$ is the wave impedance of the TM surface wave. From Eqs. (3.5) and (3.7e),

$$\underline{Z}_1 = \frac{k_{x1}}{\omega\varepsilon_0} = \frac{j|k_{x1}|}{\omega\varepsilon_0} = \frac{jk_0\kappa_1}{\omega\varepsilon_0} = j\eta_0\sqrt{n^2 - 1} \tag{3.10a}$$

where n is the refraction index of the corrugated surface given by

$$n = \frac{k_{z1}}{k_0}. \tag{3.10b}$$

Also, the transverse propagation constant k_{x1} in Eq. (3.9) is expressed by

$$k_{x1} = jk_0\sqrt{n^2 - 1}. \tag{3.11}$$

Thus, $\tan(k_{x1}(h - t))$ in Eq. (3.9) results in

$$\tan(k_{x1}(h - t)) = j\tanh(k_0\sqrt{n^2 - 1}(h - t)). \tag{3.12}$$

The deviation of the hyperbolic tangent function from the tangent function is described in appendix A. Thus, the impedance $\overrightarrow{\underline{Z}}(x = t)$ is

$$\overrightarrow{\underline{Z}}(x = t) = -j\eta_0\sqrt{n^2 - 1}\tanh(k_0\sqrt{n^2 - 1}(h - t)). \tag{3.13}$$

With Eq. (3.8) and Eq. (3.13), the TRM results in

$$\overrightarrow{\underline{Z}}(x = t) + \overleftarrow{\underline{Z}}(x = t) = 0$$

$$\sqrt{n^2 - 1}\tanh(k_0\sqrt{n^2 - 1}(h - t)) - W\tan(k_0 t) = 0. \tag{3.14a}$$

Also, using Eq. (3.10), Eq. (3.14a) is rewritten as

$$\kappa_1 \tanh(k_0\kappa_1(h - t)) - W\tan(k_0 t) = 0. \tag{3.14b}$$

By solving the above equations graphically or numerically, the desired transverse propagation constant of the TM surface wave is obtained.

Using Eq. (3.14b), the influence of the weighting factor W on the phase velocity of the TM surface wave is investigated. The phase velocity of the surface wave is obtained from Eq. (3.7d) as

$$\frac{v_p}{c} = \frac{1}{\sqrt{1 + \kappa_1^2}} \tag{3.15}$$

where c is the speed of light in free space. κ_1 is calculated from Eq. (3.7f) after Eq. (3.14b) is solved.

In Fig. 3.3, the phase velocity v_p of the corrugated surface is plotted. For the calculation, the height t and the spacing $(h - t)$ are normalized by the wavelength λ_0. It is clearly seen that v_p is always lower than the speed of light c. Also, as W is getting smaller, the phase velocity v_p becomes higher for the same height. The reason is that with smaller W, the surface impedance becomes lower as shown in Eq. (3.8). Since there is no solution of κ_1 in $0.25\lambda_0 < t < 0.5\lambda_0$, namely the stopband for TM surface waves, no wave numbers or phase velocities corresponding to κ_1 exist.

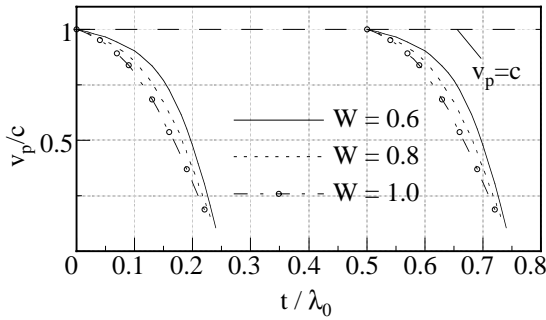Figure 3.3: Illustration of the influence of the tooth width D on the phase velocity with $(h - t) = \lambda_0/2$ fixed ($W = 1.0$ for $D = 0$).

3.2 Regular and periodic metal posts

In the above case of the corrugated surface, the surface impedance is dependent on the direction of the incident waves. In other words, the corrugated surface acts as an anisotropic artificial dielectric [Wal65], [Lee71], [Col91]. For the

purpose of suppressing the surface waves or building high surface impedance, the isotropy is unnecessary. However, in order to guide surface waves to an arbitrary direction at lower frequencies than f_0, that is, in the range II and III in Fig. 3.2, a structure should have an isotropy [Wal65]. In the following section, a PBG structure supporting TM surface waves and simultaneously nearly isotropic property is proposed.

3.2.1 Theoretical analysis

Figure 3.4 shows periodic and regular square metal posts in a parallel-plate waveguide. The unit cell of the structure, called a lattice, is a square. The metal post structure can be considered as a *bed-of-nail* structure placed in a parallel-plate waveguide. In [Wal65], [Kin81], and [Kin83], the bed-of-nail structure was investigated experimentally and theoretically. The surface impedance of the bed-of-nail structure becomes inductive or capacitive depending on the height of the posts. Thus the structure is used to guide surface waves [Wal60], [Wal65]. Here, characteristics of the bed-of-nail structure built in a parallel-plate waveguide are reported. Also new lattices and new shapes of the metal posts for the isotropy are presented.

In fig. 3.4, the parallel-plate waveguide is filled with an isotropic homogeneous dielectric ($\varepsilon = \varepsilon_0 \varepsilon_r$). The period P is much smaller than λ_0, at the same time the width of the posts D is smaller than half a period in order that the complete structure behaves as a continuous medium of an artificial dielectric. However, it should be noted that if the period P satisfies the Bragg condition in the k_z direction, that is, P is about a half of a wavelength, the structure has maximum reflection in the k_z direction and then has Bragg resonance frequencies [Yar84], [Bul93], [Lee94], [Pes01], [Thu02].

The basic principle is that with the electric field ($\vec{\underline{E}}_{\mathrm{inc}}$) perpendicular to the posts, the charges on the posts will be displaced for setting up an induced field ($\vec{\underline{E}}_{\mathrm{ind}}$) that will remove the applied field at the obstacle surface. This principle is illustrated in Fig. 3.4(b). Figure 3.4(b) also shows that depending on the geometric parameters of the posts such as height and width, different displacement current is induced.

In Fig. 3.5, the cross-sectional view and its transverse resonance equivalent circuit are displayed. The structure is divided into two regions. The first region is between the upper metal plate and the surface of the PBG structure ($t < x < h$). k_{x1} is the transverse propagation constant and $\underline{Z}_1$ is the intrinsic wave impedance in this region. The second region is the metal post region ($0 < x < t$). k_{x2} is the transverse propagation constant and $\underline{Z}_2$ is the intrinsic
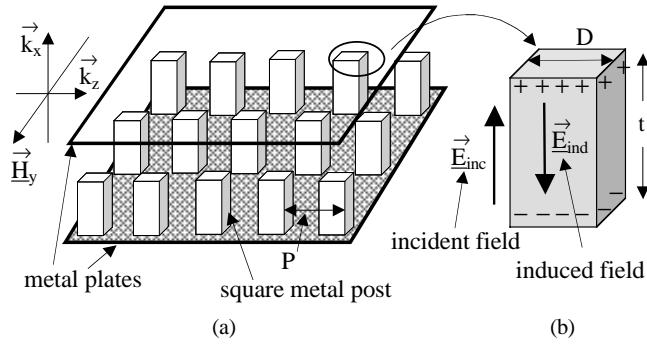
Figure 3.4: Geometry of the PBG structure. (a) Periodic and regular metal posts in a parallel-plate waveguide. (b) Illustration of the field induced on the metal posts by the incident field.

wave impedance in the region. From Eq. (2.32a), the intrinsic wave impedances in each region are

$$\underline{Z}_1 = \frac{k_{x1}}{\omega\varepsilon} \tag{3.16a}$$

$$\underline{Z}_2 = \frac{k_{x2}}{\omega\varepsilon}. \tag{3.16b}$$

In order to calculate the surface impedance of the structure, it will be assumed that due to $P \ll \lambda_0$ and $D \leq P/2$ only the TEM mode exists in the metal post region, similar to a corrugated surface. Thus, k_{x2} is the propagation constant k_2 in the region and the intrinsic wave impedance $\underline{Z}_2 = k_2/(\omega\varepsilon)$. Now the surface impedance $\underline{Z}_{\mathrm{ISO}}$ on the metal posts is

$$\underline{Z}_{\mathrm{ISO}} = jW\underline{Z}_2\tan(k_2 t) \tag{3.17}$$

where $W = \left(1 - \frac{D^2}{P \cdot D}\right)$ is a weighting factor defined as the ratio of the area unfilled by the post to the area $P \cdot D$ as shown in Fig. 3.6. Additionally, in calculating the surface impedance $\underline{Z}_{\mathrm{ISO}}$, fringing at the tops of the metal posts is considered since these fringing fields lead to the effect of adding capacitive to the surface impedance. This means that $k_2 \approx \omega\sqrt{\mu_0\varepsilon}$ and hence the wave impedance $\underline{Z}_2 \approx \eta_0/\sqrt{\varepsilon_r}$.

Similar to a corrugated surface, in the range of $(2m+1)\lambda_0/4 < t < (2m+2)\lambda_0/4$ $(m = 0, 1, 2, \dots)$, the surface impedance $\underline{Z}_{\mathrm{ISO}}$ becomes inductive, so that the structure is capable of guiding TM surface waves along the thin

metal plate

$\underline{H}_y$ Z_{ISO} d h x $\underleftarrow{Z}_{x=t}$ $\underline{Z}_1, k_{x1}$

t

y

$\underrightarrow{Z}_{x=t}$ $\underline{Z}_2, k_{x2}$

P D metal plate z

(a)   (b)
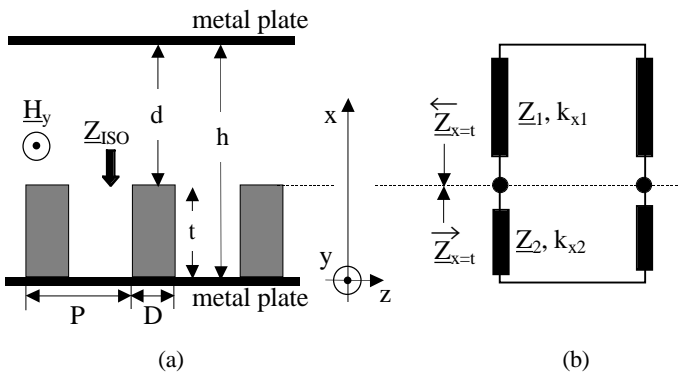
Figure 3.5: (a) Cross-sectional view of the structure of Fig. 3.4. (b) The transverse resonance equivalent circuit.

P·D D

P
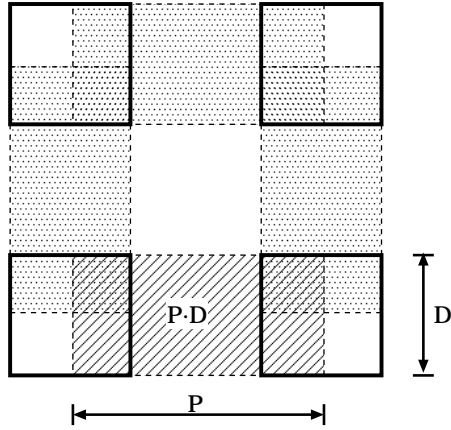
Figure 3.6: Illustration of the way of calculating the factor W in Eq. (3.17).

metal surface. In the range of near the height $t = (2m + 1)\lambda_0/4$, the PBG structure has a high impedance, so that there are no surface waves. Finally, in the range $(2m + 1)\lambda_0/4 < t < (2m + 2)\lambda_0/4$, the surface impedance becomes capacitive.

As mentioned previously, however, the entire structure functions as a continuous dielectric under the assumption $P \ll \lambda_0$ and $D \leq P/2$. Moreover, due to the regularity and periodicity of the metal posts, the PBG structure

will have an isotropy as described in [Wal60] and [Wal65]. The isotropy distinguishes the bed-of-nail structure from corrugated surfaces. Therefor, the PBG structure of regular and periodic metal posts guides a TM surface wave regardless of the incident wave direction.

3.2.1.1 Lattices and post shapes for isotropy

The isotropy of the metal posts is subject to the shape of the metal posts and the lattice of the structure as well since the complete structure is composed of metal posts with a lattice. In order to choose isotropic post shapes, the length obtained by projecting the posts from all directions should be considered. For the isotropy, the projection length is nearly identical for all directions. In
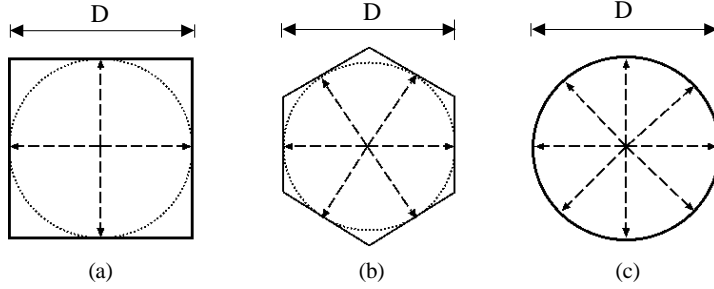
Figure 3.7: Post shapes recommended for an isotropy. (a) Top view of a square post, (b) a hexagonal post, and (c) a circular post.

Fig. 3.7, three different post shapes for the isotropy, a square post, a hexagonal post, and a circular post are displayed. As shown, the circular post has the identical length of D in all directions, so that the PBG structure composed of circular posts is more isotropic than any others.

In case of hexagonal posts and circular posts, the weighting factor W for square posts is invalid since since the area occupied by a post is modified. Thus, according to the definition of the weighting factor W in Eq. (3.17), for hexagonal and circular posts, the weighting factor W in Eq. (3.17) should be changed.

$$W \quad = \quad 1 - \frac{\pi D}{4P}, \quad \text{for circular posts} \tag{3.18a}$$

$$W \quad = \quad 1 - \frac{\sqrt{3}D}{2P}, \quad \text{for hexagonal posts.} \tag{3.18b}$$

However, if D is getting smaller than P and λ_0, both of the square and the hexagon become similar to the circle (see Fig. 3.7) and then the weighting factor W is getting closer to 1. That is, with a small D, the surface impedance depends only on the volume, not the shape of each post if the edge diffraction of the square and the hexagonal posts can be neglected.

In fact, the lattice of the PBG structure plays a more important role

(a)

(b)   (c)
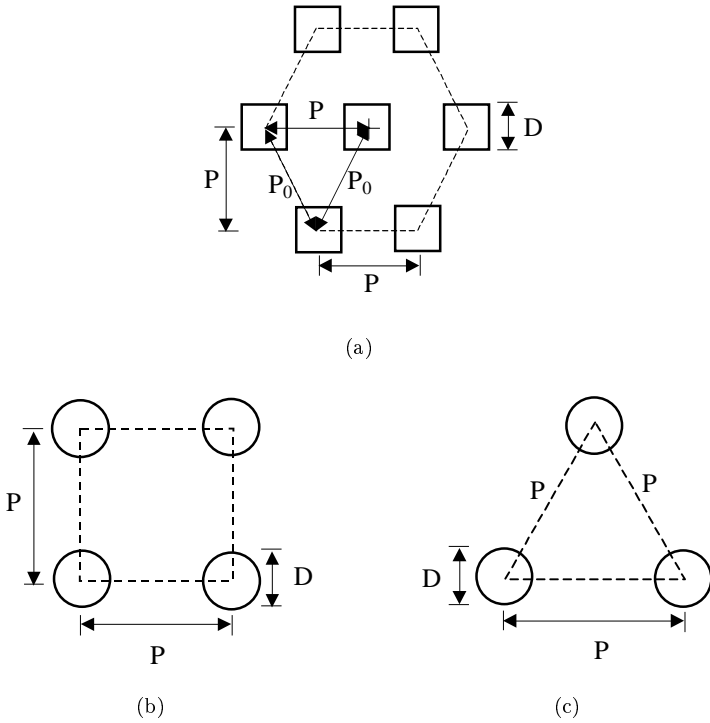
Figure 3.8: Top view of possible lattices for the isotropy of the PBG structure. (a) Hexagonal lattice ($P_0 > P$), (b) square lattice, and (c) triangular lattice.

in the isotropic property than the shape of the posts since without a proper lattice, the PBG structure is anisotropic for any post shapes and dimensions. For the isotropy, the PBG structure should be regular and periodic, so that the performance of the PBG structure is nearly independent of the direction of an incident wave.

In the same way of choosing the isotropic post shape, isotropic lattices

which have the nearly identical projection length in all directions are chosen. In Fig. 3.8, a hexagonal lattice, a square lattice, and a triangular lattice are considered as proper isotropic lattices. Any combinations between the post shapes in Fig. 3.7 and the lattices in Fig. 3.8 are possible such as the triangular lattice with the square posts.

The performances of the above lattices and post shapes are verified in Ch. 5 by applying the PBG structure for the design of an asymmetric parallel-plate waveguide Luneburg lens antenna.

3.2.1.2 Determination of propagation constants

To obtain the transverse propagation constants in the parallel-plate waveguide using the TRM, first, the surface impedance looking into the $-x$ direction at $x = t$, $\overleftarrow{\underline{Z}}(x = t)$ is given by $\underline{Z}_{\text{ISO}}$ in Eq. (3.17). By the transmission line theory, the impedance looking into the $+x$ direction, $\overrightarrow{\underline{Z}}(x = t)$ is

$$
\begin{aligned}
\overrightarrow{\underline{Z}}(x = t) &= j\underline{Z}_1 \tan(k_{x1}(h - t)) \\
&= j\frac{k_{x1}}{\omega\varepsilon} \tan(k_{x1}(h - t))
\end{aligned}
\tag{3.19a}
$$

with

$$
k_{x1} = \sqrt{k_0^2 \varepsilon_r - k_{z1}^2}.
\tag{3.19b}
$$

Considering the PBG structure as a dielectric with a dielectric constant of ε_d and the TEM wave propagating in the $+z$ direction, the propagation constant k_{z1} is $k_0\sqrt{\varepsilon_d}$ at $x = t$. Thus, k_{x1} results in

$$
k_{x1} = k_0\sqrt{\varepsilon_r - \varepsilon_d} = k_0\sqrt{\varepsilon_r - n^2}
\tag{3.20}
$$

where n is the refraction index given by the ratio of k_{z1} to k_{x1}. For the goal of guiding surface waves, the transverse propagation constant k_{x1} should be purely imaginary since no real power flux in the x direction exist but the whole power is transferred along the surface of the PBG structure. For the purpose of the pure imaginary k_{x1}, $\varepsilon_r < n^2$ is required in Eq. (3.20). Now combining $k_{x1} = jk_0\sqrt{n^2 - \varepsilon_d}$ with Eq. (3.19a) results in

$$
\overrightarrow{\underline{Z}}_{x=t} + \overleftarrow{\underline{Z}}_{x=t} = 0
$$

$$
\sqrt{n^2 - \varepsilon_r}\,\tanh\left(k_0\sqrt{n^2 - \varepsilon_r}(h - t)\right) - W\,\tan(k_2 t) = 0.
\tag{3.21a}
$$

Using Eq. (3.20), the above result is

$$|k_{x1}|\tanh(|k_{x1}|(h-t)) - \frac{\eta_0}{\sqrt{\varepsilon_r}}W\,\tan(k_2 t) = 0. \qquad (3.21\text{b})$$

The equation is numerically solved for the transverse propagation constants $|k_{x1}|$. Specially, for the case that the spacing h goes to infinity, that is, without the upper plate,

$$k_{z1} = k_0\sqrt{1 + (W\tan(k_0 t))^2} \qquad (3.22)$$

as given in [Wal60] and [Wal65].

In Fig. 3.9, $|k_{x1}|t$ is calculated as a function of $k_2 t$. Figure 3.9(a) shows the influence of the weighting factor W with $(h - t) = 100t$ fixed. The curve repeats periodically and there is no $|k_{x1}|t$ for $\frac{(2m+1)\pi}{2} < k_2 t < \frac{(2m+2)\pi}{2}$ ($m = 0, 1, 2, \ldots$). As is shown, the increase of W results in the increase of $|k_{x1}|t$. The reason is that a larger W provides the higher surface impedance $\underline{Z}_{\text{ISO}}$ in Eq. (3.17).

In Fig. 3.9(b), $|k_{x1}|t$ is displayed as a function of $k_2 t$ for different spacings $(h - t)$ between the surface of the PBG structure and the upper metal plate. The minifigure shows that with a smaller spacing, $|k_{x1}|t$ is higher.

## 3.2.2 Modified metal post structures

3.2.2.1 Symmetric periodic and regular metal posts structure

First, consider the metal post PBG structure in Fig. 3.10. It is expected that it has also an isotropy and then guides surface waves. For the sake of simplicity, $t_1 = t_3$ and $\varepsilon_{r1} = \varepsilon_{r3}$ are chosen. Thus the entire structure can be simplified by replacing the plane at $x = h/2$ as a PEC or a short in the same as in Fig. 2.7.

In Fig. 3.10(b), the equivalent circuit of the simplified structure is displayed. The equivalent circuit is analogous to that in Fig. 3.5. Therefore, by referring to the result in Eq. (3.21), the relation between the post dimension and the propagation constants is simply obtained as

$$\sqrt{n^2 - \varepsilon_{r2}}\,\tanh\left(k_0\sqrt{n^2 - \varepsilon_{r2}}\frac{(h-t)}{2}\right) = \frac{\varepsilon_{r2}}{\sqrt{\varepsilon_{r1}}}W\tan(k_1 t) \qquad (3.23)$$

where $W = 1 - \frac{D}{P}$ for the metal square posts in Eq. (3.18a). This symmetric PBG structure may be applicable in a surface wave antenna design for the symmetric property [Her00].
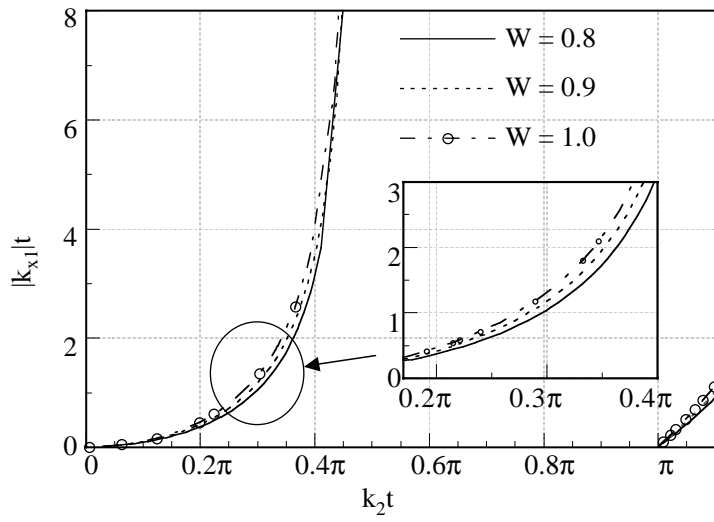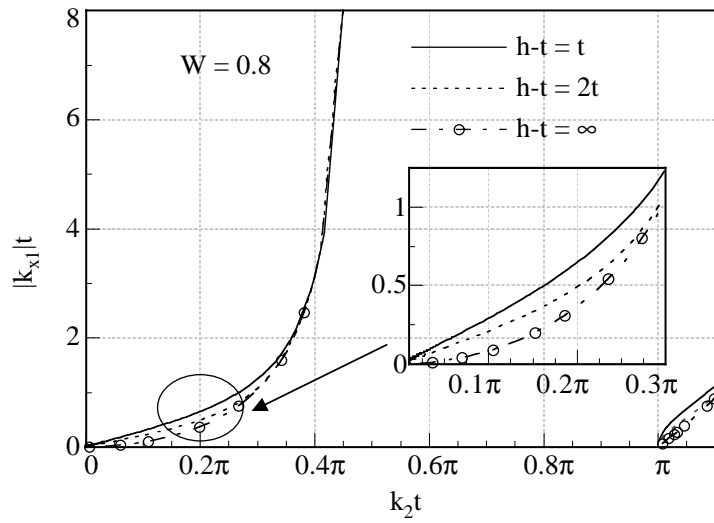
Figure 3.9: Computation of $|k_{x1}|t$ as a function of k_2t in Eq. (3.21b) for (a) three different weighting factors W and (b) three different spacing $(h - t)$.
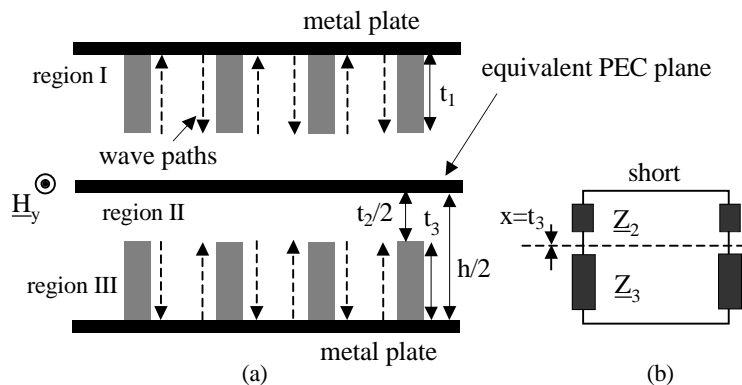
Figure 3.10: (a) Cross-sectional view of the symmetric metal post structure. (b) Transverse equivalent model.

3.2.2.2 Sievenpiper's high-impedance electromagnetic surface

In Fig. 3.11, the high impedance structure described by Sievenpiper, *et al.* [Sie99] is placed in the parallel-plate waveguide. It is composed of periodic regular circular metal posts on a metal ground plane and thin plates on the metal posts. The structure can be considered as a transformed bed-of-nail with the capacitive thin metal plate.

Figure 3.11: High-impedance electromagnetic surface presented in [Sie99].

The cross-sectional view and the equivalent model are displayed in Fig. 3.12. Note that the capacitive reactance is parallel to the impedance of the metal post

structure [Kue64], [Col91]. Thus, the surface impedance of the PBG structure is

$$\underline{Z}_{\text{PBG}} = \overset{\rightarrow}{\underline{Z}}_{x=t} = 1/\left(\frac{1}{\underline{Z}_{\text{ISO}}} + j\omega C_i\right)$$
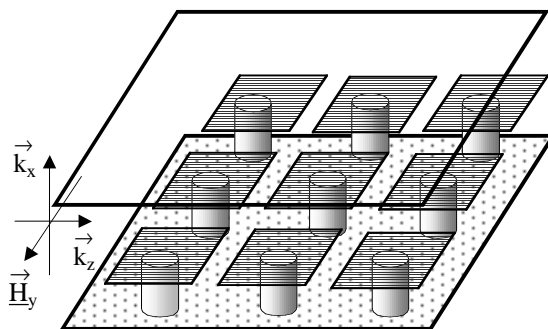
$$= \frac{jW\eta_2 \tan(k_2 t)}{1 - \left(W\eta_2 \tan(k_2 t) \cdot C_i\right)} \tag{3.24}$$

where the impedance $\underline{Z}_{\text{ISO}}$ is given in Eq. (3.17), $\eta_2 = \eta_0/\sqrt{\varepsilon}$, and $W = 1 - \pi D/(4P)$ in Eq. (3.18). Eq. (3.24) states that the structure supports arbitrary surface impedances. Furthermore, the surface impedance can also be changed by varying the dimension of the thin plate with the post dimensions fixed.

Figure 3.12: (a) Cross-sectional view of the structure. (b) The transverse resonance equivalent circuit.

Now from $\overset{\rightarrow}{\underline{Z}}_{x=t}$ in Eq. (3.19a) and Eq. (3.24), the TRM leads to the propagation constants in the high-impedance structure as

$$\overset{\rightarrow}{\underline{Z}}(x = t) + \overset{\leftarrow}{\underline{Z}}(x = t) = 0$$

$$\frac{|k_{x1}|}{\omega\varepsilon} \tanh(|k_{x1}|(h - t)) - \frac{W\,\eta_2 \tan(k_2 t)}{1 - \left(W\,\eta_2 \tan(k_x t) \cdot C_i\right)} = 0. \tag{3.25}$$

In a similar way as previously, $|k_{x1}|$ can be determined graphically or numerically. Note that with $C_i = 0$, the structure becomes the metal post structure, and then Eq. (3.25) is the same as Eq. (3.21).

Chapter 4

Application of PBG structures to an asymmetric parallel-plate waveguide Luneburg lens

In this chapter, the two PBG structures of the periodic and regular metal post structure and the corrugated surface are applied to an improved and modified parallel-plate Luneburg lens (PPLL) antenna, called an asymmetric parallel-plate waveguide Luneburg lens (APWLL) antenna. The complete APWLL antenna consists of an APWLL, a pair of rotationally symmetric corrugated flares, a primary feed. Far fields of the antenna are derived and design rules are presented.

4.1   Principle of parallel-plate Luneburg lens

A parallel-plate Luneburg lens should be satisfied with the following refraction index $n(r')$:

$$
\begin{aligned}
n(r') &= \sqrt{2 - (r')^2}, \quad 0 \leq r' \leq 1 \\
n(r') &= 1, \qquad\qquad\ \ r' \geq 1
\end{aligned}
\tag{4.1}
$$

44

where r' is the radius normalized by the radius of the lens r_0 [Lun64]. It is noted that the refraction index profile is inhomogeneous for $0 \leq r' \leq 1$, and the index of refraction is unity at $r' = 1$, so that a Luneburg lens is matched to free space. Since the phase velocity is proportional to $\frac{1}{n(r')}$, the profile of the refraction index in Eq. (4.1) implies that the phase velocity at the rim of the lens is higher than that in the middle.
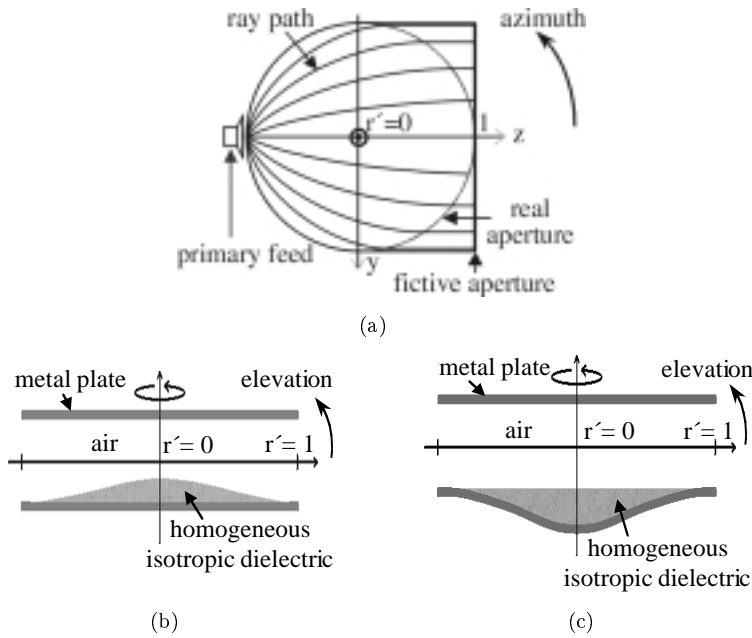

(a)

(b)　　　　　　　　　　　　　　　　　　(c)

Figure 4.1: Parallel-plate Luneburg lens. (a) Top view and the behavior of the propagating rays. Cross-sectional view (b) in case that the spacing of metal plates is constant [Han64] and (c) in case that the spacing is varied [Vog82]. The radius r' is normalized by the real lens radius r_0.

In Fig. 4.1(a), the behavior of the propagating rays is illustrated. Each ray propagates from a point located on the rim of the lens, called a focal point toward the fictive aperture in the opposite side. The rays which start from the focal point arrive at the fictive aperture at the same time since rays through the middle of the lens propagate slower than the rays at near the rim due to the above refraction index. Therefore, the parallel-plate Luneburg lens has the same phase at the fictive aperture. In other words, a plane wave leaves from

the lens.

In order to provide the refraction index in a PPLL, mostly a homogeneous isotropic dielectric is used [Han64], [Joh93]. In Figs. 4.1(b) and 4.1(c), the cross-sectional views embedded by a homogeneous isotropic dielectric are displayed. Air is filled in the rest of the dielectric in the parallel-plate waveguide. The thickness of the homogeneous isotropic dielectric in the lens is varied in a radial direction in order to satisfy $n(r')$.

4.2 Application of the regular and periodic metal posts

As mentioned in Ch. 1, the usage of a dielectric in the PPLL causes bad durability and weak contact on the interface between the dielectric and the metal plate. Therefore, the metallic PBG structure of the regular and periodic metal post structure is used instead of a homogeneous isotropic dielectric to get over the drawbacks of dielectric.

As described in Ch. 3, the PBG structure of the regular and periodic metal posts acts like a homogeneous artificial dielectric. Furthermore, since the PBG structure is made of metal and realized on the same plate as the metal plate of the parallel-plate waveguide, the metallic PBG structure provides the properties of strong durability, good contact and little dielectric loss.

4.2.1 Determination of metal post dimension

In order to utilize the metal post structure in the APWLL, the structure has to satisfy the required refraction index in Eq. (4.1). In Eq. (3.21), the relation of the post dimension and the refraction index has been derived. By inserting Eq. (4.1) into Eq. (3.21) and letting $\varepsilon_r = 1$ (see Fig. 3.5), Eq. (3.21) is expressed by

$$\sqrt{1-(r')^2}\tanh\left(k_0\sqrt{1-(r')^2}(h-t)\right) = W\tan(k_0 t). \tag{4.2}$$

The weighting factor W is determined by Eq. (3.18). Eq. (4.2) states that if W and h are given, the profile of the post height t for the index $n(r')$ is determined. Also with h and t given, the required weighting factor W is obtained for $n(r')$.

Here, the case of obtaining the metal post height t for $n(r')$ is considered. In order to fix the post height t, two cases are shown. The first is the spacing 'h =constant', the second is the spacing '$(h-t)$ =constant'.
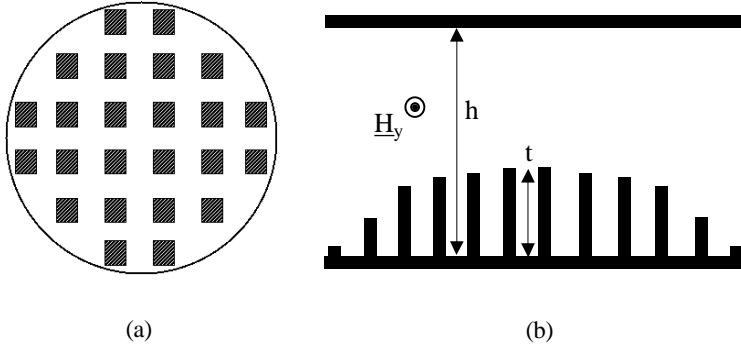
(a)   (b)

Figure 4.2: An APWLL with a square lattice and square posts in case of $h = $ constant.
(a) Top view. (b) Cross-sectional view.

4.2.1.1   h = constant

In Fig. 4.2, the top view and the cross-sectional view of the lens are displayed.
The APWLL has a square lattice and square posts. From Eq. (4.2), the post
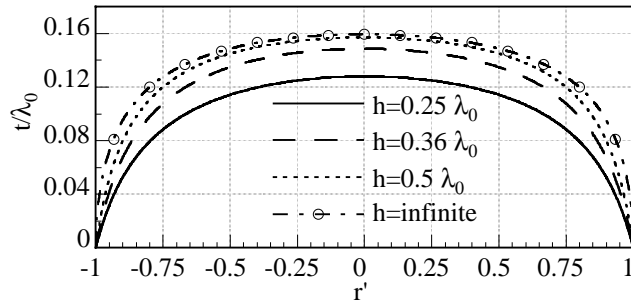height t is numerically obtained, with the weighting factor W fixed.

Figure 4.3: Variation of the post height for four different spacings of the plates h.
$P = 0.2\lambda_0$ and $D = 0.07\lambda_0$ ($W = 0.65$ by Eq. (3.8)).

Figure 4.3 shows the normalized post height t/λ_0 as a function of r' for
different plate spacing h. It is seen that the posts in the middle are tallest
whereas the ones at the rim are lower. With a smaller h, the maximum height
becomes lower and the profile of the height is sensitively changed despite a little
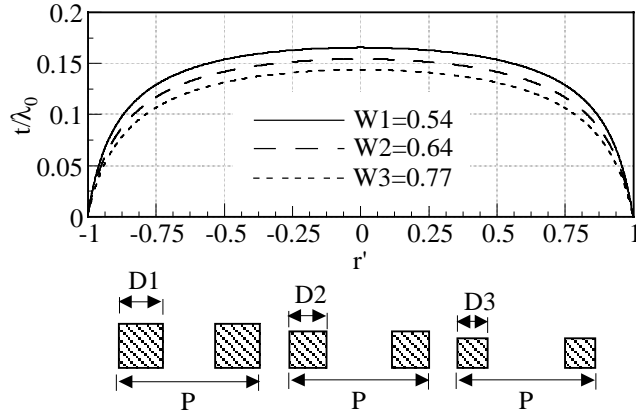
Figure 4.4: Variation of the post height for three different weighting factors W with the spacing of the plates $h = 0.48\lambda_0$ fixed. $P = 0.2\lambda_0$. Note that the width of the posts D is varied ($D1 > D2 > D3$).

variation of h. In other words, with a lower h, a little deviation of h during fabrication will seriously inflict the lens performance because a little deviation of h causes a large error of the post profile.

However, for $\frac{\lambda_0}{2} < h < \infty$, the entire profile is little changed. The reason is the behavior of the hyperbolic tangent function in Eq. (4.2). That is, if $(h - t)$ in Eq. (4.2) grows, the hyperbolic tangent function is converging to 1 (see appendix A). From the point of view of fields in the x direction, it means that the amplitude of the attenuated wave in the $+x$ direction $e^{|x|}$ is much larger than that of the reflected wave $e^{-|x|}$ since the wave in the $+x$ direction is completely bound to the PBG structure. Hence the impedance $\overrightarrow{Z}(x = t)$ in Eq. (3.19a) is

$$\overrightarrow{Z}(x = t) = \frac{jk_0\sqrt{n^2 - 1}}{\omega\varepsilon_0}. \tag{4.3}$$

Note that the hyperbolic tangent function has disappeared in Eq. (4.3). As a result, the post height t is independent of the variation of the spacing h, that is,

$$t(r') = \frac{\lambda_0}{2\pi}\tan^{-1}\left(\frac{\sqrt{1 - (r')^2}}{W}\right). \tag{4.4}$$

From the above reason, $h > \lambda_0/2$ is preferred in order to enhance the tolerance of the measurement and fabrication since the small deviation of the
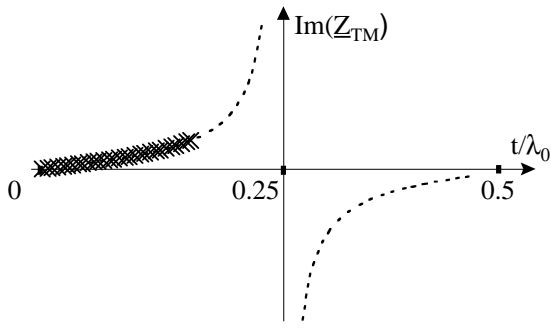
Figure 4.5: The surface impedance $\underline{Z}_\mathrm{TM}$ corresponding to the post heights for $W = 0.77$ in Fig. 4.4 (marked cross sign). The dotted line is the surface impedance as a function of the post height from Eq. (3.17).

spacing h in measurement and fabrication leads to little variation of the post profile and hence has little effect on the performance of the APWLL. Especially, in applications such as the ACC radar operating in the millimeter wave frequency range, the entire dimension (i.e. post height t and spacing h) is very small. Therefore, a small deviation of the spacing h in measurement and fabrication is acceptable by taking $h > \lambda_0/2$.

However, if $\lambda_0/2 < h$, higher-order modes near the rim of the lens may be excited. Therefore, in order to determine the appropriate spacing h in the design of an APWLL, both of the tolerance of h in fabrication and the suppression of higher-order modes in the lens must be considered.

In Fig. 4.4, the variation of the post height profile for different W (or different D) is displayed. It shows that with a larger W, the height in the middle becomes lower. The reason is that with a large W, metal posts will have more incident field between the posts and then more induced field on the posts. Therefore shorter posts are necessary in order to obtain the same surface impedance as that with a small W. For $W = 0.77$, the maximum height is about $0.14\lambda_0$.

As shown in Figs. 4.3 and 4.4, the profile of the posts' height is such that the post height decreases in the radial direction. Since the surface impedance is proportional to the height of the posts, the surface impedance decreases as well. Therefore, the rays in the center propagate slower than that off the center like the function of a homogeneous isotropic dielectric in the lens.

Using Eq. (3.17), the surface impedance $\underline{Z}_\mathrm{TM}$ for $n(r')$ is calculated. In Fig. 4.5, the surface impedance $\underline{Z}_\mathrm{TM}$ corresponding to the post height for

$W = 0.77$ in Fig. 4.4 is displayed with the marked cross signs ($\times$). Note that the marked range changes relatively smoothly. Hence it is possible in practice to get an almost exact arbitrary inductive surface impedance as a little variation of the height t effects little the surface impedance $\underline{Z}_{\mathrm{TM}}$. In contrast, with a smaller W, that is $D > P/2$, the posts are getting taller. Thus, the range of $\underline{Z}_{\mathrm{TM}}$ for the posts is located in the region where $\underline{Z}_{\mathrm{TM}}$ cannot be exactly achieved due to its sensitivity of the t variation.

4.2.1.2 $(\mathbf{h} - \mathbf{t}) = \mathbf{constant}$

In Fig. 4.6, an APWLL with constant $(h - t)$ is displayed. The top view is identical to one of $h = $ constant, whereas the cross section is different. Using Eq. (4.2) and letting $(h - t)=$constant, the analytical solution for the post height t is derived:

$$t(r') = \frac{\lambda_0}{2\pi} \tan^{-1}\left(\frac{\sqrt{1 - (r')^2}}{W} \tanh\left(\frac{2\pi}{\lambda_0}\sqrt{1 - (r')^2}(h - t)\right)\right). \qquad (4.5)$$

In Fig. 4.7, the post profiles for four different cases of $(h - t)$ calculated by Eq. (4.5) are plotted. It shows that the variation of $(h - t)$ has only a little influence on the profiles. The reason is that if $(h - t)$ is larger than about $0.3\lambda_0$, the hyperbolic tangent function approaches 1 (see Appendix A). But for both cases $h = $ constant and $(h - t) = $ constant, the tallest posts are located in the middle.
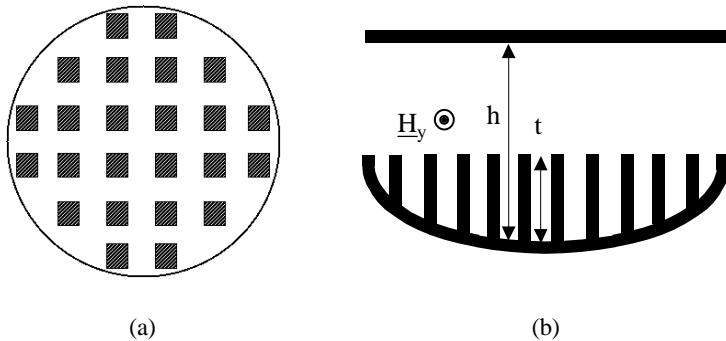

Figure 4.6: An APWLL with a square lattice and square posts in case of $(h - t) = $ constant. (a) Top view. (b) Cross-sectional view.
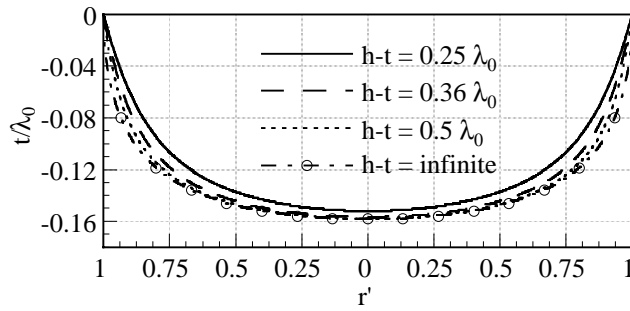
Figure 4.7: The variation of the post heights for different spacing $(h - t)$. P=$0.2\lambda_0$ and $D = 0.07\lambda_0$. Note that $(h - t)$ is varied.

The influence of the weighting factor W (or post dimensions D) is shown in Fig. 4.8. The entire profiles are proportional to the decrease of W like the case $h = $ constant shown in Fig. 4.4.

4.2.2   Far-field calculation of the APWLL

Figure 4.9 illustrates the procedure for calculating the far field of the lens. The total far-field calculation is divided into two steps. First, the aperture field of the APWLL $\underline{E}_a(y)$ is determined by GO using the far field of the primary horn $\underline{E}_p(\zeta)$ [Vog82], [McN90]. Second, the far field of the APWLL is calculated with the help of the aperture field integration method using the aperture field [Pee53a], [Bal97].

4.2.2.1   Aperture field

The Finite Element Method (FEM) can be used for calculating the aperture field of a PPLL, too [Gre99]. As the lens is usually several wavelengths long, the efficiency of an FEM calculation is low. On the other hand, geometrical optics (GO) is quite fast. Thus, GO is selected although the aperture fields are approximately predicted due to the assumption that the focal point of the lens should be placed in the middle of the aperture of a practical feed.

In Fig. 4.9, the geometry of the lens is displayed for calculating the aperture field. In the lens, ray tubes are illustrated. The angle ζ is used to describe the lens with the radius r_0 and the rays. $d\zeta$ is the differential increment of the angle ζ. The differential increments of x and y are denoted dx and dy,
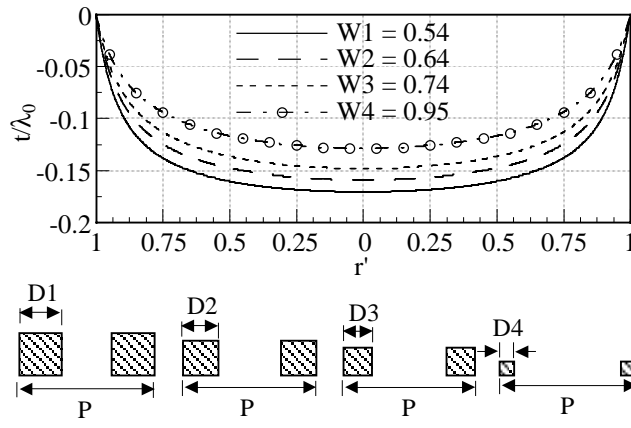
Figure 4.8: The variation of the post height for different factors W with a constant spacing $(h - t) = 0.48\lambda_0$. $P = 0.2\lambda_0$. The width of the posts D is varied $(D1 > D2 > D3 > D4)$.

respectively.

From principles of GO [Kli65], [Lee78], [McN90] it can be shown that the energy flow is along rays. The energy flow through a ray tube at the feed is $S_p(x,\zeta)dxd\zeta$, where $S_p(x,\zeta)$ is the energy distribution per unit angle area $(dxd\zeta)$ in the primary pattern of the feed. In the same way, the energy flow through the ray tube at the aperture is expressed by $S_a(x,y)dxdy$, where $S_a(x,y)$ is the energy distribution per unit area $(dxdy)$ at the aperture.

Since S_a and S_p are the magnitude of the Poynting vector at the feed and at the aperture, it is proportional to the square of the magnitude of the electric field $\underline{E}_a$ at the aperture and $\underline{E}_p$ at the feed, respectively. Additionally, it will be assumed that S_a is a separable function of x and y and S_p a separable function of x and ζ. Thus,

$$
\begin{aligned}
S_a(x,y)dxdy &= |\underline{E}_a(x)|^2|\underline{E}_a(y)|^2dxdy \\
S_p(x,\zeta)dxd\zeta &= |\underline{E}_p(x)|^2|\underline{E}_p(\zeta)|^2dxd\zeta.
\end{aligned}
\tag{4.6}
$$

Since the energy flow should be conserved through various cross sections normal to a ray tube, $S_a(x,y)dxdy = S_p(x,\zeta)dxd\zeta$. That is,

$$
|\underline{E}_a(x)|^2|\underline{E}_a(y)|^2dxdy = |\underline{E}_p(x)|^2|\underline{E}_p(\zeta)|^2dxd\zeta.
\tag{4.7}
$$

From Fig. 4.9, the relation between y and ζ is obtained:
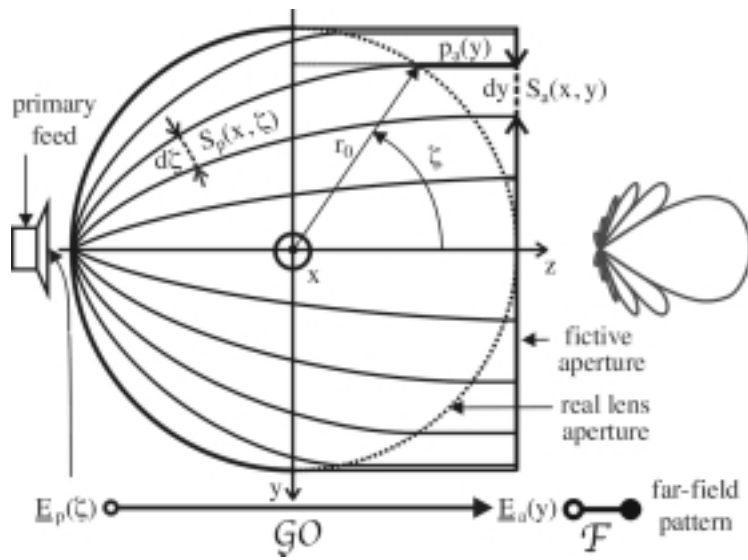
$$
y = r_0 \sin(\zeta).
\tag{4.8a}
$$

Figure 4.9: Geometry of a parallel-plate Luneburg lens for the calculation of the aperture field with the aid of GO and calculation procedure of far fields.

Then,

$$dy = r_0 \cos(\zeta)d\zeta. \tag{4.8b}$$

Substituting dy into Eq. (4.7) results in

$$|\underline{E}_a(y)| = \frac{1}{\sqrt{r_0 \cos(\zeta)}} \cdot |\underline{E}_p(\zeta)| \tag{4.9}$$

where $\underline{E}_p(\zeta)$ is the far field of the primary feed. It is noted that the amplitude of the aperture field in the y direction, $|\underline{E}_a(y)|$, is subject to the angle ζ and the amplitude of the far field of a primary feed, $|\underline{E}_p(\zeta)|$.

In order to obtain the phase difference between the fictive aperture and the real aperture, the distance $p_a(y)$ has to be calculated. By assuming that a plane wave at the fictive aperture is left, the distance is

$$p_a(y) = r_0(1 - \cos(\zeta)). \tag{4.10}$$

As a result, by combining Eqs. (4.9) and (4.10), the aperture fields at the real

aperture are

$$\vec{E}_a(x,y) = \underline{E}_a(x,y)\hat{x}$$
$$= \underline{E}_a(x)\underline{E}_a(y)\hat{x} = \underline{E}_a(x)|\underline{E}_a(y)|e^{jk_0\,p_a(y)}\hat{x} \qquad (4.11\mathrm{a})$$

$$\vec{H}_a(x,y) = \frac{1}{\eta_0}\underline{E}_a(x,y)\hat{y}$$
$$= \frac{1}{\eta_0}\underline{E}_a(x)|\underline{E}_a(y)|e^{jk_0\,p_a(y)}\hat{y}. \qquad (4.11\mathrm{b})$$

As an example, a H-plane sectoral horn for a primary feed is considered. The width and height of the H-plane sectoral horn are λ_0 and $\lambda_0/4$. Using the formula for the far field of the horn in [Bal97], the field $\underline{E}_p(\zeta)$ is calculated. In Fig. 4.10(a), the far field of the horn and the aperture field distribution calculated by Eq. (4.9) are plotted. In practice, the energy in Fig. 4.10(b) may not disappear abruptly at $|\zeta| = 90°$. This is due to the approximation of GO.
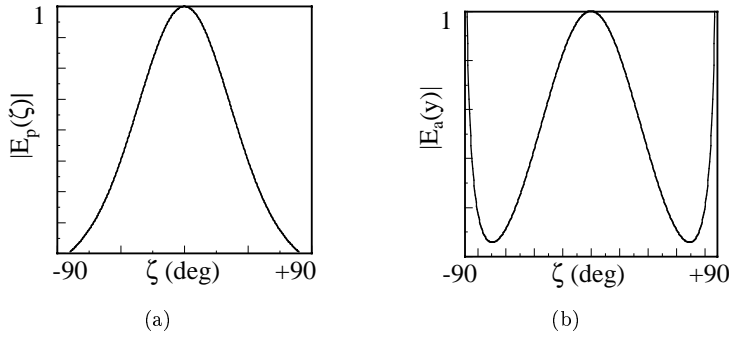

Figure 4.10: (a) Far field of the H-plane sectoral horn. (b) Field distribution at the lens aperture.

4.2.2.2 Far-field calculation

With the aperture field in Eq. (4.11), the far fields of the lens are derived with the aid of the aperture field integration method [Yam96], [Bal97]. The procedure of the derivation is described in appendix B in detail. Here, only the

results are written:

$$\underline{E}_\theta = \frac{jr_0k_0e^{-jk_0R}}{4\pi R}\int_{-\frac{x_0}{2}}^{\frac{x_0}{2}}\int_{-\frac{\pi}{2}}^{\frac{\pi}{2}}\underline{E}_a(x,y)\cos(\zeta)\cos(\psi)(1+\cos(\theta))\cdot$$

$$e^{jk_0\hat{e}_r\cdot\vec{\rho}}dxd\zeta \tag{4.12a}$$

$$\underline{E}_\psi = \frac{-jr_0k_0e^{-jk_0R}}{4\pi R}\int_{-\frac{x_0}{2}}^{\frac{x_0}{2}}\int_{-\frac{\pi}{2}}^{\frac{\pi}{2}}\underline{E}_a(x,y)\cdot$$

$$(\cos(\zeta)\sin(\psi)(1+\cos(\theta))-\sin(\theta)\sin(\zeta))e^{jk_0\hat{e}_r\cdot\vec{\rho}}dxd\zeta \tag{4.12b}$$

and

$$\underline{H}_\theta = -\frac{\underline{E}_\psi}{\eta} \tag{4.12c}$$

$$\underline{H}_\psi = \frac{\underline{E}_\theta}{\eta} \tag{4.12d}$$

where

$$\hat{e}_r\cdot\vec{\rho}=x\sin(\theta)\cdot\cos\psi-r_0\sin(\zeta)\cdot\sin(\theta)\cdot\sin(\psi)+r_0\cos(\zeta)\cdot\cos(\theta). \tag{4.12e}$$

Now with Eq. (4.12a) and Eq. (4.12b), H-plane ($\psi = 90°$) and E-plane ($\psi = 0°$) patterns are derived respectively as follows:

H-plane pattern with $\psi = 90°$:

$$\underline{E}_\theta = 0 \tag{4.13a}$$

$$\underline{E}_\psi = \frac{-jr_0k_0e^{-jk_0R}}{4\pi R}\int_{-\frac{x_0}{2}}^{\frac{x_0}{2}}\int_{-\frac{\pi}{2}}^{\frac{\pi}{2}}\underline{E}_a(x,y)(\cos(\zeta)(1+\cos(\theta))-\sin(\theta)\sin(\zeta))\cdot$$

$$e^{jk_0(-r_0\sin(\zeta)\cdot\sin(\theta)+r_0\cos(\zeta)\cdot\cos(\theta))}dxd\zeta. \tag{4.13b}$$

E-plane pattern with $\psi = 0°$:

$$\underline{E}_\theta = \frac{jr_0k_0e^{-jk_0R}}{4\pi R}\int_{-\frac{x_0}{2}}^{\frac{x_0}{2}}\int_{-\frac{\pi}{2}}^{\frac{\pi}{2}}\underline{E}_a(x,y)\cos(\zeta)(1+\cos(\theta))\cdot$$

$$e^{jk_0(x\sin(\theta)+r_0\cos(\zeta)\cdot\cos(\theta))}dxd\zeta \tag{4.14a}$$

$$\underline{E}_\psi = 0. \tag{4.14b}$$

Note that $\underline{E}_\psi = 0$ because $\underline{E}_\psi$ in Eq. (4.12b) is an odd function with respect to $\psi = 0°$. The far-field patterns are obtained numerically.

4.3   Application of corrugated surfaces

As discussed in Sec. 3.1, corrugated surfaces have an ability in suppressing surface waves. In this section, the property of a corrugated surface is applied to build a pair of rotationally symmetric corrugated flares added to the APWLL. With the flares, the performance of the APWLL in elevation is improved in terms of side lobe levels and a HPBW.

Up to now, there has not been any analytical or approximate approach to design the rotationally symmetric corrugated flares for the Luneburg lens available. Therefore, the new approach of using the corrugated flares and the design procedure presented in this section are absolutely novel and useful.

4.3.1   Property and design of a pair of rotationally symmetric corrugated flares

In [Pee53a], the improvement of a microwave Luneburg lens in elevation was attempted using a pair of rotationally symmetric plane flares as shown in Fig. 4.11. However, as the polarization of the lens in [Pee53a] is perpendicular to the rotational axis of the lens, namely horizontal, the flares cannot be adapted to the APWLL which has a vertical polarization.

Recently, Vogel presented an asymmetric sandwich lens, a kind of a PPLL added by a pair of rotationally plane flares [Vog82], [Vog83] for a mechanical scanning. The lens has a vertical polarization like the APWLL. However, as described in [Vog82], the extended plane flares badly influence the performance of the lens in azimuth.

In order to verify the performance of the APWLL fed by a pair of rotationally symmetric plane flares in elevation, a pair of plane flares is fabricated and measured. A end-fire waveguide is used for a primary feed. Therefore, the antenna has a constant field distribution in elevation. In Fig. 4.11(a), the APWLL with a pair of rotationally symmetric plane flares is displayed. The measured pattern of the APWLL is plotted in Fig. 4.11(b). As expected, the antenna has a higher side lobe levels due to a constant field distribution in elevation.

Here a pair of rotationally symmetric corrugated flares is proposed to modify the constant field distribution. In Fig. 4.12, the corrugated flares are illustrated. They seem to be a biconical antenna. The circularly-shaped corrugations are periodically engraved on the metal flares. Due to their rotational symmetry, the complete antenna preserves the properties of the APWLL in azimuth, especially, a large scan angle and multiple beam.
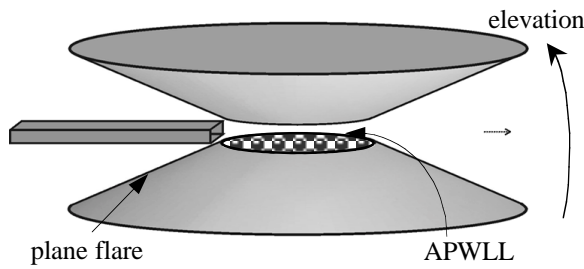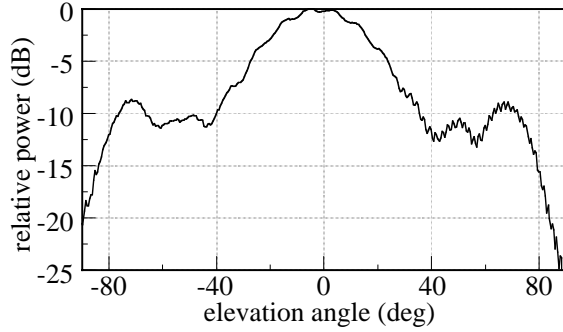
Figure 4.11: (a) Illustration of an APWLL antenna added to plane flares. (b) Far-field pattern in elevation.

For using the corrugated flares, an additional important property of the corrugated surface mentioned in Ch. 3 is used. It is that the type of the surface impedance still becomes capacitive for the depth of the corrugations of between $\lambda_0/4$ and $\lambda_0/2$ whereas the corrugated surface works in an anisotropic way. In fact, as shown in Fig. 4.12, the corrugated surface is not perpendicular to the direction of wave propagation. This fact leads to the variation of the weighting factor W in Eq. (3.8). However, due to the above reason, the corrugated flares stop the surface wave on the flares' surface.

As shown in Fig. 4.12(b), a corrugated flare is determined by the flare length ρ_e and the flare angle θ_e. A cutoff ring is placed to suppress higher-order modes around the rim of the APWLL. Each corrugation has the same tooth thickness D and the period P. The depth of the corrugation is between $\lambda_0/4$ and $\lambda_0/2$. For the design of the corrugations, the design procedure of the corrugations for
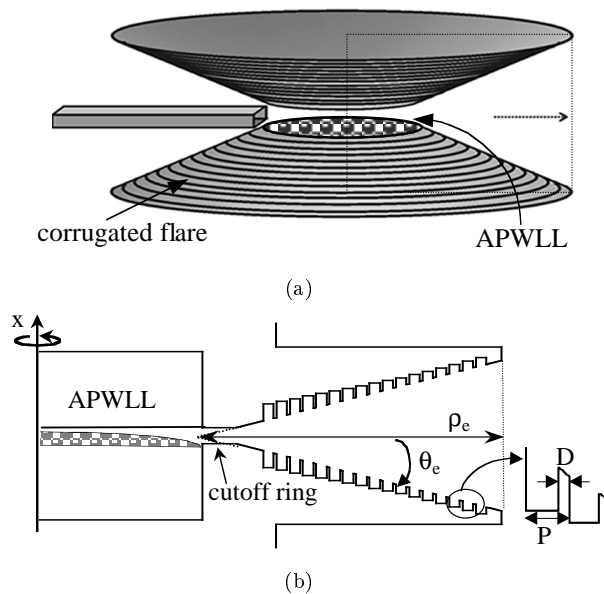
(a)

(b)

Figure 4.12: (a) A complete antenna with the APWLL and the corrugated flares. (b) Cross-sectional view of the complete antenna.

a corrugated horn is followed [Law66], [Men74], [Lov76], [Cla84].

As mentioned in Sec. 3.1, if the depth of the corrugation is between $\lambda_0/4$ and $\lambda_0/2$, the corrugated surface becomes capacitive and hence stops TM surface waves on the corrugated surface. Therefore, the energy on the surface is added to that in the middle since the field on the corrugated surface cannot exist. From the above reasons, a cosine distribution is achieved by the corrugated flares, at the same time little edge diffraction occurs at the end of the flares. As a result, the APWLL has a very low side lobe level and a desired HPBW.

4.3.2   Far-field calculation of the corrugated flares

In order to compute the far fields of the flares, the aperture fields which are available in the corrugated pyramidal horns are used [Men76]. This method is reasonable since both the symmetric corrugated flares and a corrugated horn produce a cosine field distribution at the aperture due to their corrugated surfaces as illustrated previously. Also, as shown in Fig. 4.13, the cross section of a corrugated pyramidal horn is nearly similar to the one in Fig. 4.13(b).
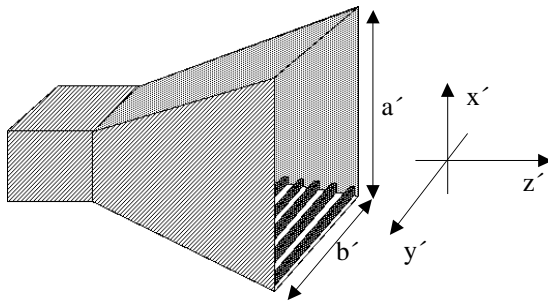
(a)
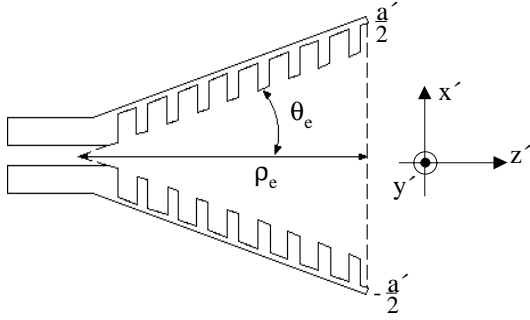
(b)

Figure 4.13: (a) Geometry of a corrugated pyramidal horn. (b) Its cross-sectional view.

Moreover, as shown in Fig. 4.9, the ray paths at the fictive aperture are parallel to each other and bound into the fictive aperture of the APWLL. Especially, with much larger flares than the radius of the APWLL, the flares is quite similar to the horn. As a result, the far-field patterns of the two cases will be nearly the same in elevation.

The complete derivation of the far fields is given in appendix C. Here, only the far-field pattern in E-plane is presented.

$$\underline{E}_\psi = 0 \tag{4.15a}$$

$$\underline{E}_\theta = jk_0 \frac{e^{-jk_0 R}}{2\pi R} E_0 \underline{A} \cdot \underline{B}\Big|_{\psi=0^\circ} \tag{4.15b}$$

where

$$\underline{A} = \frac{1}{2}\sqrt{\frac{\pi\rho_e}{k_0}}\left[e^{j\frac{\rho_e}{2k_0}\left(\frac{\pi}{a'}+k\sin(\theta)\right)^2}\left(C(t_2) - jS(t_2) - C(t'_2) + jS(t'_2)\right)\right.$$

$$\left.+e^{j\frac{\rho_e}{2k_0}\left(\frac{\pi}{a'}-k\sin(\theta)\right)^2}\left(C(s_2) - jS(s_2) - C(s'_2) + jS(s'_2)\right)\right]_{\psi=0°} \quad (4.15c)$$

$$\underline{B} = \int_{y'} \underline{E}_{ax}(y')dy'. \quad (4.15d)$$

As explained in appendix C, at $\psi = 0°$ (E-plane), the term $\underline{B}$ is independent of the angle θ. For the numerical calculation of the far-field pattern, the approximation of the Fresnel integrals is used (see the appendix C.2) and the variables are transformed as follows:

$$t_2 = 2\sqrt{T_e}\left(1 - \frac{V_e}{4T_e} - \frac{1}{8T_e}\right)$$

$$t'_2 = 2\sqrt{T_e}\left(-1 - \frac{V_e}{4T_e} - \frac{1}{8T_e}\right)$$

$$s_2 = 2\sqrt{T_e}\left(1 + \frac{V_e}{4T_e} - \frac{1}{8T_e}\right)$$

$$s'_2 = 2\sqrt{T_e}\left(-1 + \frac{V_e}{4T_e} + \frac{1}{8T_e}\right) \quad (4.16a)$$

where

$$T_e = \frac{1}{8}\left(\frac{a'}{\lambda_0}\right)^2 \cdot \frac{1}{\rho_e/\lambda_0}$$

$$V_e = \frac{a'}{\lambda_0}\sin(\theta). \quad (4.16b)$$

Therefore, with the horn dimension ρ_e and a' given, the E-plane pattern is computed from Eq. (4.15).

Chapter 5

Verification and measurement in 76-77 GHz range

In the previous chapter, a periodic and regular metal post structure is used for an APWLL instead of a homogeneous isotropic dielectric. Also, a corrugated surface with its property of suppressing surface waves is applied for the design of the corrugated flares of the APWLL antenna. In this chapter, the properties of the PBG structures and the design procedures of the APWLL antenna are verified. For verification, APWLLs are simulated by HFSS and two APWLL antennas for an ACC radar at 76.5 GHz are designed and measured.

5.1 Simulation and design of an APWLL antenna at 76.5 GHz

First, the far field of the APWLL is computed at 76.5 GHz using the result in Sec. 4.2.2. With the help of the calculation, the appropriate dimensions of the feed and the APWLL are chosen for a desired HPBW and side lobe levels. In order to show the isotropy of the lattices and the shapes of the metal posts proposed in Ch. 3, the APWLLs with the lattices and the post shapes are simulated with the aid of HFSS and then the performances of the lattices are evaluated. Also, the influences of the post shapes and the post dimensions on the far-field pattern are investigated. In Figs. 4.2 and 4.6, two ways of the realization of regular and periodic metal posts are described for the application to the APWLL. Here since the way in Fig. 4.2 has clearly the low profile, the

case of constant spacing is selected for the design of APWLLs.

Second, the far field of the corrugated flares is computed at 76.5 GHz, and then using the result, the proper dimensions of the corrugated flares are selected.

5.1.1 Determination of the dimensions of the feed and lens

A far field of an APWLL in H-plane (in azimuth) is directly influenced by the far field of a primary feed $\underline{E}_p(\zeta)$ as described in Sec. 4.2.2. Therefore, in order to determine the proper dimensions of the feed and the lens for a desired pattern, the relation between the dimensions of the primary feed and the lens and the far field should be investigated in advance.

Here a H-plane sectoral horn is selected as a primary feed. As shown in Fig. 5.1(a), the feed horn is determined by a flare length ρ and an aperture width a. Since the electric field distribution of the horn in the x direction $\underline{E}_p(x)$ (see Eq. (4.7)) is constant, it is assumed that the electric field distribution of the lens aperture in the x direction $\underline{E}_a(x)$ (see Eq. (4.11)) is also constant in calculating far fields.

As the first prototype, an APWLL of a 50 mm diameter ($2r_0 = 12.75\lambda_0$, $\lambda_0 = 3.92$ mm) is designed. In Fig. 5.1(a), the far-field calculation's procedure of the complete antenna system is displayed. With Eq. (4.13b), the radiation pattern in H-plane is computed at 76.5 GHz. Figure 5.1(b) shows HPBWs and first side lobe levels as functions of the horn dimensions. The dashed line points out an equi-HPBW while the solid line is an equi-first side lobe level.

Also it shows that as the aperture width of the feed horn a and the flare length ρ are growing, first side lobe levels become lower, while HPBWs get larger. To explain the reason, the influence of feed dimension on the field distribution of the real lens and feed horn is displayed in Fig. 5.2. Figure 5.2(a) shows that with larger a, the field of the feed horn at the edge is reduced. Further, the shape of current distribution in the middle is getting narrower since the directivity of the feed horn increases with larger a. The facts of lower edge field and narrower current distribution have a direct effect on the field distribution of the real lens aperture. That is, as is shown in Fig. 5.2(b), with larger a, the edge field of the lens which mainly leads to higher side lobe level of radiation pattern of the APWLL is lower [Tay55], [Joh93] and the field distribution near the middle of the lens is getting closer to the $\cos^n$ form distribution. As a result, with primary feeds of higher gain and lower side lobe, the APWLL supports larger HPBW and lower side lobe levels. In [San95], a
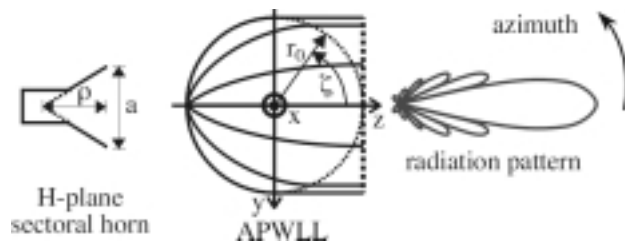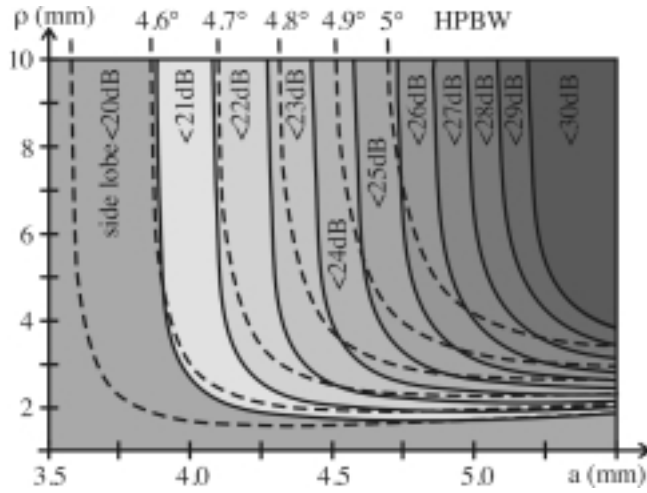
Figure 5.1: (a) Illustration of the APWLL antenna for the calculation of the far field: a H-plane sectoral horn and an APWLL. (b) HPBW and first side lobe level as a function of the feed horn dimensions for 50 mm APWLL.

couple of techniques for proper primary feeds are described in case of spherical Luneburg lens in order to reduce side lobe level.

However, for a practical determination of the proper dimensions of the feed horn, it should be considered that if $\rho < a$, the feed horn will have high reflection and serious phase errors as well. It means that ρ should be larger than a. For $\rho > a$, Fig. 5.1(b) shows that the variation of a has a main influence on the lens performance of a HPBW and a first side lobe level.

As a prototype, a H-plane sectoral horn for the 50 mm APWLL which has a HPBW of 4.5° and the first side lobe < -19 dB in azimuth is designed.
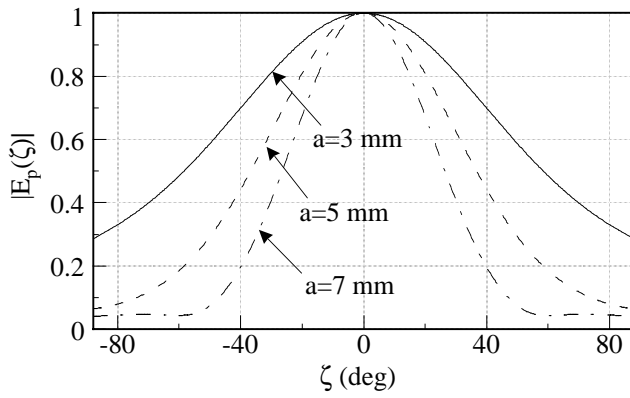
(a)
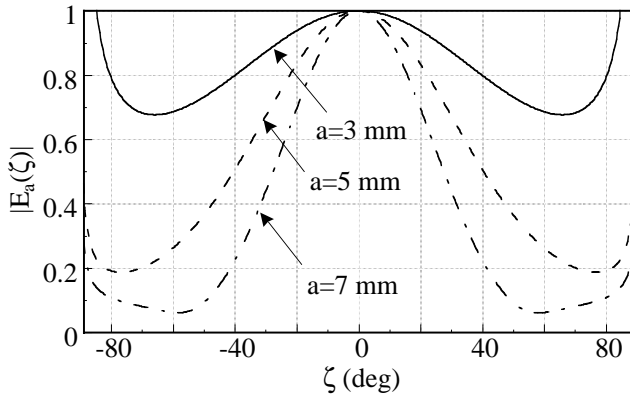
(b)

Figure 5.2: Influence of the feed horn on the field distribution of the feed horn and the lens aperture with $\rho = 15$ mm. (a) Field distribution at the feed aperture. (b) Field distribution at the real lens aperture (see Fig. 4.9 for the real lens aperture.).

Using the simulation result in 5.1(b), a H-plane sectoral horn of $a = 3.6$ mm and $\rho = 10$ mm is determined for a primary feed. In Fig. 5.3, the simulated far-field pattern for the 50 mm APWLL is shown.

In Fig. 5.4, the influence of the lens radius r_0 is shown with the horn dimensions fixed. Note that the patterns are normalized. The variation of the lens radius has little influence on the first side lobe level.
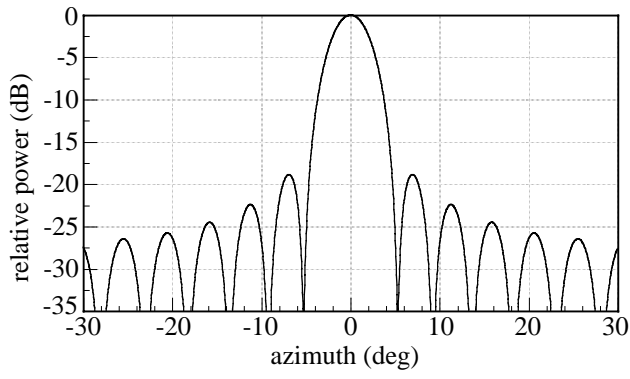
Figure 5.3: Simulated H-plane radiation pattern of the 50 mm APWLL with $a = 3.6$ mm and $\rho = 10$ mm (see Fig. 5.1).
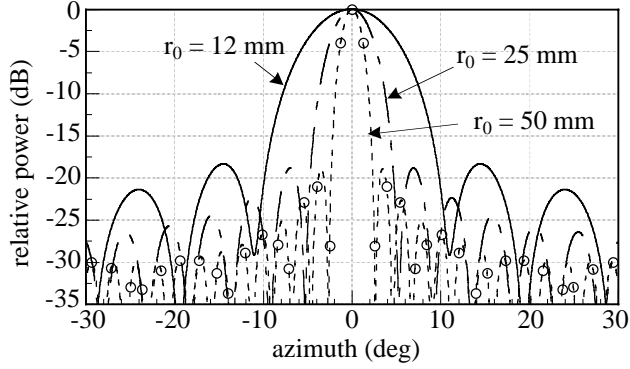

Figure 5.4: Influence of the lens radius on the far-field pattern for $a = 3.6$ mm and $\rho = 15$ mm.

In Tab. 5.1, the comparison of the three cases is conducted. On the base of the table, the beam factor ($BF_{\text{sim:H}}$) is derived and used later to approximately predict the required dimension of the APWLL for a desired HPBW. That is,

$$BF_{\text{sim:H}} = \theta_{\text{HPBW}} \times \frac{2 \times r_0}{\lambda_0} = 56.6°. \tag{5.1}$$

It is noted that Eq. (5.1) is valid for only the feed horn dimension $a = 3.6$ mm and $\rho = 15$ mm.

Table 5.1: HPBWs and first side lobes for different radii r_0

	radii r_0 (see Fig. 5.1)		
	12 mm	25 mm	50 mm
HPBW (°)	9.2°	4.44°	2.22°
first side lobe	-18.4 dB	-18.8 dB	-18.9 dB

In Sec. 4.2, the influence of the deviation of the parallel-plate spacing h on the metal post profile is investigated. According to the results, the spacing of the parallel-plate $h = 1.9$ mm ($< \lambda_0/2$) is chosen to in order to a) reduce the sensitivity by the deviation of the spacing in fabrication and b) suppress higher modes near the rim of the APWLL.

5.1.2 Determination of post dimensions and proper lattices

5.1.2.1 Post dimensions

In determining the proper post dimensions, the requirements explained in the previous chapters should be considered. First, as described in Ch. 3, the period $P \ll \lambda_0$ and the width of the posts $D < P/2$ are required for the TEM mode in the PBG. Second, in Ch. 4, $D \ll P/2$ is recommended to avoid the side effect caused by the top surface of the posts such as parasitic capacity and so on. However, for the mechanical stability in fabrication, the width D may not be so small at 76.5 GHz.

By considering the above conditions, first, $P = 0.78$ mm ($0.2\lambda_0$) is determined. In order to decide the width of the posts D, the influence of D on the radiation pattern of the APWLLs is investigated for a square lattice with square posts with the aid of HFSS. Three different cases of the width are chosen for the simulation. The first is $D = 0.28$ mm ($W = 0.64$ from Eq. (3.18)), which is smaller than $P/2$. The second is $D = 0.36$ mm ($W = 0.54$), which is nearly equal to $P/2$. The last is $D = 0.44$ mm ($W = 0.44$), which is larger than $P/2$.

In Fig. 5.5, the geometry of an APWLL for the simulation is shown for $D = 0.36$ mm is shown. An APWLL's diameter of $5.1\lambda_0$ is chosen. By considering the spacing of the parallel-plate waveguide $h = 1.9$ mm, the height of the feed horn is fixed to 1.9 mm.

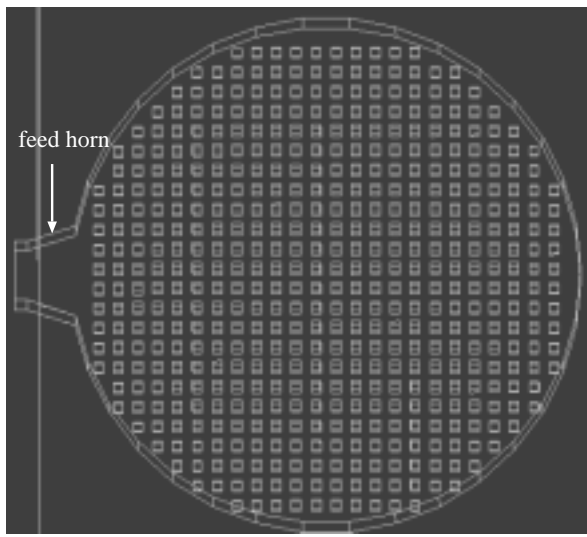Figure 5.6 shows the simulation results. As is shown, both cases of

Figure 5.5: Geometry of an APWLL with a square lattice and square posts for the simulation by HFSS.
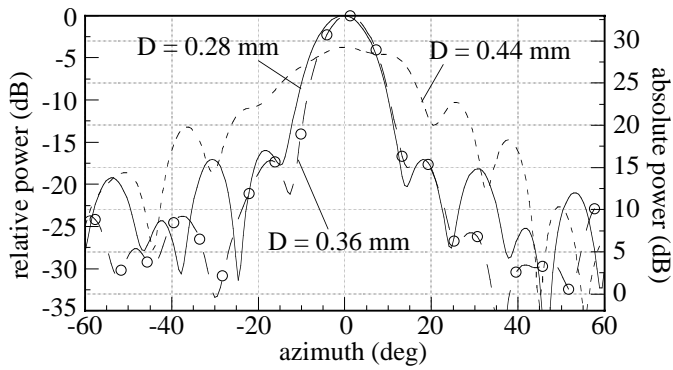

Figure 5.6: Simulation results of APWLLs for different post width D with a constant period $P = 0.78$ mm.

$D = 0.28$ mm and $D = 0.36$ mm differ little. However, with $D = 0.44$ mm, the property of the APWLL comes to much worse than two cases. As a result, it is recommended that the post widths within these ranges of the weighting

factor $W > 0.5$ and the period $P \ll \lambda_0$ should be determined.

For the next simulations, the proper dimension of the square metal posts is determined to $P = 0.78\,\mathrm{mm}$ and $D = 0.28\,\mathrm{mm}$, so that $W = 0.64$. In simulation of circular metal posts and hexagonal metal posts, $P = 0.78\,\mathrm{mm}$ and $D = 0.38\,\mathrm{mm}$ are used, so that $W = 0.62$ and $W = 0.58$. Using the above dimensions, the profile of post height is computed numerically by Eq. (4.2).

In Fig. 5.7, the profiles for the two cases are presented. Note that the
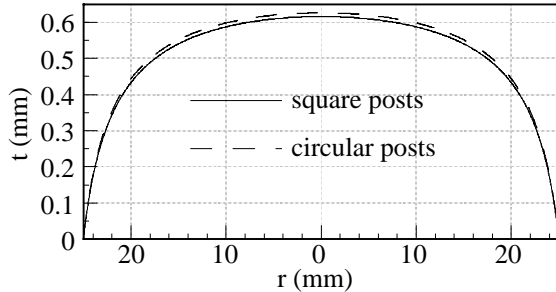

Figure 5.7: Post profiles for the square posts $D = 0.28\,\mathrm{mm}$ and the circular posts $D = 0.38\,\mathrm{mm}$ with $P = 0.78\,\mathrm{mm}$. The profiles are extremely exaggerated.

height is extremely exaggerated. For the circular posts, the tallest post is $0.626\,\mathrm{mm}$ in the middle of the APWLL while for the square posts, the tallest post is $0.616\,\mathrm{mm}$.

5.1.2.2   Proper lattices for an isotropy

To realize a wide beam scanning, an isotropy of the PBG structure is strongly required, so that the performance of the APWLL should be independent of scan angles or feed position. It is mentioned in Ch. 3 that the isotropy is related to a lattice of the metal post structure and such lattices as hexagon, square, and triangle are proposed as reasonable lattices for an isotropy. In order to evaluate each lattice, the APWLLs with the above three lattices are simulated for a couple of different scan angles with HFSS. In simulation, the operating frequency is $76.5\,\mathrm{GHz}$ and a H-plane sectoral horn $3.6\,\mathrm{mm} \times 1.9\,\mathrm{mm}$ is used.

In simulations, it is possible to examine the beam scanning of the APWLL by two ways. One is to turn the feed horn with the posts fixed. The other is to turn the complete posts, with the horn fixed. In simulation, the second method is selected. Also, later in measurement, the second way is selected to prove the isotropy of the metal post structure by showing the property of beam
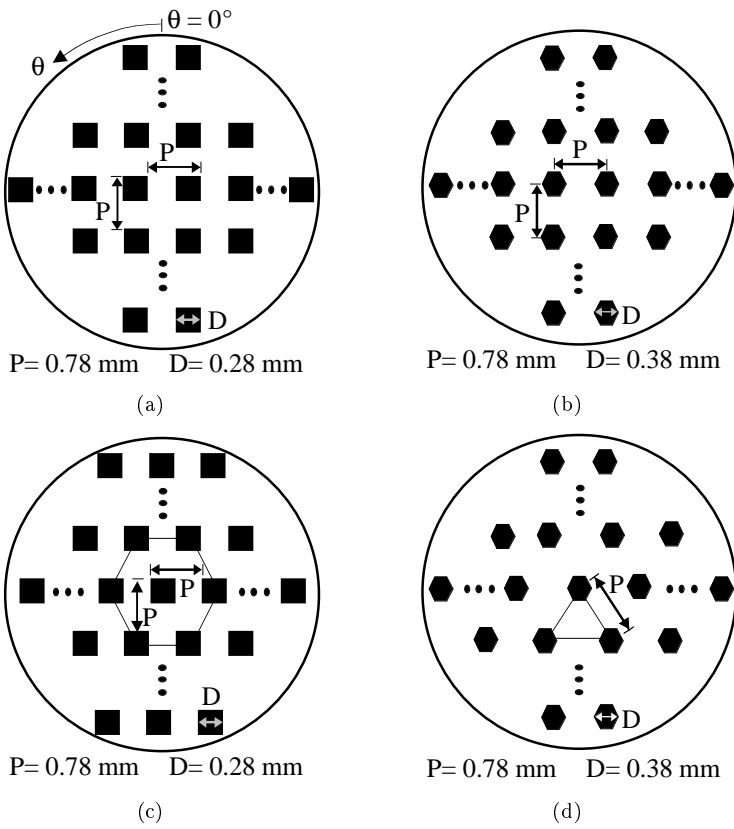
Figure 5.8: Examples of isotropic structures. (a) Square lattice with square posts. (b) Square lattice with hexagonal posts. (c) Hexagonal lattice with square posts. (d) Triangular lattice with hexagonal posts.

scanning.

In Fig. 5.8, top views of four APWLLs with three lattices and two different shapes of the metal posts at a scan angle $0°$ are presented. The diameter of the three APWLLs is fixed to $5.1\lambda_0$. They are simulated at a scan angle of $\theta = 6°$. In simulation, the metal posts are rotated by an angle $6°$ with the horn fixed.

In Fig. 5.9, the H-plane radiation patterns of the above cases are plotted. The simulations show that the hexagonal lattice with square posts points out about $3\,\mathrm{dB}$ higher first side lobe than the others whereas all patterns have
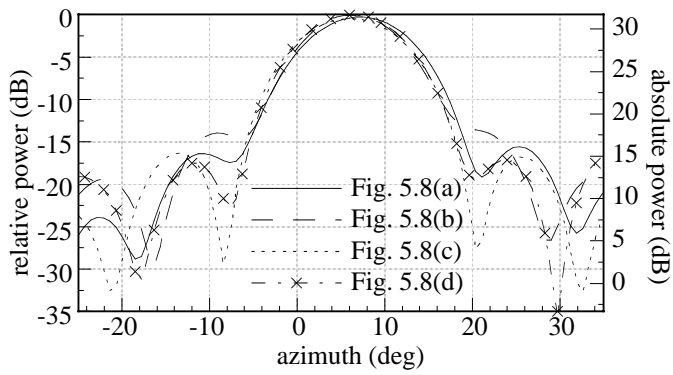
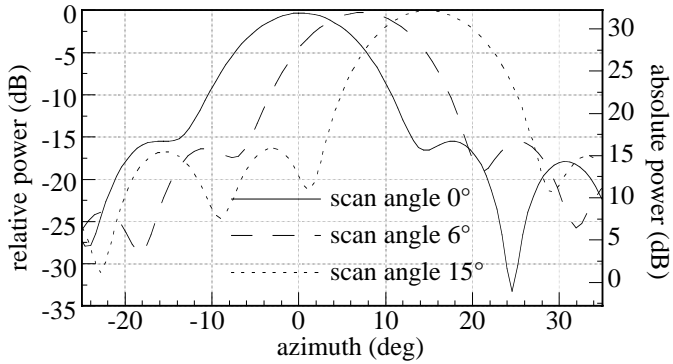Figure 5.9: *H*-plane radiation patterns of the APWLL in Fig. 5.8 simulated by HFSS.

Figure 5.10: *H*-plane radiation patterns of the APWLL with the square lattice and square posts for different scan angles.

about 11.5° HPBW.

In order to verify a wide scan angle of the APWLL, the APWLL in Fig. 5.8(a) is simulated at two more different scan angles of 0° and 15°.

Figure 5.10 shows the radiation pattern in *H*-plane. The three patterns differ little depending on scan angles. As a result, from Figs. 5.9 and 5.10, it is found that the APWLLs with the lattices are capable of guiding a wave in the APWLLs, independent of the feed position. Therefore, the metal post structure with the lattices support the isotropy. The results lead to the conclusion that for the purpose of an isotropy the APWLL should be composed of discrete
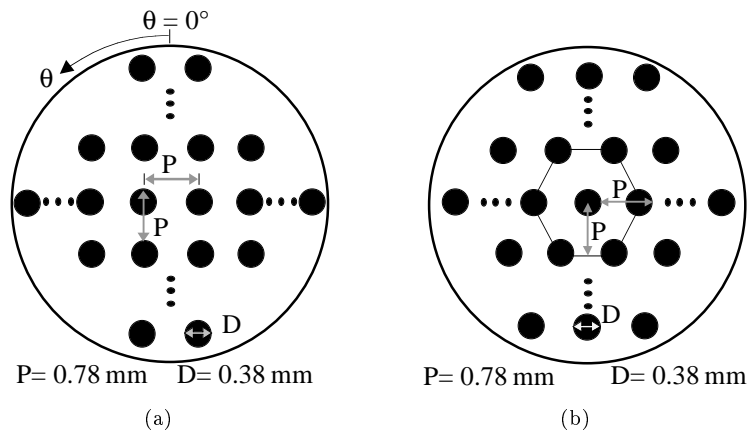
Figure 5.11: Isotropic structures with circular posts. (a) square lattice with circular posts. (b) hexagonal lattice with circular posts.

metal posts and have a two-dimensional lattice for the complete APWLL.

Now APWLLs with circular posts are investigated. In Fig. 5.11, two AP-WLLs are represented. As shown, the dimensions of the posts are identical and the diameter of two APWLLs is $5.1\lambda_0$ for the hexagonal lattice and $5.2\lambda_0$ for the square lattice. The lattices are different, so that the performance of the two lattices are evaluated.

Figure 5.12 shows the H-plane radiation patterns of the two cases. For the hexagonal lattice, two simulation of the APWLL at two scan angles of $0°$ and $6°$ are displayed while for the square lattice, the APWLL is simulated only at the scan angle $6°$. The HPBWs are $10.1°$ for the square lattice and $11°$ for the hexagonal lattice (note that the diameter of the APWLL with the hexagonal lattice is $0.1\lambda_0$ smaller than that with the square lattice). In terms of a first side lobe level, the APWLL with the hexagonal lattice is about $3\,$dB better. Therefore, the APWLL of the hexagonal lattice and circular posts is better. In addition, the reflection coefficient S_{11} for the hexagonal lattice is $-18\,$dB while for the square lattice $S_{11} = -15\,$dB.

Compared with the simulations of the APWLLs with square or hexagonal posts in Fig. 5.9, the two APWLLs have lower side lobe levels while the directivity is nearly the same. Furthermore, the HPBW is also improved. The reason is that as explained in Fig. 3.7, the projection length of the circular post is always identical, so that a circular post will support the same impedance,
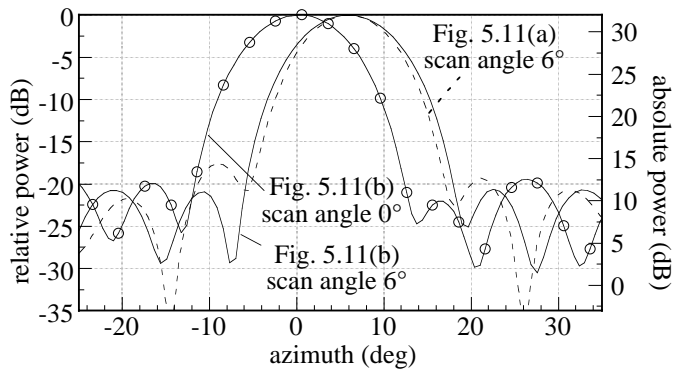
Figure 5.12: *H*-plane radiation patterns of the APWLLs composed of circular metal posts for two different lattices.

regardless of the direction of the propagating wave. As a result, it is found that the APWLL with circular posts works better and is more isotropic than that with the square and the hexagonal posts.

In Fig. 5.13, two radiation patterns in elevation (*E*-plane) are displayed for the hexagonal lattice and circular posts shown in Fig. 5.11(b). The solid line is the simulation by HFSS, the dashed-dotted line is calculated by Eq. (4.14a). Both of the patterns are in a good agreement.

Figure 5.14 shows the distribution of the electric field in the APWLL. As shown, while leaving the feed horn, a cylindrical wave propagates (see that the dotted curve near the feed is a cylindrical curve which is a equiphase line). While the wave is propagating through the lens, the cylindrical curve becomes a line (see the dotted linear line at the lens aperture) since the phase velocity around the rim is faster than that in the middle as explained in Sec. 4.1. As a result, a cylindrical wave from the *H*-plane sectoral horn is gradually transformed into a plane wave at the fictive aperture by guiding the cylindrical wave.

It is also found that compared with the simulation with a Hertzian dipole as a primary feed in [Gre99], the more power propagates through near the middle of the APWLL since the feed horn has higher gain. In the right side of the Fig. 5.14, electric field distribution near the fictive aperture is displayed. It is seen that the fields are bound by the fictive aperture.
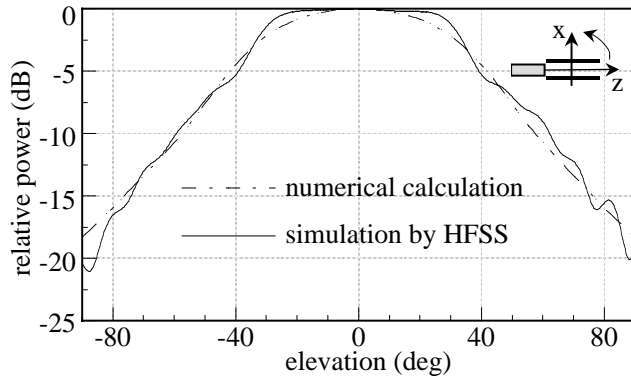
Figure 5.13: *E*-plane radiation patterns of the APWLL computed by HFSS and by Eq. (4.14a) in case of a hexagonal lattice with circular posts.
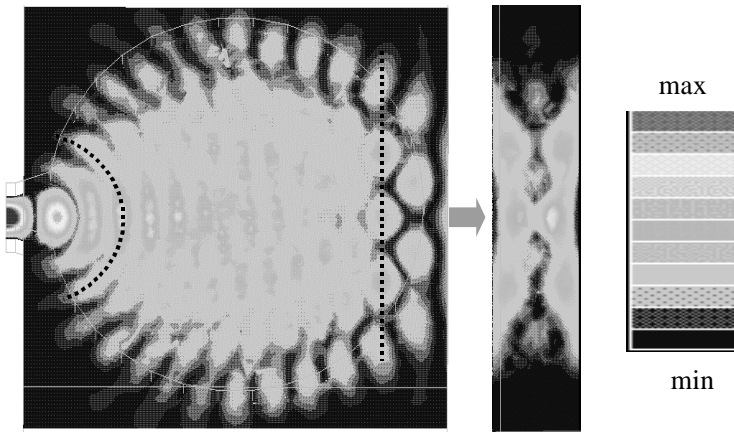

Figure 5.14: Illustration of electric field in the APWLL with the hexagonal lattice and circular posts. The dotted lines show equiphase.

5.1.3 Design of symmetric corrugated flares

5.1.3.1 Determination of dimensions of corrugated flares

In order to design a proper corrugated flare for a desired pattern, the far field of the APWLL antenna in elevation is computed at 76.5 GHz without considering the edge diffraction using Eq. (4.15). Figure 5.15 shows HPBWs as functions of the flare angle θ_e and length ρ_e. The curves are equi-HPBW lines. It is seen that each curve has an optimal range for a proper dimension of the flares to achieve a desired HPBW. For instance, consider the curve of 14.7° HPBW. As shown in the simulation, the flare angle should be chosen near at 18° for a minimal flare length for 14.7° HPBW. Also, the simulation result shows that as HPBWs are getting smaller, optimal flare lengths ρ_e increase exponentially and then the flares become larger.

From the above simulation, a beam factor ($BF_{\mathrm{sim:E}}$) for a minimal flare
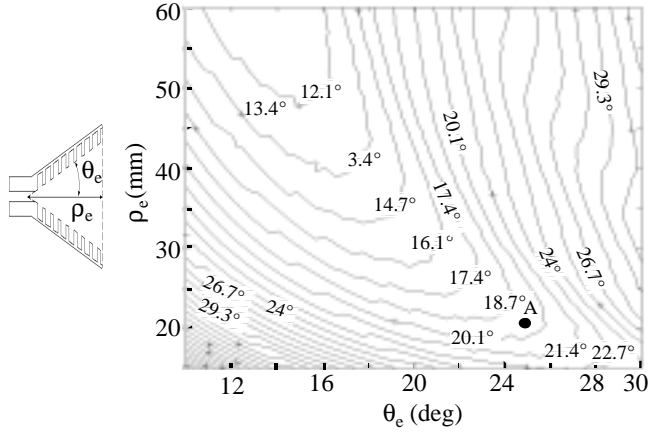
Figure 5.15: HPBWs as functions of flare angles θ_e and the flare length ρ_e.

length for a HPBW is derived

$$BF_{\mathrm{sim:E}} = \theta_{\mathrm{HPBW}} \times \frac{2\,\rho_e \tan\theta_e}{\lambda_0} \approx 93°. \tag{5.2}$$

The beam factor is used to predict approximately a required optimal dimension of corrugated flares for a desired HPBW later.

As a prototype, a pair of rotationally symmetric corrugated flares for a 20° HPBW is designed. Referring to Fig. 5.15, $\rho_e = 20.2$ mm and $\theta_e = 25°$ (see

the point A in Fig. 5.15) are determined for a 20° HPBW. The simulation is displayed in Fig. 5.16.

Figure 5.16: E-plane radiation pattern calculated by Eq. (4.15) for the determined dimensions of $\rho_e = 20.2$ mm and $\theta_e = 25°$.
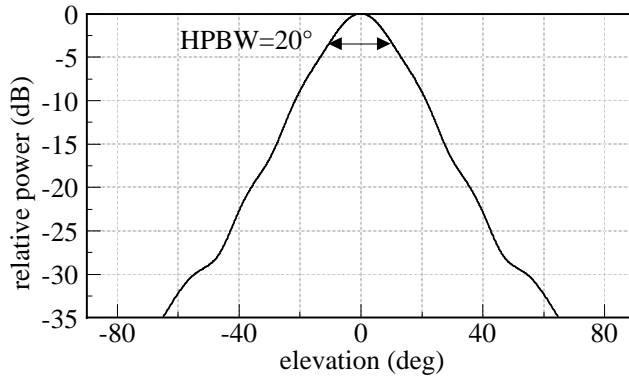
5.1.3.2 Design of corrugations

As described previously, to suppress the TM surface wave on the corrugated surface, the depth of the teeth should be between $\lambda_0/4$ and $\lambda_0/2$. Considering the mechanical stability and electronic properties such as low power loss and low reflection, a tooth thickness of 0.2 mm and a period of 0.9 mm ($0.23\lambda_0$) are selected [Men74].

Figure 5.17 shows the cross sectional view of the flare. It is divided into three parts. The first part is the cutoff ring. In this part, higher modes at the rim of the APWLL are suppressed since the spacing is lower than $\lambda_0/2$. For the flares, the cutoff ring of 2.2 mm is chosen. The second part is transition near the throat of the flares for low reflection. The depth of corrugations is decreased gradually from about $\lambda_0/2$ to $\lambda_0/4$. Since corrugations with a depth of about $\lambda_0/2$ act like a conducting surface, in this transition part, the reflection at the transition is reduced [Olv92]. The third part is the high impedance region between the end of the transition and the end of the flare. The corrugations are about $\lambda_0/4$ deep. In this part, the TM surface wave is strongly prohibited. Referring to [Men74], no less than 8 corrugations which are $\lambda_0/4$ deep are necessary for both a cosine amplitude and proper phase distribution at the aperture of the flares. In Fig. 5.17, the cross sectional view of lower part

of the flares for a 20° HPBW is presented.

It should be mentioned that the simulation results and the novel approach
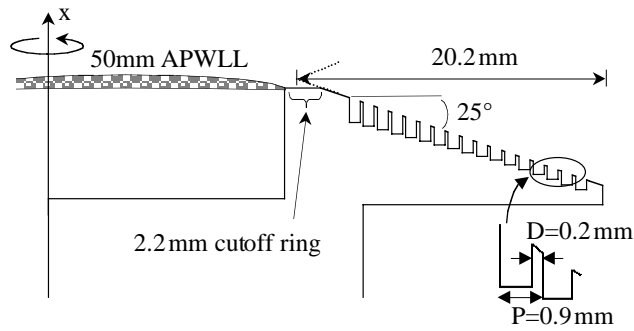

Figure 5.17: Cross-sectional view of the rotationally symmetric corrugated flare for the 50 mm APWLL.

for designing the rotationally symmetric corrugated flares are unique to determine the proper flare dimensions for a desired HPBW and first side lobe.

5.2   Fabrication

5.2.1   APWLL

To verify the simulation results of the previous section, two APWLLs are fabricated. One is a 50 mm APWLL with a square lattice and square metal posts. The other is a 50 mm APWLL with a hexagonal lattice and circular posts.

5.2.1.1   50 mm APWLL with a square lattice and square posts

The APWLL is composed of two aluminum plates. One plate is a plane aluminum plate, and the other is provided with the PBG structure on the surface. As determined in Sec. 5.1.2, the width of square posts D is 0.28 mm and the period P=0.78 mm. The spacing h of the parallel-plate waveguide is 1.9 mm. The lattice is a square. The APWLL's diameter is 50 mm.

The fabrication procedure of the plate with the PBG structure is divided into three steps. First, a metal surface curvature calculated by Eq. (4.2) for the metal post height is fabricated on a computer numeric control (CNC) revolving

machine. The machine has the tolerance of $1\,\mu$m. Second, a CNC milling machine produces the posts by machining the curve. In the end, it is etched by an acid to get away the metal wastes between the posts and around the posts. The PBG structure consists of about 3000 square posts.

In Fig. 5.18, a picture of a small part of the APWLL is presented to show

(a)

0.78 mm

(b)
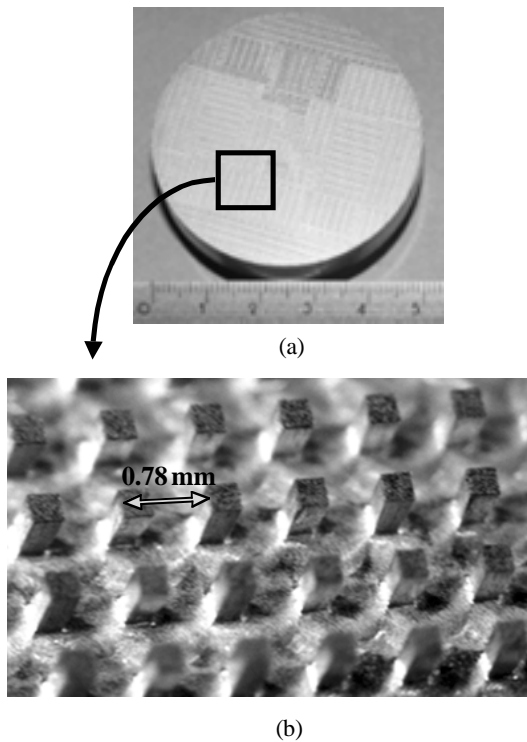
Figure 5.18: (a) Photograph of one part of the APWLL where the PBG structure is implemented. Diameter is 50 mm. (b) Photograph of the PBG structure in the APWLL. The lattice is a square and the metal posts are a square.

the posts. As illustrated in Fig. 5.18, the square posts are arranged periodically and regularly. The fabrication error of the post width is also measured, they are within $\pm 20\,\mu$m.

In contrast, the plain aluminum plate for the other plate is produced by the CNC revolving machine with a diamond cutter. The plate looks like a plane metal mirror.

5.2.1.2   50 mm APWLL with a hexagonal lattice and circular posts

From the simulations in the previous section, it is shown that the APWLL with a hexagonal lattice and circular posts shows the best performance. For verification, the 50 mm APWLL with circular posts and a hexagonal lattice is fabricated. Also it is compared with the 50 mm APWLL with square posts and a square lattice.

For fabrication, the milling cutter of 0.5 mm diameter is used due to its durability. The diameter of the posts D is determined to 0.28 mm while $P = 0.78$ mm.

Figure 5.19: Photograph of the PBG structure in the 50 mm APWLL with a hexagonal lattice and circular posts.

5.2.2   H-plane sectoral horn for a primary feed

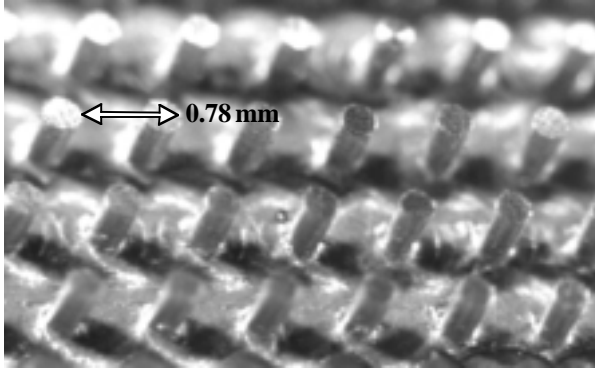The procedure of fabrication is the same as that of the 50 mm APWLL with square posts and a square lattice. In Fig. 5.19, a picture of a part of the APWLL is presented. The H-plane sectoral horn with an aperture 3.6 mm × 1.27 mm is made of a WR-10 waveguide (inside dimension = 2.54 mm × 1.27 mm, outside dimension = 4.58 mm × 3.3 mm including the copper thickness).

As shown in Fig. 5.17, the flares have a cutoff ring between the rim of the APWLLs and the throat of the flares. Therefore, when the feed horn excites the complete APWLL with the flares, the feed has to be fit to the parallel-plate spacing h=1.9 mm. In Fig. 5.20, the feed horn whose outside copper thickness is thinner is displayed. In measurement, the aperture of the horn is placed in the middle of the parallel-plate waveguide.
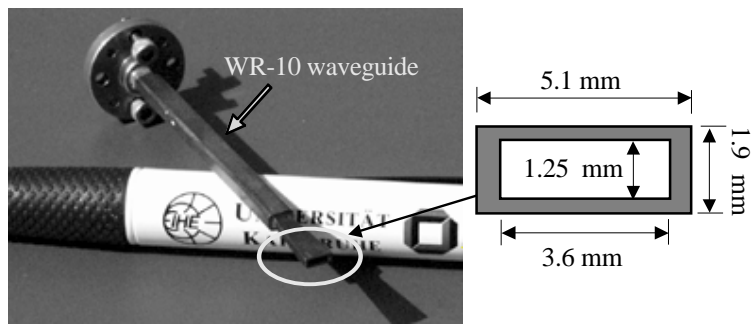
Figure 5.20: Photograph of the *H*-plane sectoral horn.

5.2.3 Rotationally symmetric corrugated flares

The fabrication of the flares is divided into two steps. First, the CNC revolving machine fabricates the plane flares which look like a biconical antenna, and then the circular corrugations are engraved on the flares.

In Fig. 5.21, one part of the flares for a HPBW of 20° is presented. The
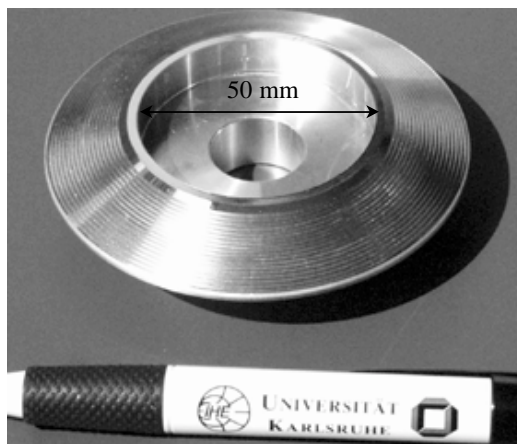
Figure 5.21: Photograph of the flare for a HPBW of 20°.

flares are composed of 17 corrugations, including the transition part and the high impedance part. A 2.2 mm cutoff ring is also machined. To remove a

small amount of edge effect on the top edge, the top edge of the flares becomes round.

5.3   Measurements

In Fig. 5.22(a), the experimental setup is displayed. As seen, the entire antenna is composed of an APWLL, a pair of rotationally symmetric corrugated flares, and the feed horn. In Fig. 5.22(b), the detailed AWPLL antenna and
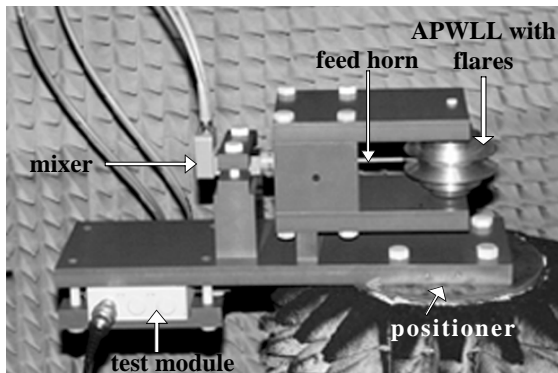
(a)
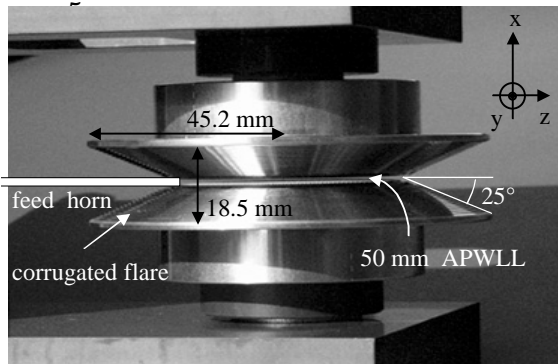
(b)

Figure 5.22: (a) Experimental setup. (b) Entire 50 mm APWLL with the flares and its geometrical dimension.

its geometrical dimension are displayed. A horn antenna as a receiver antenna

which has 25.0 dBi gain is used. The distance between the APWLL antenna and the receiver is about 3 m.

5.3.1 H-plane sectoral horn

First, the far-field patterns of the feed horn shown in Fig. 5.20 are measured. In Fig. 5.23, the simulation and the measurement of the H-plane patterns are plotted. The simulation of the pattern is performed using the formulas for the far-field pattern of the horn in [Bal97]. The simulated pattern is broader than the measured one. As explained in Fig. 5.2, it is expected in the next measurement that the fact has an effect on larger HPBWs and lower first side lobe. E-plane pattern of the feed horn is also displayed in Fig. 5.23.

Figure 5.23: H-and E-plane radiation patterns of the feed horn.

5.3.2 Fraunhofer region

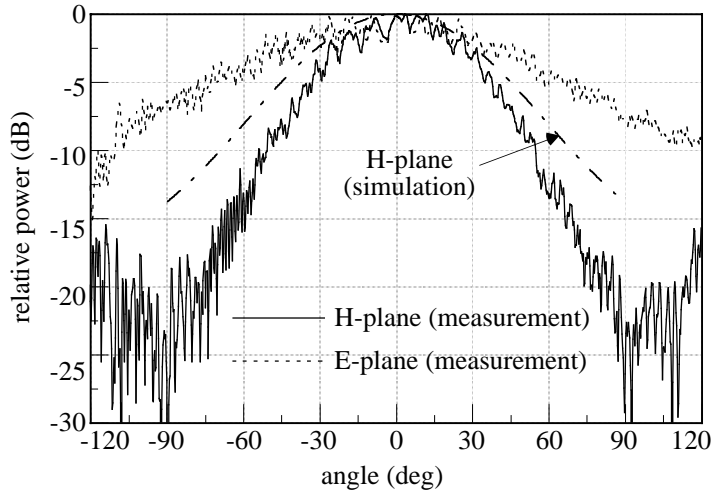For the appropriate measurement of a large antenna, it is important to find in advance the far-field or Fraunhofer region (R_F) where the field at the antenna under test approximates a uniform plane wave. As is well known, the following relation is required for the maximum phase error smaller than $\lambda_0/16$ which is

commonly acceptable for the far field [Kra88], [Bal97], [Wie99]. That is,

$$R_{\mathrm{F}} = \frac{2D_{\mathrm{E}}^2}{\lambda_0} \qquad (5.3)$$

where D_{E} is a maximum overall dimension, for example the largest diameter, the largest diagonal length and so on.

For the fictive aperture of the 50 mm APWLL with the flares, 90.4 mm by 18.5 mm (see Figs. 5.22(b)), the maximum overall dimension D_{E} is the diagonal length of 92.2 mm, so that the distance for the far-field measurement $R_{\mathrm{F}} > 4.3$ m is obtained by Eq. (5.3). However, as the phase distribution of the APWLL at the fictive aperture is constant in azimuth, only the maximum phase error in elevation for the far field is to be considered. That results in $D_{\mathrm{E}} = 18.5$ mm and $R_{\mathrm{F}} > 0.18$ m. Therefore, the 3 m distance is large enough to measure the far-field pattern of the APWLL antenna.

5.3.3 50 mm APWLL with a square lattice and square posts

Figure 5.24 illustrates measured H-plane radiation patterns for three different scan angles $0°$, $10°$, and $20°$ without the flares. In order to measure the APWLL at beam scan angles $10°$ and $20°$, the AWPLL is simply rotated with the feed horn fixed like the same way. The HPBW of the antenna is $5.2°$. The first side lobe is -17 dB. With the result, the beam factor $(BF_{\mathrm{mea:H}})$ is derived for an approximate prediction of other APWLLs.

$$BF_{\mathrm{mea:H}} = \theta_{\mathrm{HPBW}} \times \frac{2 \times r_0}{\lambda_0} = 66°. \qquad (5.4)$$

The results verify that the APWLL antenna has a wide scan angle in azimuth and the PBG structure is nearly isotropic.

Figure 5.24 also shows the simulation (dashed-dotted line) calculated by Eq. (4.13b). Compared with the simulation result, the measurements have a minimal increase of the HPBW as expected from the results in Fig. 5.23. However, in contrast to the prediction, the first side lobe becomes worse. The reason is that edge diffraction by the front square posts where the waves leave the AP-WLL disturbs wave propagation and the APWLL is not fabricated ideally. The cross-polarization in case of a scan angle $0°$ is measured. It is lower than -25 dB.

In Fig. 5.25, the simulated and measured E-plane radiation patterns of the APWLL without the flares are illustrated. The patterns are normalized. The solid line is the simulation result of the $5.1\lambda_0$ APWLL in Fig. 5.8(a) by
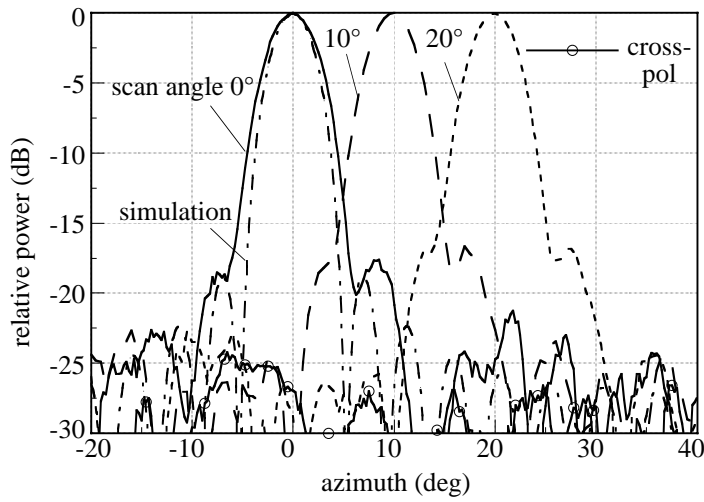
Figure 5.24: *H*-plane radiation patterns for three different scan angles without the corrugated flares and simulation result. Cross-polarization for a scan angle of 0°.

HFSS. The dashed line is the measurement result. Both results are in good agreement, regardless of the radius of the APWLL.

The antenna is also measured by adding the symmetric corrugated flares to the APWLL (see Fig. 5.22(b)). The measurements in Fig. 5.26 show that the antenna has also a wide scan angle in azimuth like the APWLL antenna without the flares. The HPBW is 4.8° and the first side lobe is -20 dB. Compared with the antenna without the flares, the antenna with the flares has an about 0.4° narrower HPBW and -2.5 dB lower first side lobe. The reason is that the symmetric corrugated flares remove the edge diffraction in both elevation and azimuth.

In Fig. 5.27, the simulated and measured *E*-plane radiation patterns are illustrated. Side lobe levels point out lower than -27 dB due to the corrugated flares. The HPBW is 19.5°. In terms of the HPBW, both the measurement and the calculation are in good agreement. Since the aperture becomes larger and the HPBW becomes narrower by adding the flares, the directivity of the complete antenna is about 6.5 dB higher than that of the APWLL without the flares.

The reflection coefficient (S_{11}) of the APWLL antenna is also measured. S_{11}
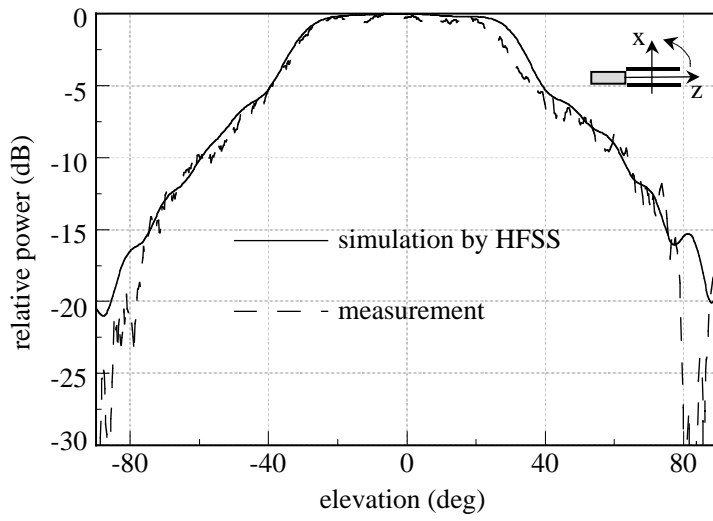
Figure 5.25: Simulated and measured E-plane radiation patterns without the corrugated flares.

of only the APWLL with the flares amounts to -13 dB whereas the complete APWLL antenna with the flares has S_{11}=-14 dB due to the corrugated flares.

The gain of the antenna is measured by comparing the maximum value with that of the reference horn. The gains of the complete antenna and the APWLL only are 24 dBi and 17.5 dBi, respectively. Using the general formula for approximating gain in [Sch51], [Tai76], and [Stu98], the approximate gain can be predicted from the measured HPBW of the patterns in H-and E-plane. The formula is

$$G \approx 10 \log(\frac{26000}{HPBW_{H^\circ} \cdot HPBW_{E^\circ}}). \tag{5.5}$$

In the case of the APWLL itself without the flares, $HPBW_{H^\circ} = 5.2°$ and $HPBW_{E^\circ} = 62.3°$. Eq. (5.5) leads to an approximate gain of 19.06 dBi. Also in the same way, the gain for the complete antenna is 24.41 dBi. Considering the aperture efficiency, the measured gain is consistent with the calculation.

Finally, the complete antenna with the corrugated flares is measured using a H-plane sectoral horn of a =5.3 mm. In Fig. 5.28, measured H-plane radiation pattern is plotted. The marked-dotted line is the result calculated by Eq. (4.13b). The dashed line is the measurement of the APWLL using the

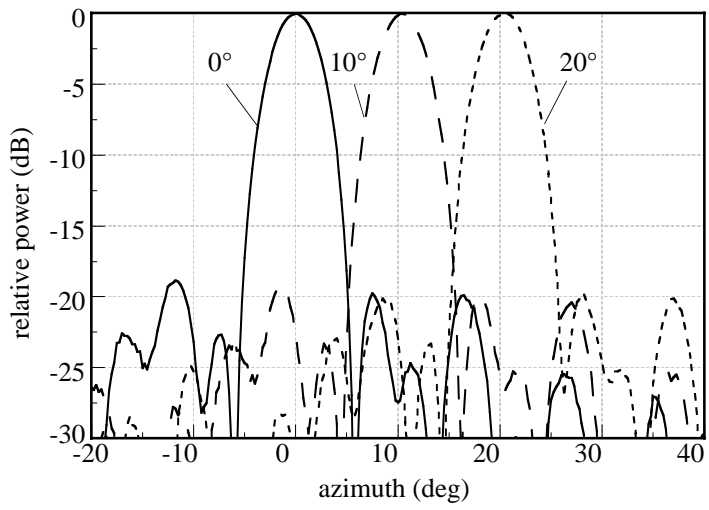Figure 5.26: Measured H-plane radiation patterns for three different scan angles with the corrugated flares (see Fig. 5.22).
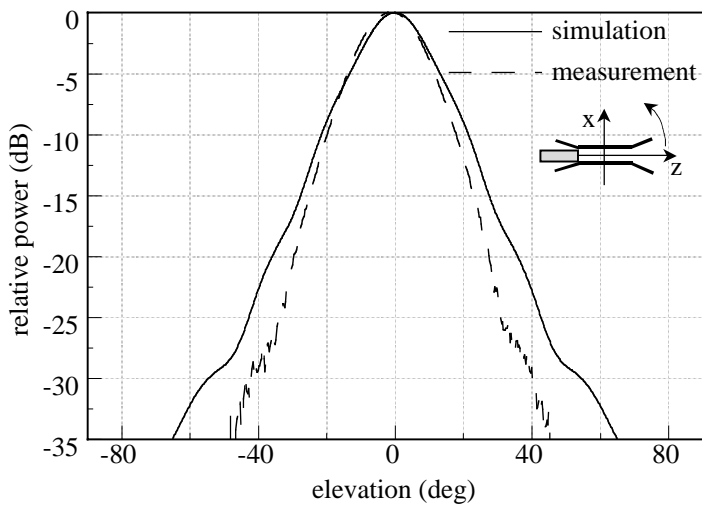
Figure 5.27: Simulated and measured E-plane radiation pattern of the APWLL with the corrugated flares.
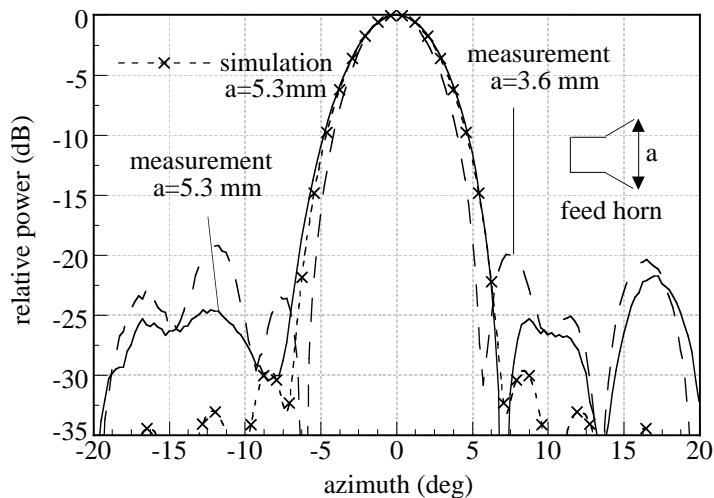
Figure 5.28: The influence of the feed dimension a on the patterns (see Fig. 5.1). The patterns are normalized.

feed horn a =3.6 mm. In terms of HPBW, both the simulation and the measurement are in a good agreement. Compared with the measured pattern using the feed horn a =3.6 mm, the HPBW becomes higher while side lobe levels are lower. In other words, Fig. 5.28 verifies well the simulation results in Figs. 5.1 and 5.2 that the HPBW of the APWLL becomes higher and the first side lobe is getting lower as the aperture width of a feed horn is getting larger.

5.3.4 50 mm APWLL with a hexagonal lattice and circular posts

For the measurement of the 50 mm APWLL with a hexagonal lattice and circular posts, the setup for the 50 mm APWLL with a square lattice and square posts is used in Fig. 5.22.

In Fig. 5.29, the measured and simulated H-plane radiation patterns of the APWLL without the flares are plotted. The simulation is done using the result of Eq. (4.13b). The APWLL is measured at three different scan angles to verify the isotropy of the circular metal post structure and the multiple beam property of the APWLL designed by circular metal post structure. The patterns point out a 4.9° HPBW and the first side lobe level is lower than -19 dB. Compared

with the above 50 mm APWLL with the square lattice and square posts, the APWLL with a hexagonal lattice and circular posts works better in terms of HPBW and the first side lobe. The gain of 23.8 dBi is measured. As a result, the measurement verifies the simulation result in Sec. 5.1.2 and the theory in Sec. 3.2.1 that the combination of hexagonal lattice and circular posts is better than that of a square lattice and square posts.

Figure 5.29: *H*-plane patterns of the APWLL with a hexagonal lattice and circular posts without the flares for three beam scan angles.

It is interesting to show how good the APWLL with the combination of a hexagonal lattice and circular posts is, compared with the Luneburg lens made of a real homogeneous isotropic dielectric. In [Par01], a parallel-plate Luneburg lens (PPLL) similar to the APWLL is reported. The appearance of the PPLL is similar to that in Fig. 4.1(c). Since two antennas, PPLL and APWLL are quite similar, related to the properties and main principles, the measurement of APWLL is compared with that of the parallel-plate Luneburg lens (PPLL) using a homogeneous dielectric, paraffin wax in [Par01] in order to estimate the performance of the metal post structure for an artificial dielectric. In Fig. 5.30, comparing two measured *H*-plane patterns is displayed. In terms of gain, the gain of the PPLL is about 0.7 dBi higher than that of the PPLL. However, as shown in Fig. 5.30, two measured patterns are in good agreement. Thus, it can be said that the circular metal post structure as an artificial dielectric works

as well as a real dielectric.
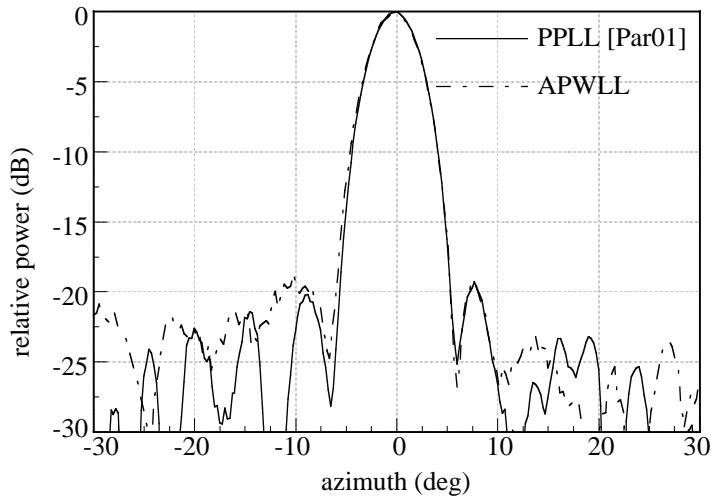
Figure 5.30: Comparison of two measured patterns between the APWLL with circular posts and the asymmetric parallel-plate Luneburg lens using a homogeneous dielectric in [Par01].

In order to check a bandwith of the APWLL, measurements are performed at several different frequencies. Figure 5.31 shows four H-plane radiation patterns at 76 GHz, 76.5 GHz, 77 GHz, and 77.5 GHz. The patterns are normalized despite the minimal difference of the gain. As is shown, the patterns differ little in terms of side lobe level and HPBW. It means that the APWLL has more than 1.5 GHz bandwidth.

The APWLL antenna with the flares for 20° HPBW is also measured. As shown in Fig. 5.32, the flares have little influence on the APWLL's property of a wide scan angle. But the side lobe levels become lower than those with the flares while the HPBW becomes 0.2° higher.

Figure 5.33 shows E-plane radiation patterns. The dashed line is co-polarization of the APWLL without the flares and the solid line is co-polarization of the complete antenna with the flares. The complete antenna with the flare has 19.9° HPBW. Also, the very low side lobe levels are due to the flares as explained previously. It shows that the gain of the complete antenna is 7 dB higher than that of the APWLL without the flares. The cross-polarization is lower than -30 dB.
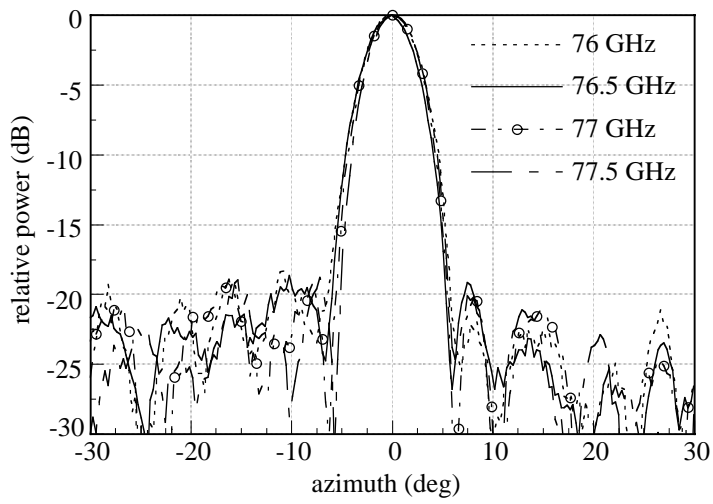
Figure 5.31: *H*-plane patterns of the APWLL with a hexagonal lattice and circular posts without the flares in case of three different operating frequencies.
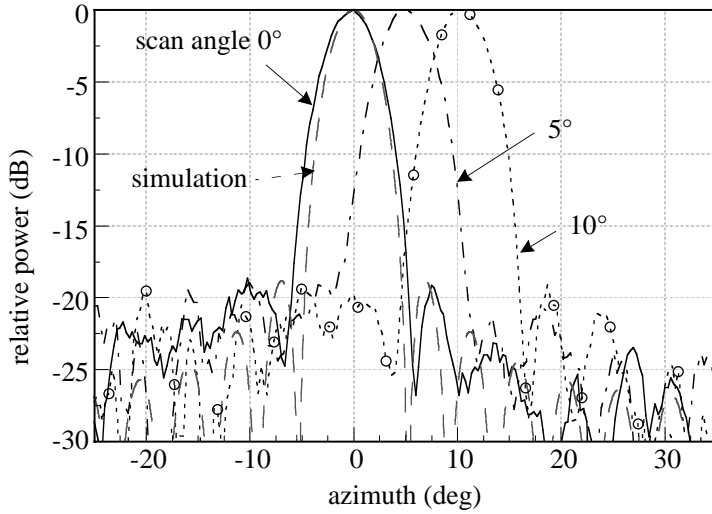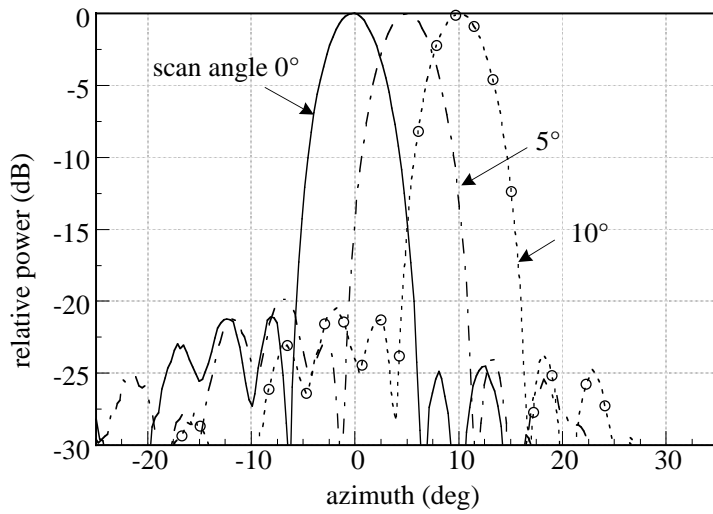

Figure 5.32: *H*-plane patterns of the APWLL with a hexagonal lattice and circular posts with the flares for three beam scan angles.
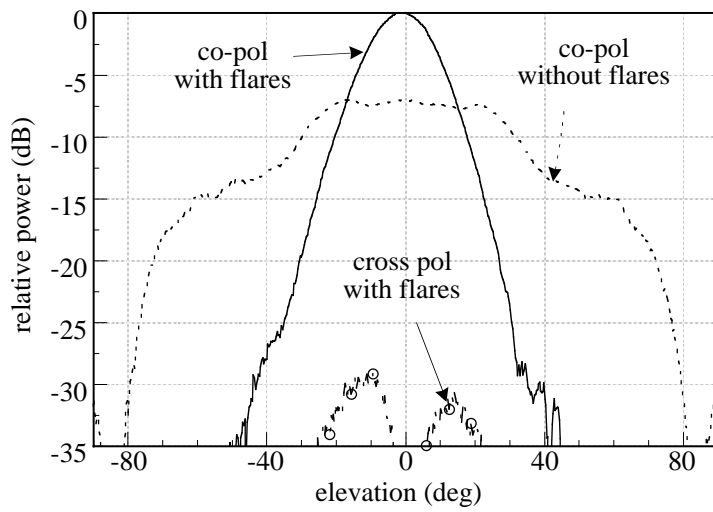
Figure 5.33: *E*-plane patterns of the APWLL with a hexagonal lattice and circular posts without and with the flares. Cross-polarization with the flares.

In Secs. 1.2.1 and 4.1, it is mentioned that the phase distribution of the APWLL in azimuth is constant since a plane wave leaves the APWLL. Also, as shown in the simulation in Fig. 5.14, the phase of the electric field becomes constant at the fictive aperture. Figure 5.34 shows the measurement of the phase distribution of the entire antenna with the flares. It is seen that in the main lobe, the phase is nearly constant.

For a lens antenna, the exact focal point is directly related to the performance of the lens antenna. The influence of the focal point is illustrated in Fig. 5.35. As shown, for a distance d =2 mm, the first side lobe increase by about 5 dB, while the HPBW is little varied. It means that if the horn is moved in radial direction by the distance d, it has a direct influence on the side lobe levels because the lens is defocused and the phase errors in the aperture increase.

5.4   Virtual-source APWLL

In this section, the new challenge to reduce the size of the APWLL itself is investigated. The main idea is based on the concept of the virtual-source
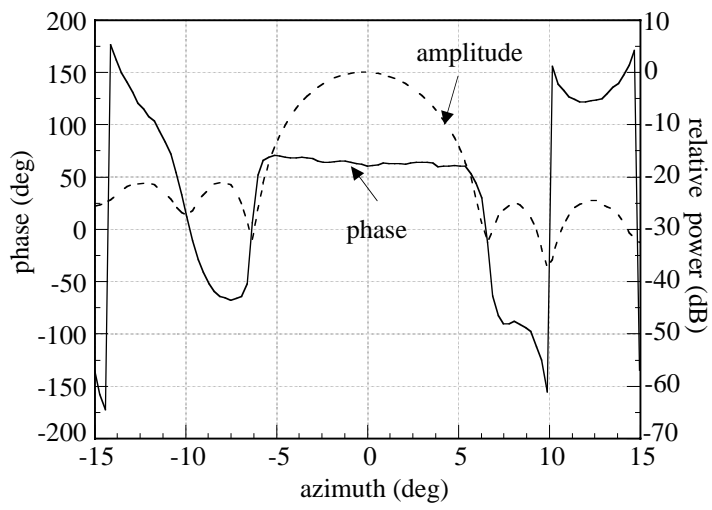
Figure 5.34: Phase information with simultaneously the amplitude for the scan angel $0°$ in case of the APWLL without the flares.
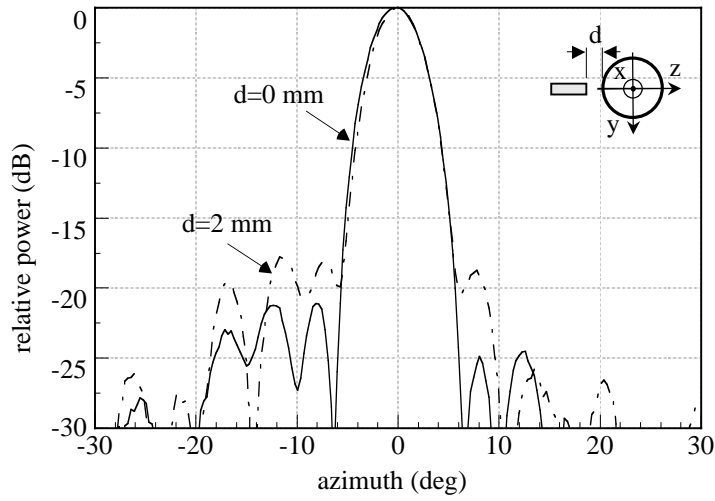
Figure 5.35: Influence of the feed position error on the radiation patterns of the AP-WLL with a hexagonal lattice and circular posts.

Luneburg lens. It will be shown that using the concept, the APWLL size may be reduced to the half.

5.4.1 Principle of a virtual-source APWLL

The basic concept of a virtual-source APWLL is based on the image theory. In Fig. 5.36, the ray path of the APWLL is shown. As shown in the figure, an equivalent PEC or PMC reflector is added through the center of the lens, and then from the image theory, each real source has a virtual source on the other side of the reflector [Pee53b], [Pee54], [Joh84]. Therefore, the virtual-source lens reduces to the half of the size of the complete lens.

In spherical Luneburg lenses, the concept of a virtual-source has been real-
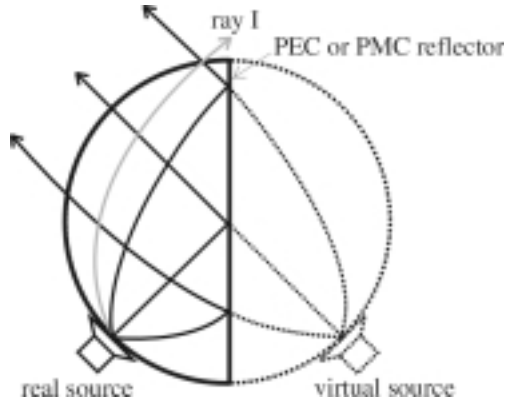
Figure 5.36: Illustration of the virtual source Luneburg lens. The ray paths are displayed in the lens.

ized to cut down the volume of the lenses [Sch95], [Par00b], [Smi89]. However, until now there has not been a virtual source Luneburg lens for PPLLs.

5.4.2 Simulation

In Fig. 5.37, the entire virtual-source APWLL for simulation is displayed. It is seen that the APWLL has a hexagonal lattice and circular posts. The diameter of the APWLL is $5.3\lambda_0$. The period and the diameter of the posts are 0.78 mm and 0.36 mm, respectively. It should be pointed out that in the simulation, the feed horn is turned around to scan the beams with the entire posts fixed. The simulation is performed at 76.5 GHz.
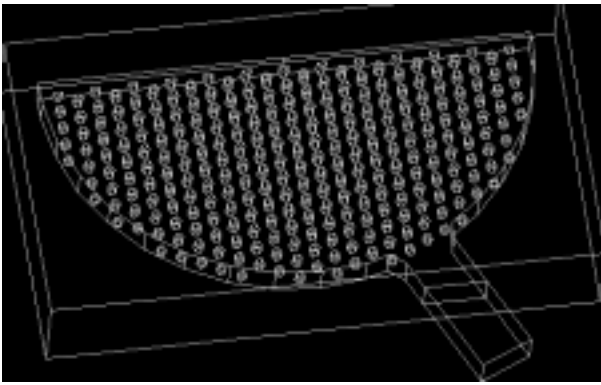
Figure 5.37: Illustration of the virtual-source APWLL for the simulation by HFSS.

Table 5.2: Summary of the simulation results of the virtual-source APWLL for three different scan angles.

	maximum (dB)	S_{11} (dB)	HPBW (°)
scan angle 40°	29.1 dB	-18 dB	12.5°
scan angle 55°	29.7 dB	-14 dB	12.2°
scan angle 65°	30.0 dB	-14 dB	11.7°
full lens	32.1 dB	-18 dB	10.5°

The simulation results for the scan angles 40°, 55°, and 65° are plotted in Fig. 5.38. In Tab. 5.2, the results are summarized. Compared to the result of the full lens in Sec 5.1, the virtual-source lens has about 2.5 dB lower directivity and about 1.5 dB larger HPBW. The reason can be understood by means of Fig. 5.36. That is, the fictive aperture becomes smaller since some rays such as the ray I (gray solid line) in the figure cannot be reflected toward the destination. It also shows that side lobe levels become higher than that of the full APWLL. The reason is due to edge diffraction and spillover problem by the rays such as the ray I.

Additionally, the electric field distribution in the APWLL for the scan angle 65° is illustrated in Fig. 5.39. It can be seen that the field distribution is different from that of the full APWLL in Fig. 5.14. The equiphase lines are not shown clearly at the fictive aperture. It is also noted that the virtual-source
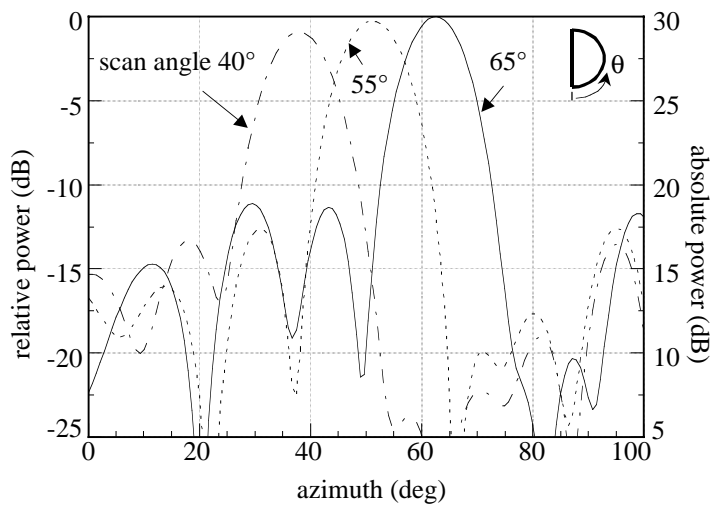
Figure 5.38: Radiation patterns of the virtual-source APWLL depending on three different scan angles.
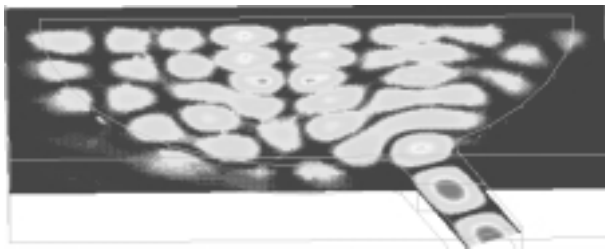
Figure 5.39: Illustration of the electric field distribution in the APWLL for the scan angle 65°.

APWLL has relatively strong fields at the edge of the reflector, which may cause higher side lobe levels.

As a result, practically, the virtual-source APWLL does not function exactly like the full APWLL. The main problem is due to the rays which do not reflect on the reflector. Therefore, for the purpose of the virtual-source APWLL, the length of the reflector in the middle should be longer than the diameter of the APWLL. Thus, the larger reflector is able to reflect the rest of the rays toward the desired direction.

5.5 Limitations of corrugated flares for ACC radar application

As mentioned in [Sch98] and [Wie01], an antenna for an ACC radar at 76.5 GHz should support a medium-high resolution in elevation. In general, a HPBW of the antenna should be narrower than 8° HPBW.

Consider the APWLL antenna. The simulation in Fig. 5.15 shows that for 8° HPBW, the flare length ρ is larger than 100 mm. By considering an APWLL of 50 mm diameter, the total length of the entire antenna amounts to 250 mm.

Certainly, in order to mount the ACC radar system including the APWLL antenna inside a car's front grille, it is necessary that the entire antenna should be as compact as possible. A typical automotive radar is roughly the size of two stacked paperback books - just 140 mm by 70 mm by 100 mm [Jon01]. Therefore, although the virtual-source APWLL is helpful for a compact antenna, the entire antenna is still too voluminous for a 76.5 GHz ACC radar system due to the excessive corrugated flares. At the same time, since many corrugations are machined on the great flare, additional losses in the metal is caused by the corrugations and hence antenna gain lowers [Kra88].

In the next chapter, a couple of new approaches are proposed to overcome the above drawbacks.

Chapter 6

Improvement and optimization of APWLL antenna for ACC radar application using offset reflectors

In this chapter, a new idea of using an offset reflector for the APWLL antenna is presented to resolve the shortcomings of large flares as described in Sec. 5.5. It will be shown that with the aid of the offset reflector, a medium-high resolution is achieved, simultaneously keeping the entire antenna compact. Moreover, a higher gain is obtained since the metal losses by the offset reflector are low and the offset reflector focuses rays of a feed in a desired direction.

Here two offset reflectors are considered. First, an offset planar reflector is investigated empirically. Through the measurements of the offset planar reflector, useful results for better understanding of the behavior of the APWLL antenna with an offset reflector are obtained. Second, an offset cylindrical parabolic reflector is considered. Using GO, the far field of the offset cylindrical parabolic reflector is obtained. By usage of the far-field calculation, the offset cylindrical parabolic reflector is optimized for a desired HPBW and a compact reflector.

6.1 Offset planar reflector

In Fig. 6.1, the offset planar reflector system is illustrated. It is composed of an aluminum planar reflector, a pair of symmetric corrugated flares, and the 50 mm APWLL. The 50 mm APWLL with a square lattice and square metal posts in Fig. 5.18 is used. The feed horn of 3.6 mm × 1.29 mm in Fig. 5.20 is used. The symmetric corrugated flares for a 20° HPBW in Fig. 5.21 are equipped to the 50 mm APWLL in measurement. The reflector is the size of 100 mm by 150 mm, taking the dimension of the corrugated flares into consideration. The reflector has a 45° tilt angle and hence the rays of the flares are simply reflected by the planar reflector without focusing rays. By varying the distance d_1, the effective aperture on the reflector can be enlarged or diminished. The entire reflector antenna is measured at 76.5 GHz ($\lambda_0 = 3.92$ mm).

Figure 6.2(a) shows the measured radiation pattern (solid line) of the APWLL antenna with the reflector in azimuth (H-plane). The dashed line is the measurement without the reflector in Ch. 5. The distance d_1 is $2\lambda_0$. It has 4.4° HPBW. The first side lobe level is -20 dB. Compared with the pattern of the APWLL antenna itself, the HPBW becomes about 0.4° narrower and the gain is increased by 1.5 dB. A first side lobe level is little changed. The reason of the improvement of gain and HPBW is that the effective aperture on the reflector becomes larger.

Figure 6.2(b) shows the measurement of beam scanning for three different scan angles. The side lobe levels of the patterns keep nearly constant while the gain is somewhat lower for a larger scan angle.

Figure 6.3 shows the measurements in elevation (E-plane). The measurements are conducted for $d_1 = \lambda_0$ (dotted line) and $d_1 = 2\lambda_0$ (solid line), respectively. Both have a HPBW of about 16.5°. The dashed-dotted line is the measurement without the reflector in Ch. 5. The HPBW becomes 3° narrower than that without the reflector. In the patterns, the edge scattering is found at the angle of around -40°. It is seen that as increasing the distance d_1, the angle of the edge scattering is moved to the left and the edge scattering has little influence on the main lobe.

The above results of the planar reflector conclude that using the planar reflector, the HPBWs of the antenna are somewhat improved in elevation and in azimuth as well, and at the same time the gain of the antenna is enhanced while the side lobe level of the antenna is little varied. Especially, the planar reflector has more influence on the HPBW of the pattern in elevation than that in azimuth. However, for a much narrower HPBW in elevation, the distance d_1 should be larger since a large effective aperture is required. This large distance
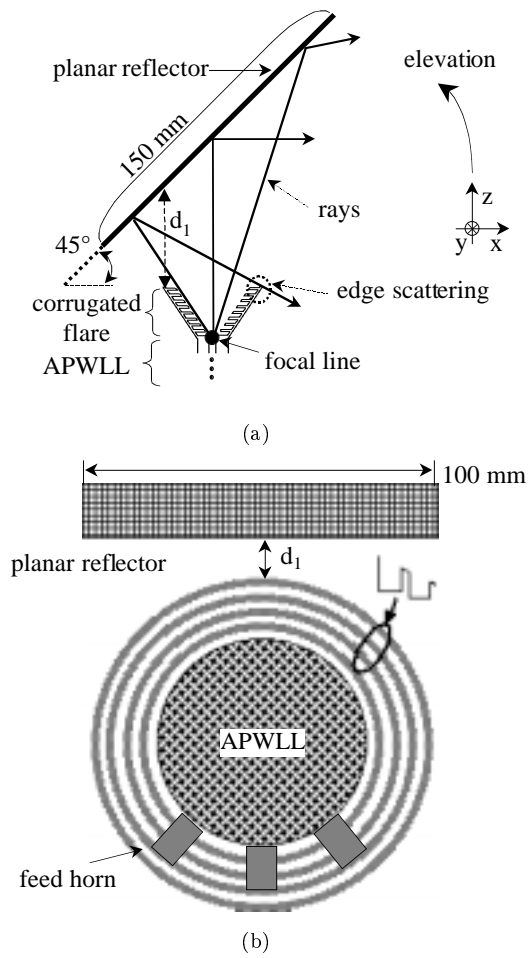
Figure 6.1: Geometry of the entire planar reflector system and coordinate system.
(a) Side view. (b) Front view.

needs a large planar reflector to reflect almost all radiation of the feed. Also it is likely to cause a critical phase error at the aperture of the reflector. The reason of this problem is due to the original drawback of the planar reflector that the planar reflector changes simply the propagation of the rays from the feed in elevation [Ehr75], [Joh93]. From the above reasons, an offset parabolic reflector
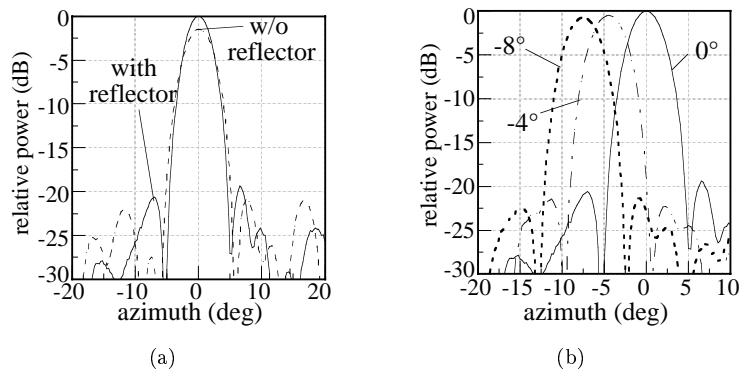
Figure 6.2: Influence of the planar reflector on H-plane radiation patterns. (a) Comparison of the results with the reflector (solid line) and without (w/o) the reflector (dashed line). (b) Beam scanning measurement.
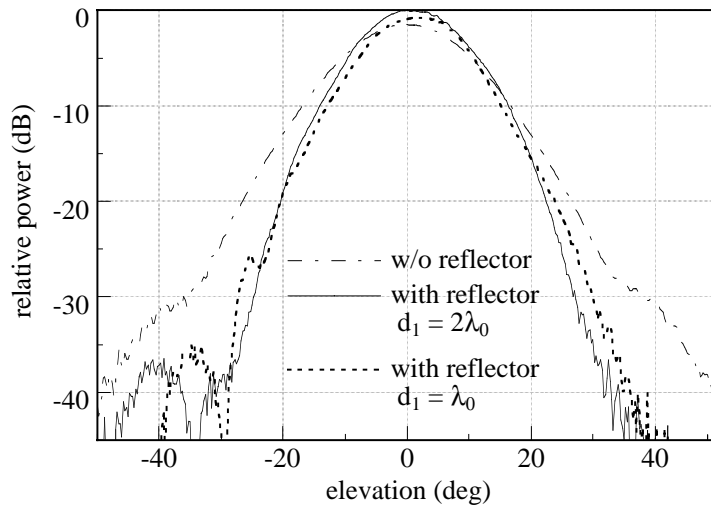
Figure 6.3: Influence of the planar reflector on E-plane radiation patterns.

is needed to collimate the rays from the feed and avoid the edge scattering by the corrugated flares.

6.2 Offset cylindrical parabolic reflector with corrugated flares

In this section, an offset cylindrical parabolic reflector antenna is considered in order to solve the problems of the APWLL antenna. GO is used to calculate far fields of the reflector in elevation. Using the far-field calculation, optimal dimensions of the reflector and the corrugated flares are determined for a desired HPBW and first side lobe level. Also, depending on a desired maximum scan angle, the unnecessary part of the flares is removed. The design procedures are described in the following sections in detail.

6.2.1 Principles of an offset reflector

As described previously, an offset reflector of collimating the rays of the APWLL antenna and modifying their phase is necessary for the dimension reduction of the entire reflector antenna. For the above purposes, a classical offset dual reflector [Han61], [Joh62], [Sco90] can be used. However, a single offset cylindrical parabolic reflector is more appropriate for the ACC radar due to its stability in tough environments and its simplicity in terms of design and fabrication.

An offset cylindrical parabolic reflector is often applied to produce pencil beams by collimating rays from a feed [Sil49], [Lov78], [Kil00]. As shown in Fig. 6.4, the entire reflector system consists of a line source, called a focal line and a cylindrical parabolic reflector. It is assumed that the line source radiates a cylindrical wave. From the property of parabola geometry, the length of the propagating rays which are reflected by the reflector is same at the aperture, so that the phase of the wave becomes identical at the reflector aperture. Therefore, the cylindrical wave from the line source is transformed to a plane wave at the reflector aperture by the reflector. Also, since the line source is fed below the offset reflector, the reflector avoids the scattering of main rays with the line source, which is a useful advantage of the offset feed technique [Sil49], [Kra88].

We consider the APWLL antenna in Ch. 5. In azimuth, the complete APWLL extended to the corrugated flares produces a plane wave at the fictive lens aperture. In elevation, the corrugated flares result in a cosine field distribution in terms of phase and amplitude. In other words, the APWLL antenna generates a cylindrical wave which can be replaced by a virtual equivalent line source. Thus, as mentioned above, this cylindrical wave is converted into a plane wave by an offset cylindrical parabolic reflector.

cylindrical parabolic reflector

z

y

x

line source

(a)

rays
collimating

z

x

focal line   y

(b)
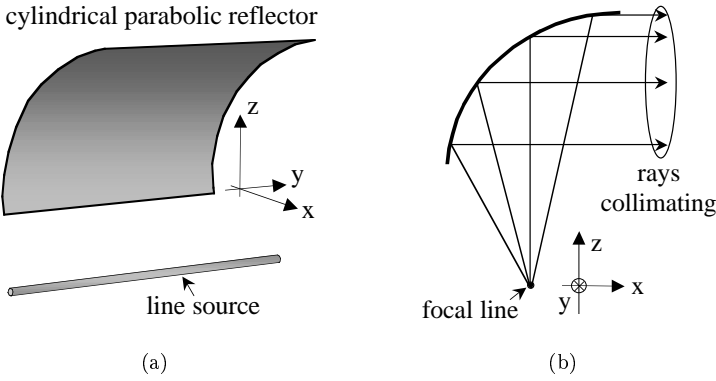
Figure 6.4: Geometry of an offset cylindrical parabolic reflector. (a) Entire reflector
system and coordinate system. (b) Side view.

In Fig. 6.5, the entire offset cylindrical parabolic reflector system is illus-
trated. It is composed of the APWLL, a pair of symmetric corrugated flares,
and a cylindrical parabolic reflector. The corrugation can be linear or circular
as illustrated in Figs. 6.5(b) and 6.5(c). Especially, in case of the circular cor-
rugation in Fig. 6.5(b), the circularly-corrugated flares feed identical cylindrical
waves on the reflector regardless of the feed positions due to their rotational
symmetry.

From literature [Sil49], it is known that the performance of the cylindrical
parabolic reflector antenna depends on the fact that the reflector of the main
beam shaper is in the cylindrical wave cone of the source. In the dual reflector
system, the first small reflector plays a role in changing a wave from the primary
feed into a cylindrical wave. On the other hand, in this novel reflector system,
the corrugated flares are used in order to feed a cylindrical wave on the reflector,
the main beam shaper. Therefore, the entire reflector antenna has not only
good performance, but also keeps compact and stable since only the little flares
will be extended to the APWLL. It should be mentioned that the idea of
using the corrugated flares and a single offset cylindrical parabolic reflector is
presented for the first time in this work.

Also, the performance of the entire antenna in elevation is mostly subject to
both the flares and the reflector. Therefore, in order to predict the performance
of the entire antenna and design an optimal reflector, in the following section,
the far fields of the entire antenna are derived.

cylindrical parabolic reflector

elevation

cylindrical wave

corrugated flare

focal line

APWLL

z

y x

(a)

cylindrical parabolic reflector

APWLL

feed horn

(b)

cylindrical parabolic reflector

APWLL

feed horn

(c)

Figure 6.5: Entire offset cylindrical parabolic reflector antenna with symmetric corrugated flares. (a) Side view. (b) Front view of the antenna extended by circularly-corrugated flares and (c) by linearly-corrugated flares.

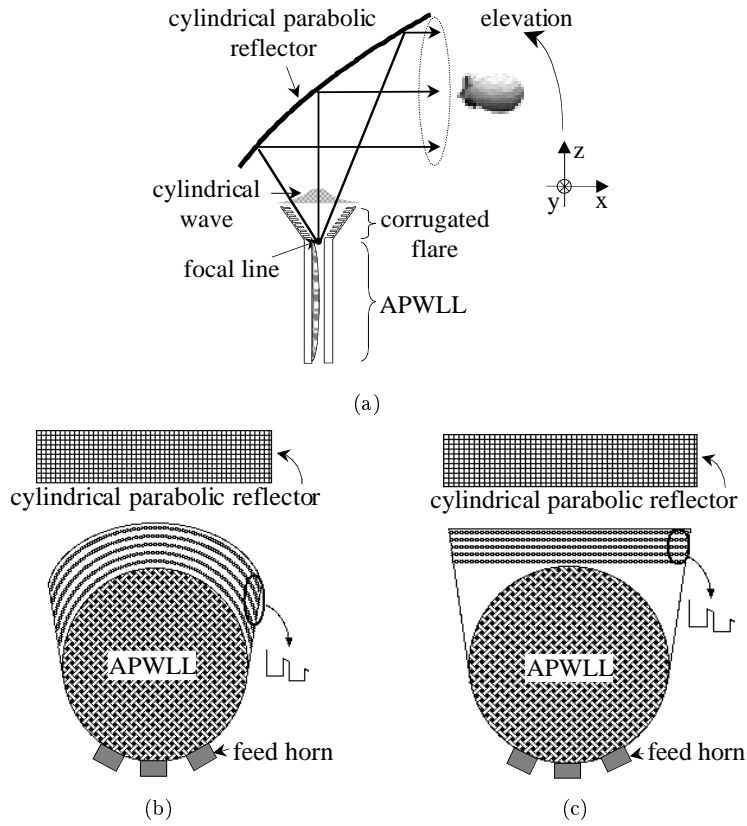## 6.2.2 Far-field calculation of offset cylindrical parabolic reflector

In Fig. 6.6, the geometry of the offset cylindrical parabolic reflector for calculating far fields is illustrated. The focal point is located on the $x-$axis, $F_a(F,0,0)$. $F_e(F + \delta_x,0,\delta_z)$ is a point which is deviated from the focal point to δ_x in the x direction and δ_z in the z direction. This is used later to investigate off-axis operation such as the calculation of far field at a beam scan angle. An arbitrary point of the parabola is given as $Q(x,0,z)$. The length and the angle between the focal point F_a and the point Q are R_a and ζ, respectively. The differential increment of the angle ζ is $d\zeta$. Two angles of $\zeta_1 (< 0)$ and $\zeta_2 (> 0)$ determine the lowest point (x_1,z_1) and the highest point (x_2,z_2), respectively. D_a is the projected cylindrical parabolic length and using Eq. (D.3) in appendix D is given as

$$D_a = z_2 - z_1 = 2F \left(\frac{\cos(\zeta_2)}{1 - \sin(\zeta_2)} - \frac{\cos(\zeta_1)}{1 - \sin(\zeta_1)} \right). \tag{6.1}$$

Eq. (6.1) also shows that if the three variables of ζ_1, ζ_2, and D_a are given, the focal point length F is known, so that a cylindrical parabolic reflector is designed.

Practically, if the reflector is small, the amount of rays which isn't reflected by the reflector, called spillover effect, increases. For a lower spillover, that is, a high efficiency at least the following two conditions should be fulfilled. First, the length D_a is bisected at the point P. Second, the angle ζ_1 is large enough to make almost all energy from the flares reflected. Usually, the angle $\theta_{10\,dB}$, at which the power of the feed radiates $10\,dB$ below from the bore sight of the feed is taken as ζ_1 [Miz76], [Rus90], [Bro93], [Lee95].

The first condition of bisection at the point P results in $D_a = 2(2F - z_1)$ and hence z_2 is determined by D_a and z_1 or F and z_1 as follows:

$$z_2 = D_a + z_1 = 4F - z_1. \tag{6.2}$$

Thus, with the first condition, a cylindrical parabolic reflector is fixed by only two variables ζ_1 and one of both D_a and F. The relation of D_a and F is

$$F = \frac{D_a}{4} \cdot \left(1 - \frac{\cos(\zeta_1)}{1 - \sin(\zeta_1)} \right)^{-1}. \tag{6.3}$$

6.2.2.1 Aperture field of the reflector

$S_1(y,\zeta)$ is the energy distribution per unit angle area in the pattern of the feed and $S_2(y,z)$ is the energy distribution per unit area at the aperture. In the same
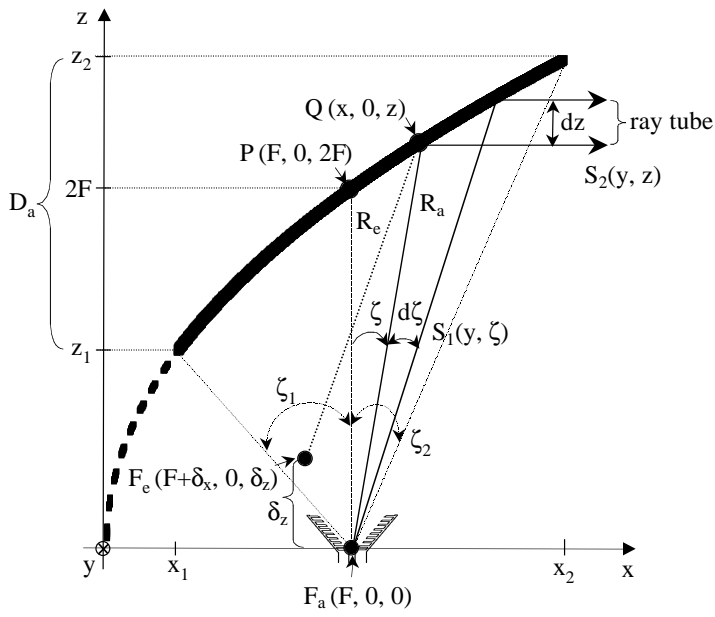
Figure 6.6: The schematic diagram of the offset cylindrical parabolic reflector for the calculation of far fields.

way as the calculation of the lens aperture field in Sec 4.2.2, the energy flows through a ray tube at the feed, $S_1(y,\zeta)dyd\zeta$ and at the aperture, $S_2(y,z)dydz$ are

$$S_1(y,\zeta)dyd\zeta = |\underline{E}_1(y)|^2|\underline{E}_1(\zeta)|^2dyd\zeta \qquad (6.4a)$$
$$S_2(y,z)dydz = |\underline{E}_2(y)|^2|\underline{E}_2(z)|^2dydz. \qquad (6.4b)$$

Since the energy flow keeps constant through various cross sections normal to the tube,

$$S_1(y,\zeta)dyd\zeta = S_2(y,z)dydz. \qquad (6.5a)$$

From Eq. (6.4), simplifying Eq. (6.5a) results in

$$|\underline{E}_1(\zeta)|d\zeta = |\underline{E}_2(z)|dz. \qquad (6.5b)$$

$|\underline{E}_1(\zeta)|$ is a far field of the corrugated flares in elevation and $d\zeta$ is derived in appendix D. Therefore, the field distribution at the aperture $|\underline{E}_2(z)|$ is

$$|\underline{E}_2(z)| = \frac{1 - \sin(\zeta)}{2F}|\underline{E}_1(\zeta)|. \tag{6.5c}$$

For instance, the far field of the corrugated flares for a $20°$ HPBW is considered as $|\underline{E}_1(\zeta)|$. Figure 6.7(a) shows the far-field pattern of the corrugated flare. The angle $\theta_{10\,\mathrm{dB}}$ is $23.4°$, so that the angle $\zeta_1 = -23.4°$. Figure 6.7(b) shows the field distribution at the reflector aperture. In calculation, the reflector length D_a is $9.3\lambda_0$ and then Eq. (6.3) leads to the focal point length of $F = 6.8\lambda_0$.

For the purpose of beam scanning, the focal point is moved and is located
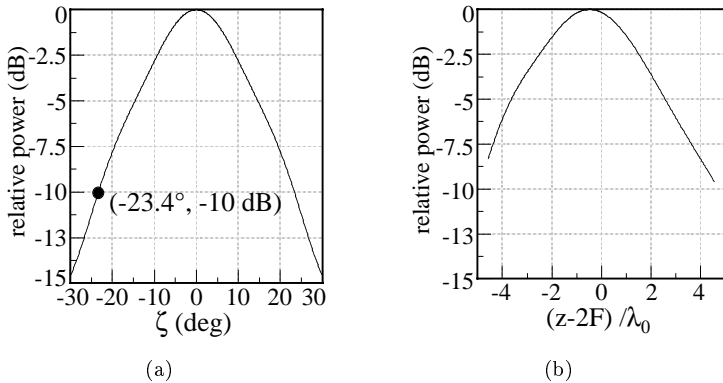
Figure 6.7: (a) Far field of the corrugated flares fabricated for $20°$ HPBW in Ch 5. (b) Field distribution at the reflector aperture using Eq. (6.5c).

on the off-axis. This causes phase errors at the aperture. Therefore, the effect of phase errors should be added to the amplitude term in Eq. (6.5c) in order to predict far fields at a beam scan angle. From the new focal point F_e, the distance between F_e and Q is

$$R_\mathrm{e} = \sqrt{(F + \delta_x - \frac{z^2}{4F})^2 + (z - \delta_z)^2} \tag{6.6}$$

where z is given by the angle ζ in Eq. (D.3) in appendix D. Using Eq. (D.2c), the total distance between the original focal point F_a and the new focal point F_e is

$$r_\mathrm{e} = R_\mathrm{a} - R_\mathrm{e}. \tag{6.7}$$

Therefore, the complete electric field at the aperture including the phase error is

$$\vec{E}_2(y,z) = \hat{z}|\underline{E}_2(y)||\underline{E}_2(z)|e^{jk_0 r_e} \tag{6.8}$$

where $|\underline{E}_2(y)|$ is given as $|\underline{E}_a(y)|$ in Eq. (4.9).

With the aid of Eqs. (6.6) and (6.7), the phase error caused by focal point deviation is investigated. In Fig. 6.8, the phase error $k_0 r_e$ and the amplitude in elevation are plotted for two different cases. First, Fig. 6.8(a) is for the movement in the x direction, $\delta_x = 0.8\lambda_0$, while $\delta_z = 0$. Second, Fig. 6.8(b) is for the movement in the z direction, $\delta_z = 0.7\lambda_0$, while $\delta_x = 0$.

6.2.2.2 Far-field calculation

Far-field patterns of the reflector are derived by the aperture field integration method [Stu81], [Bal97] using the aperture field given by Eq. (6.8). By applying the equivalent theorem on the aperture, only the equivalent electric current $\vec{\underline{M}}$ is considered. Therefore,

$$\vec{\underline{M}} = 2\vec{\underline{E}}_2(y,z) \times \hat{n} = 2\hat{y}|\underline{E}_2(y)||\underline{E}_2(z)|e^{jk_0 r_e} \tag{6.9}$$

where $\hat{n}$ is the outward unit vector normal to the aperture, so that $\hat{n} = \hat{x}$. Similar to the far-field calculation of the lens in appendix B, the far fields of the reflector are

$$\underline{E}_\theta = -\frac{jk_0 e^{-jk_0 r}}{4\pi r} \int_y \int_{z_1-2F}^{z_2-2F} \underline{M}_y \cos(\psi) e^{jk_0(y'\sin(\theta)\sin(\psi)+z'\cos(\theta))} dz' dy' \tag{6.10a}$$

$$\underline{E}_\psi = \frac{jk_0 e^{-jk_0 r}}{4\pi r} \int_y \int_{z_1-2F}^{z_2-2F} \underline{M}_y \cos(\theta)\sin(\psi) e^{jk_0(y'\sin(\theta)\sin(\psi)+z'\cos(\theta))} dz' dy' \tag{6.10b}$$

with

$$\underline{M}_y = 2|\underline{E}_2(y)||\underline{E}_2(z)|e^{jk_0 r_e}. \tag{6.10c}$$

For the far-field pattern in E-plane, let $\psi = 0°$. Thus,

$$\underline{E}_\theta = -\frac{jk_0 e^{-jk_0 r}}{4\pi r} \int_y \int_{z_1-2F}^{z_2-2F} \underline{M}_y e^{jk_0 z'\cos(\theta)} dz' dy' \tag{6.11a}$$

$$\underline{E}_\psi = 0. \tag{6.11b}$$
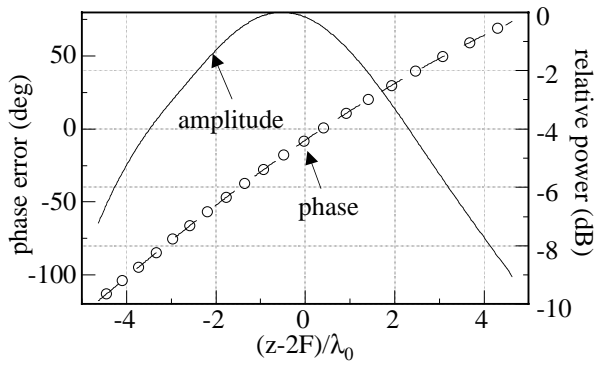
(a)
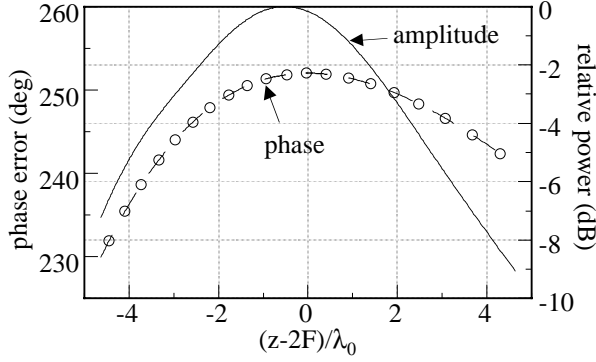
(b)

Figure 6.8: (a) Plot of phase error and amplitude for $\delta_x = 0.8\lambda_0$ and $\delta_z = 0$. (b) Plot of phase error and amplitude for $\delta_z = 0.7\lambda_0$ and $\delta_x = 0$.

Using Eq. (6.11), the far-field patterns are computed for the three cases in Figs. 6.7 and 6.8. The patterns are normalized. For $\delta_x = 0$ and $\delta_z = 0$, the reflector has a 6.2° HPBW in elevation and a first side lobe of about -22 dB. Thus, the beam factor is obtained as

$$BF_{\text{sim:ref}} = \theta_{\text{HPBW}} \times \frac{D_{\text{a}}}{\lambda_0} = 57.66°. \qquad (6.12)$$

For $\delta_x = 0.8\lambda_0$ and $\delta_z = 0$, the reflector has a 9.2° HPBW. The first side lobe level is lower than -33 dB. For $\delta_x = 0$ and $\delta_z = 0.7\lambda_0$, the reflector has a HPBW

of about 5.8°. The first side lobe level is about -15.5 dB. From the simulation, it can be found that the deviation in the x direction influences mostly a HPBW of the reflector whereas the deviation in the z direction influences mostly a first side lobe level of the reflector.
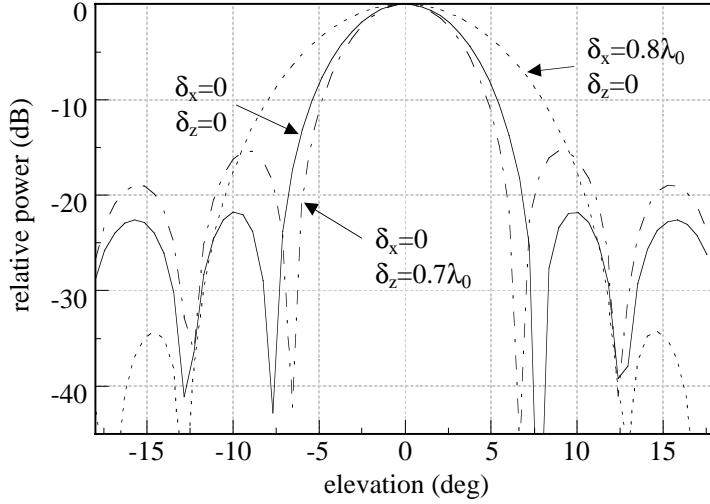
Figure 6.9: Calculated E-plane far-field patterns for the three cases in Figs. 6.7 and 6.8. Solid line is for $\delta_x = 0$ and $\delta_z = 0$.

6.2.3 Design and fabrication of an offset cylindrical parabolic reflector for the 76.5 GHz ACC radar

6.2.3.1 Determination of the reflector

In order to design a cylindrical parabolic reflector, the projected reflector length D_a and the angle ζ_1 are required as mentioned previously. Additionally, the width of the reflector in the y direction is required. As a first prototype, a reflector of about 5° HPBW in elevation and a 8° maximum scan angle in azimuth which satisfies the specification for the 76.5 GHz ACC radar in [Sch98] and [Wie01] is designed.

First, as shown in Eq. (6.12), the length D_a is determined by a desired HPBW. For a HPBW of 5.4°, $D_a = 11\lambda_0$ is calculated.

Second, to determine the angle ζ_1, the ratio of F and D_a is considered. As

described in [Lo60], [Ruz65], [Rus73], and [Kra88], higher ratio of F and D_a improves the tolerance of feed deviation (displacement). However, for higher ratio, a small $|\zeta_1|$ (a large aperture of the corrugated flare) is required (see Eq. (6.3), so that the flares become large. By considering the above effects, $|\zeta_1|$ is determined to 31°, and then the focal point length F is 24.8 mm from Eq. (6.3). As a result, the ratio of F and D_a is 0.57.

To design a corrugated flare for $\theta_{10\,\mathrm{dB}} = |\zeta_1| = 31°$, the design rules for
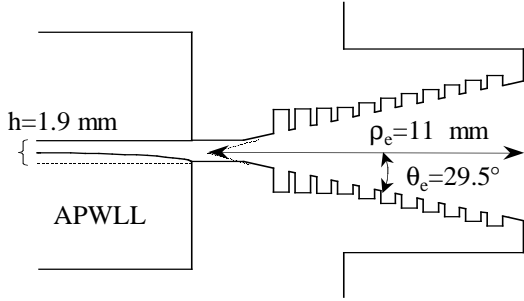
Figure 6.10: Side view of the corrugated flares for the $\theta_{10\,\mathrm{dB}}$=31°. The size of the corrugations is extremely exaggerated.

corrugated flares in Sec. 5.1.3 are used. The flare length $\rho_e = 11$ mm and the flare angle $\theta_e = 29.5°$ are selected. For the corrugations, the teeth width is 0.2 mm and the period between two teeth is 0.7 mm. Figure 6.10 shows the cross sectional view of the 11 mm corrugated flares. The total number of the corrugated flares amounts to 11.

Third, the width of the reflector w_{ref} is determined by considering a desired maximum scan angle. In Fig. 6.11, the schematic diagram is illustrated to determine the width. The angle α is a maximum scan angle. Also note that the unnecessary part of the flare (larger than $\alpha = 8°$) has been removed. To determine the width, it is assumed that the rays leaving the APWLL are confined to the aperture of the 50 mm APWLL, so that no fields out of the 50 mm length exist. Then, the width of the reflector is

$$w_{\mathrm{ref}} = 50 + 2\tan(\alpha) \cdot (2F + s_1). \tag{6.13}$$

As given previously, the desired maximum scan angle is $\alpha = 8°$, $s_1 = 25$ mm. The width of the reflector w_{ref} is determined to 70 mm.
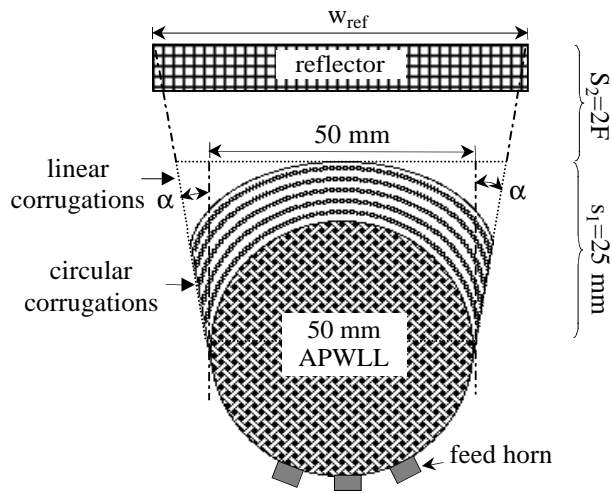
Figure 6.11: The schematic plot of the offset cylindrical parabolic reflector for the determination of the optimal reflector length w_{ref} depending on a desired maximum scan angle.

6.2.3.2   Fabrication

Figures 6.12(a) and 6.12(b) show the photograph of the linearly-corrugated flare and that of the circularly-corrugated flare, respectively. They are made of aluminum. Both of the flares are machined on a CNC milling machine. The 70 mm cylindrical parabolic reflector is shown in Fig. 6.12(c). The reflector is also made of aluminum and machined on the milling machine.

6.2.4   Experimental setup and measurement

In Fig. 6.13, the experimental setup is illustrated. The reflector is movable so that the deviation of the reflector from the focal line in the neighbor of the focal line is corrected. For the beam scan measurement, the feed horn connected with the mixer is rotated while both of the reflector and the APWLL antenna are fixed. In measurement, the 50 mm APWLL with the square lattice and square metal posts in Fig. 5.18 is used. The feed horn of 3.6 mm × 1.29 mm in Fig. 5.20 is used.

  Figure 6.14 shows measured and simulated far-field patterns of the APWLL antenna without the reflector in E-plane. The solid line shows the pattern
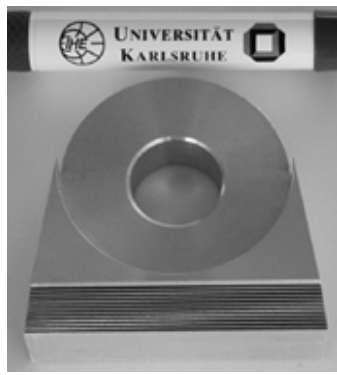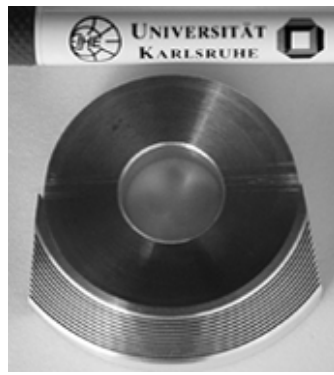
(a)   (b)
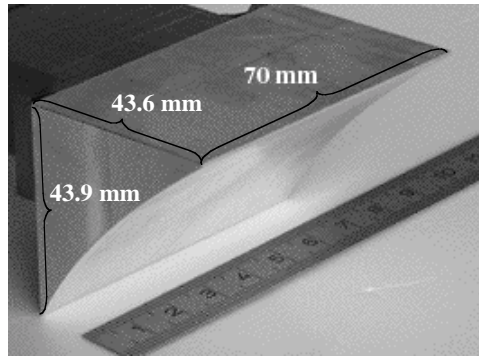
(c)

Figure 6.12: (a) Photograph of the linearly-corrugated flare. (b) Photograph of the circularly-corrugated flare. (c) Photograph of the 70 mm cylindrical parabolic reflector.

for the circularly-corrugated flare. It has 29° HPBW and $\theta_{10\,\mathrm{dB}}$=31°. For the linearly-corrugated flares (marked-dashed-dotted line), the HPBW is 28.4° and $\theta_{10\,\mathrm{dB}}$ is 34.2°. By comparing the simulation and the measurement, both of them are in good agreement although the HPBWs of two patterns are a bit higher.

In Fig. 6.15, measured H-plane far-field patterns of the entire reflector antenna for the circularly-corrugated flares are displayed. The antenna is measured at two different scan angles, 0° and 8°. It is seen that the pattern at 0°

(a)   (b)
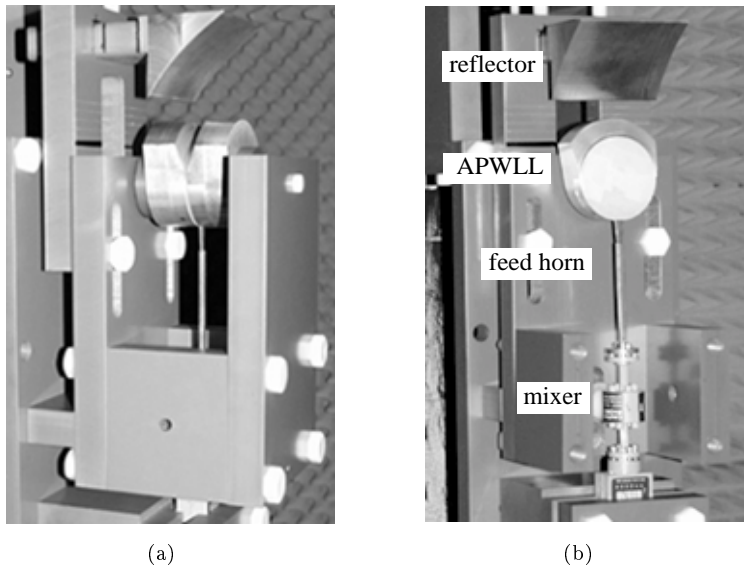
Figure 6.13: (a) Photograph of the measurement setup. (b) Photograph of the measurement setup without the upper plate of the APWLL.

has 2 dB higher gain than that at 8°. Both of the patterns have 4.75° HPBW and about -18.5 dB first side lobe. In other words, the deviation of the focal point have little influences on the H-plane pattern. The cross polarization at scan angle 0° is lower than -37 dB.

In Fig.6.16, measured and simulated E-plane far-field patterns are displayed. The calculation (dotted line) shows 5.4° HPBW whereas the measured (solid line) shows 4.8° HPBW. Therefore, the beam factor is

$$BF_{\text{mea:ref}} = \theta_{\text{HPBW}} \times \frac{D_{\text{a}}}{\lambda_0} = 53°. \tag{6.14}$$

In terms of side lobe level, the calculation is about 2.5 dB lower than the measurement. The minimal differences of HPBW and side lobe level is due to the usage of the approximate far field of the flares. The measured pattern is also displayed in expanded scale. Spillover effect is found at about 50°. The antenna gain of 30.3 dBi is measured.

In Fig. 6.17, the influence of focal line movement on E-plane radiation patterns is investigated. In order to compare each pattern, they are normalized whereas the gain of the pattern at scan angle 0° is 2 dB higher than that at 8°
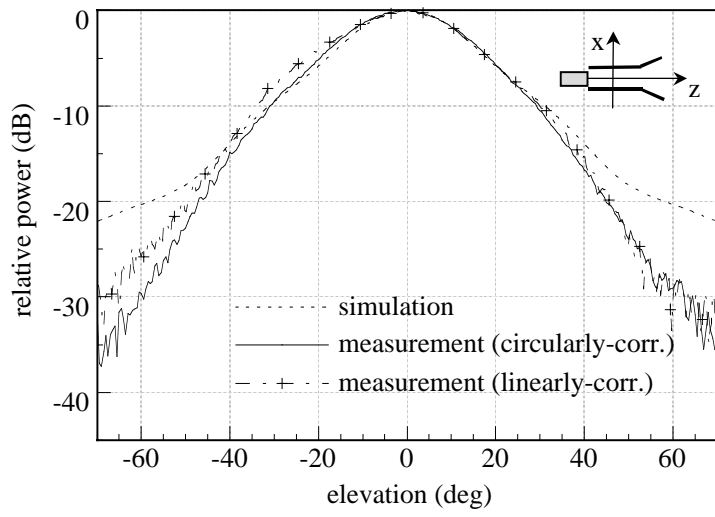
Figure 6.14: Simulated (dotted line) and measured far-field patterns without the reflector and with the circularly- and linearly-corrugated flares in elevation.
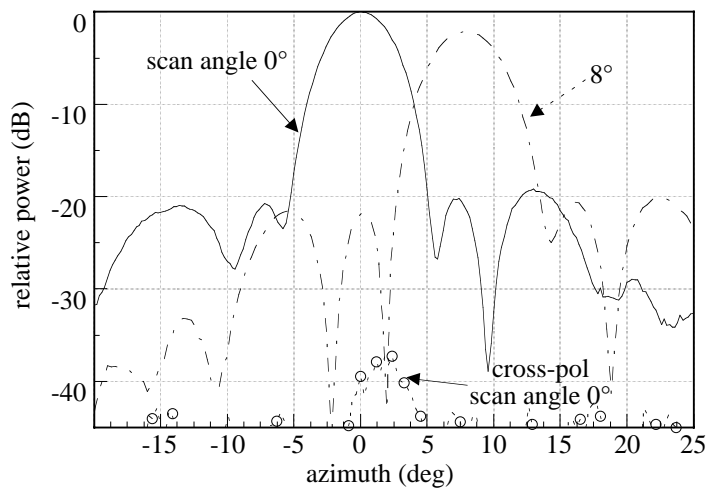
Figure 6.15: Measured *H*-plane far-field patterns with the reflector and with the **circularly**-corrugated flares for scan angles 0° and 8°.

Figure 6.16: Measured and simulated E-plane far-field patterns with the reflector and with the **circularly**-corrugated flares. Cross polarization is measured at scan angle $0°$. The measured pattern is also plotted in expanded scale.

as described previously. The gain of the pattern at scan angle $0°$ is also $0.4\,\mathrm{dB}$ higher than that for $\delta_x = 0$ and $\delta_z = \lambda_0$. In terms of the side lobe levels, the behavior is clearly different. The movement of focal point in the z direction leads to higher side lobe level (see the marked-dashed-dotted line). This result is also shown in Fig. 6.9. However, compared with the pattern of scan angle $8°$, the side lobe levels are nearly the same except but the $2\,\mathrm{dB}$ gain loss.

In order to compare the performance between the circularly-corrugated and the linearly-corrugated flare, the entire antenna equipped with the linearly-corrugated flare in Fig. 6.12(a) is measured. The measurement is plotted in Fig. 6.18. The simulated pattern is the same that in Fig. 6.16. The measured pattern points out $4.8°$ HPBW and $-18.5\,\mathrm{dB}$ first side lobe level. The measurement shows that the shape of the corrugation has little effect on the performance of the entire antenna.

Conclusively, it is shown that using of a cylindrical parabolic reflector instead of corrugated flares, high resoltuion in elevation is achieved with the complete antenna still compact. Also, the usage of a new type of the circularly-corrugated flares is presented and its good ability is shown. The design pro-
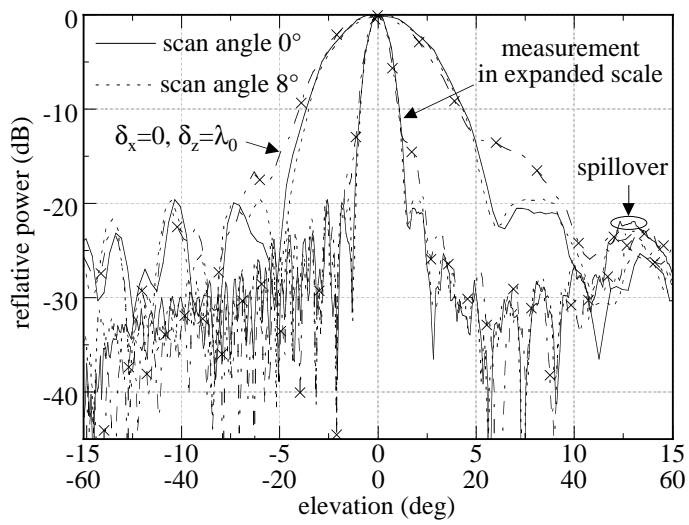
Figure 6.17: Influence of the displacement of the focal point on E-plane far-field patterns with the reflector and with the **circularly**-corrugated flares. The patterns are also plotted in expanded scale.

cedure of the complete antenna is given and very helpful for the design of the general parallel-plate Luneburg lens antenna with an offset reflector. In Fig. 6.19, the complete offset cylindrical parabolic reflector antenna for the 76.5 GHz ACC radar is displayed.
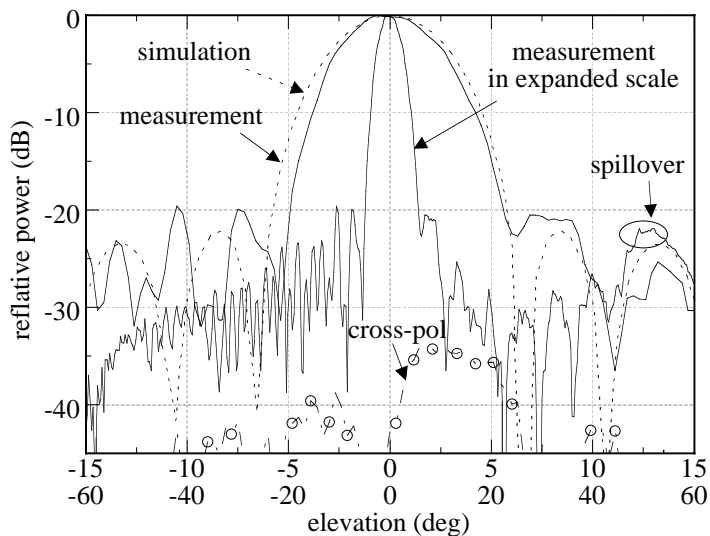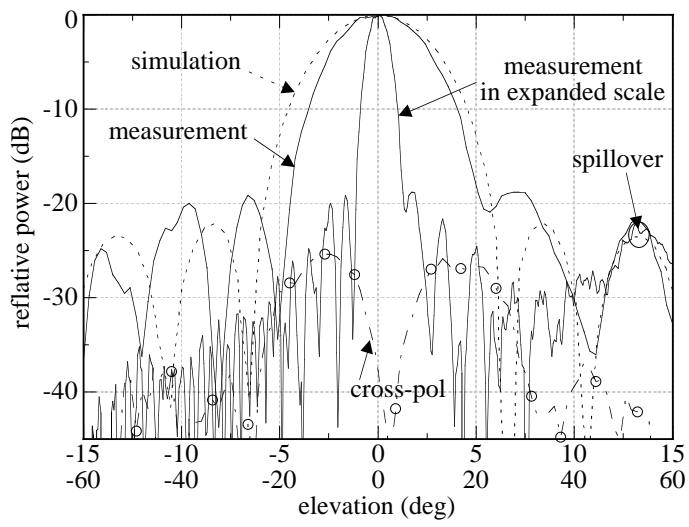
Figure 6.18: Measured and simulated *E*-plane far-field patterns with the reflector and with the **linearly**-corrugated flares. Cross polarization is measured at scan angle 0°. The measured pattern is also plotted in expanded scale.

Figure 6.19: The entire offset cylindrical parabolic reflector antenna for the 76.5 GHz ACC radar.

Chapter 7

Conclusion

Two new antennas using Luneburg lenses were presented for an adaptive cruise control (ACC) radar at 76.5 GHz. First, an asymmetric parallel-plate waveguide Luneburg lens (APWLL) antenna using two metallic PBG structures of a metal post structure and a corrugated surface was presented. Second, a single offset cylindrical parabolic reflector antenna fed by an APWLL antenna was presented.

The major contributions of this work can be summarized as follows:

First, two different properties of PBG structures of guiding and suppressing surface waves were studied. To explain the properties, two metallic PBG structures of a metal post structure and a corrugated surface in a parallel-plate waveguide were analyzed using the transmission line theory and the transverse resonance method. The metal post structure was shown to be isotropic but the corrugated surface is anisotropic while both structures are able to support arbitrary surface impedance. For the isotropy of the metal post structure, new lattices and shapes of metal post were found.

Second, using the two metallic PBG structures, a new APWLL antenna for automotive radar and communication applications was presented. The antenna is composed of an APWLL, rotationally symmetric corrugated flares, and a primary feed. The far fields of the antenna were derived by GO and the aperture field integration method. The design procedures of the antenna were described in Ch. 4.

With the aid of HFSS, the performances of the metal post structure for different lattices and metal post shapes were evaluated and verified at 76.5 GHz. It was found that the APWLL with a hexagonal lattice and circular metal posts

117

has the best performance.

By measurement, the design rules and the simulation results were verified at 76.5 GHz in Ch. 5. It was also shown that the APWLL antenna has really a wide scan angle, low side lobe levels, and relative broad band behavior. The most important advantages is that the APWLL antenna has nearly same performance, regardless of the feed position, that is, the antenna is used as a multiple beam antenna (MBA). Since the metallic PBG structures, namely the metallic artificial dielectrics were used, the complete antenna was capable of being made of metal. This metal fabrication makes the antenna not only durable in a car but also producible in low cost with the aid of proper fabrication method such as a precise metal cast [Woe98].

Last, using a single offset cylindrical parabolic reflector and an APWLL antenna, a prototype antenna for the 76.5 GHz ACC radar was made and measured in Ch. 6. The measurements showed that the antenna has a relatively wide scan angle. Also, using the reflector and the corrugated flares, the total dimension of the antenna was reduced and the efficiency of the antenna was enhanced, especially compared with the case of the usage of the large corrugated flares. Thus, it was shown that the antenna was able to satisfy the hard requirements for the 76.5 GHz ACC radar. It should be pointed out that the usage of a single offset cylindrical parabolic reflector for a parallel-plate waveguide Luneburg lens is reported for the first time.

Conclusively, the two antennas are excellent candidates for not only the 76.5 GHz ACC radar but also other automotive radar applications, especially, due to the low cost production and the properties of multiple beam and a wide scan angle. Furthermore, for the APWLL antenna, the useful properties of the multiple beam and a wide scan angle are applied for point-to-multipoint communications.

Appendix A

tanh(x)

Here a hyperbolic tangent function is derived from a tangent function to calculate the surface impedance in Ch. 3.

Let $x = k_{x1}(h - t)$ in Eq. (3.9),

$$\tan(k_{x1}(h - t)) = \tan(x) = \frac{\sin x}{\cos x} = -j\frac{e^{jx} - e^{-jx}}{e^{jx} + e^{-jx}}. \tag{A.1}$$

Using $k_{x1} = jk_0\sqrt{n^2 - 1}$ given in Eq. (3.11), $x = jk_0\sqrt{n^2 - 1}(h - t) = j|x|$. Thus

$$\tan(x) = -j\frac{e^{-|x|} - e^{|x|}}{e^{-|x|} + e^{|x|}} = j\tanh(|x|). \tag{A.2}$$

As a result,

$$\tan(k_{x1}(h - t)) = j\tanh(k_0\sqrt{n^2 - 1}(h - t)). \tag{A.3}$$

As an example, $n' = \sqrt{2 - r'^2}$ in Eq. (4.1) is put in the hyperbolic tangent function. The result is

$$\tanh(|x|) = \tanh\left(\frac{2\pi}{\lambda_0}\sqrt{1 - r'^2}(h - t)\right). \tag{A.4}$$

The behavior of the hyperbolic tangent function is plotted for $r' = 0$ in Fig. A.1.
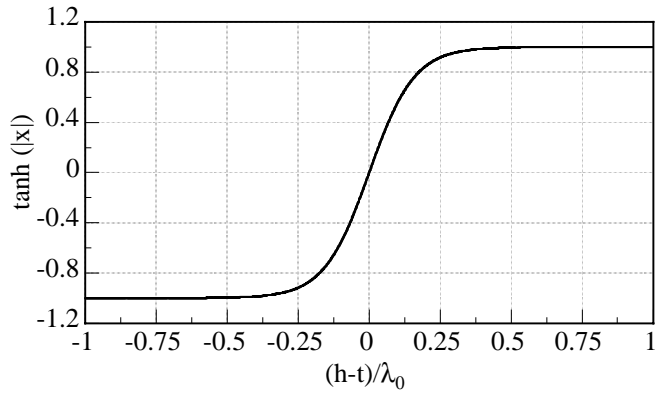
Figure A.1: Behavior of the hyperbolic tangent function for $r' = 0$.

Appendix B

Far-field calculation of a parallel-plate Luneburg lens
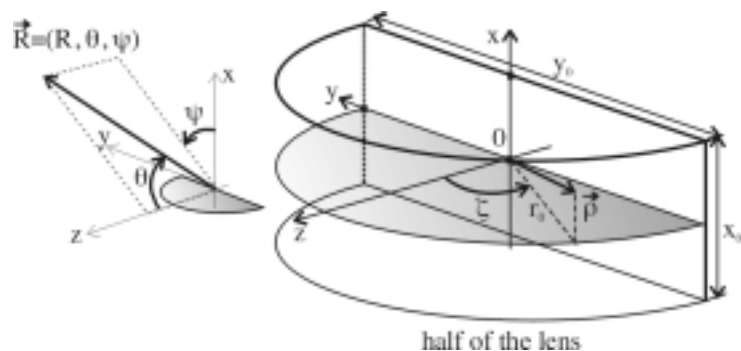
Figure B.1: Geometry of a parallel-plate Luneburg lens for the far-field calculation.

In Fig. B.1, the real aperture of the lens is displayed. Now using the aperture fields given in Eqs. (4.11a) and (4.11b), the equivalent magnetic and electric currents on the aperture, $\vec{\underline{J}}$ and $\vec{\underline{M}}$ are obtained. They are

$$\vec{\underline{J}} \quad = \quad \hat{n} \times \vec{\underline{H}}_a = -\frac{1}{\eta_0} \cos(\zeta) \underline{E}_a(x,y) \hat{x} \qquad \text{(B.1a)}$$

$$\vec{\underline{M}} \quad = \quad -\hat{n} \times \vec{\underline{E}}_a = -\underline{E}_a(x,y) \left(\cos(\zeta) \hat{y} + \sin(\zeta) \hat{z} \right). \qquad \text{(B.1b)}$$

121

The vector $\hat{n}$ is the outward unit vector normal to the aperture. It is given as

$$\hat{n} = -\sin(\zeta)\hat{y} + \cos(\zeta)\hat{z}.$$

With Eq. (B.1), vector magnetic and electric potentials, $\vec{\underline{A}}$ and $\vec{\underline{F}}$, are given.

$$\vec{\underline{A}} = \frac{\mu_0 r_0 e^{-jk_0 R}}{4\pi R} \int_{-\frac{x_0}{2}}^{\frac{x_0}{2}} \int_{-\frac{\pi}{2}}^{\frac{\pi}{2}} \vec{\underline{J}} e^{jk_0 \hat{e}_r \cdot \vec{\rho}} dx d\zeta = \underline{A}_r \hat{e}_r + \underline{A}_\theta \hat{e}_\theta + \underline{A}_\psi \hat{e}_\psi$$

$$\underline{A}_r = -\frac{\sqrt{\varepsilon_0 \mu_0} r_0 e^{-jk_0 R}}{4\pi R} \int_{-\frac{x_0}{2}}^{\frac{x_0}{2}} \int_{-\frac{\pi}{2}}^{\frac{\pi}{2}} \cos(\zeta) \sin(\theta) \cos(\psi) \underline{E}_a(x,y) e^{jk_0 \hat{e}_r \cdot \vec{\rho}} dx d\zeta$$

$$\underline{A}_\theta = -\frac{\sqrt{\varepsilon_0 \mu_0} r_0 e^{-jk_0 R}}{4\pi R} \int_{-\frac{x_0}{2}}^{\frac{x_0}{2}} \int_{-\frac{\pi}{2}}^{\frac{\pi}{2}} \cos(\zeta) \cos(\theta) \cos(\psi) \underline{E}_a(x,y) e^{jk_0 \hat{e}_r \cdot \vec{\rho}} dx d\zeta$$

$$\underline{A}_\psi = \frac{\sqrt{\varepsilon_0 \mu_0} r_0 e^{-jk_0 R}}{4\pi R} \int_{-\frac{x_0}{2}}^{\frac{x_0}{2}} \int_{-\frac{\pi}{2}}^{\frac{\pi}{2}} \cos(\zeta) \sin(\psi) \underline{E}_a(x,y) e^{jk_0 \hat{e}_r \cdot \vec{\rho}} dx d\zeta$$

$$(\text{B.2a})$$

$$\vec{\underline{F}} = \frac{\varepsilon_0 r_0 e^{-jk_0 R}}{4\pi R} \int_{-\frac{x_0}{2}}^{\frac{x_0}{2}} \int_{-\frac{\pi}{2}}^{\frac{\pi}{2}} \vec{\underline{M}} e^{jk_0 \hat{e}_r \cdot \vec{\rho}} dx d\zeta = \underline{F}_r \hat{e}_r + \underline{F}_\theta \hat{e}_\theta + \underline{F}_\psi \hat{e}_\psi$$

$$\underline{F}_r = -\frac{\varepsilon_0 r_0 e^{-jk_0 R}}{4\pi R} \int_{-\frac{x_0}{2}}^{\frac{x_0}{2}} \int_{-\frac{\pi}{2}}^{\frac{\pi}{2}} \underline{E}_a(x,y)(\cos(\zeta)\sin(\theta)\sin(\psi)$$
$$+ \sin(\zeta)\cos(\theta)) e^{jk_0 \hat{e}_r \cdot \vec{\rho}} dx d\zeta$$

$$\underline{F}_\theta = -\frac{\varepsilon_0 r_0 e^{-jk_0 R}}{4\pi R} \int_{-\frac{x_0}{2}}^{\frac{x_0}{2}} \int_{-\frac{\pi}{2}}^{\frac{\pi}{2}} \underline{E}_a(x,y)(\cos(\zeta)\cos(\theta)\sin(\psi)$$
$$- \sin(\zeta)\sin(\theta)) e^{jk_0 \hat{e}_r \cdot \vec{\rho}} dx d\zeta$$

$$\underline{F}_\psi = -\frac{\varepsilon_0 r_0 e^{-jk_0 R}}{4\pi R} \int_{-\frac{x_0}{2}}^{\frac{x_0}{2}} \int_{-\frac{\pi}{2}}^{\frac{\pi}{2}} \underline{E}_a(x,y) \cos(\zeta) \cos(\psi) e^{jk_0 \hat{e}_r \cdot \vec{\rho}} dx d\zeta$$

$$(\text{B.2b})$$

where

$$\vec{\rho} = x\hat{x} - r_0\sin(\zeta)\hat{y} + r_0\cos(\zeta)\hat{z} \tag{B.3a}$$

$$\hat{e}_r = \sin(\theta)\cos(\psi)\hat{x} + \sin(\theta)\sin(\psi)\hat{y} + \cos(\theta)\hat{z} \tag{B.3b}$$

$$\hat{e}_r \cdot \vec{\rho} = x\sin(\theta)\cos(\psi) - r_0\sin(\zeta)\cdot\sin(\theta)\sin(\psi) + r_0\cos(\zeta)\cdot\cos(\theta). \tag{B.3c}$$

Since $\underline{\vec{A}}$ and $\underline{\vec{F}}$ are known, the far fields can be calculated [Bal97]

$$\underline{E}_\theta = -j\omega\underline{A}_\theta - j\omega\eta_0\underline{F}_\psi \tag{B.4a}$$

$$\underline{E}_\psi = -j\omega\underline{A}_\psi + j\omega\eta_0\underline{F}_\theta. \tag{B.4b}$$

Thus, using the results in Eq. (B.2), the far fields are obtained as

$$\underline{E}_\theta = \frac{jr_0k_0e^{-jk_0R}}{4\pi R}\int_{-\frac{x_0}{2}}^{\frac{x_0}{2}}\int_{-\frac{\pi}{2}}^{\frac{\pi}{2}}\underline{E}_a(x,y)\cos(\zeta)\cos(\psi)$$

$$(1+\cos(\theta))e^{jk_0\hat{e}_r\cdot\vec{\rho}}dxd\zeta \tag{B.5a}$$

$$\underline{E}_\psi = \frac{-jr_0k_0e^{-jk_0R}}{4\pi R}\int_{-\frac{x_0}{2}}^{\frac{x_0}{2}}\int_{-\frac{\pi}{2}}^{\frac{\pi}{2}}\underline{E}_a(x,y)(\cos(\zeta)\sin(\psi)(1+\cos(\theta))$$

$$-\sin(\theta)\sin(\zeta))e^{jk_0\hat{e}_r\cdot\vec{\rho}}dxd\zeta \tag{B.5b}$$

$$\underline{H}_\theta = -\frac{\underline{E}_\psi}{\eta_0} \tag{B.5c}$$

$$\underline{H}_\psi = \frac{\underline{E}_\theta}{\eta_0}. \tag{B.5d}$$

Appendix C

Far-field calculation of corrugated flares
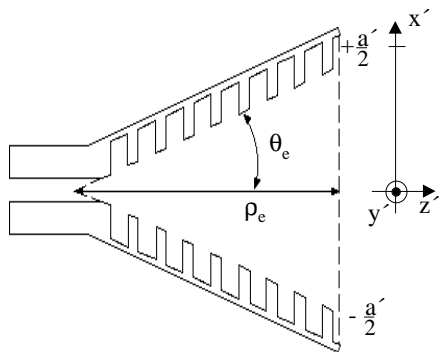
Figure C.1: Geometry of the corrugated flares for the aperture field calculation.

Referring to [Men76] and [Bal97], the aperture field is given as follows:

$$
\vec{\underline{E}}_a(x', y') \quad = \quad \hat{x}\underline{E}_{ax}(x', y') = \underline{E}_0 \cos \frac{\pi x'}{a'} \underline{E}_{ax}(y') e^{jk_0(\rho_e - \sqrt{\rho_e^2 + x'^2})} \hat{x}
$$

$$\tag{C.1a}$$

$$
\vec{\underline{H}}_a(x', y') \quad = \quad \frac{1}{\eta_0} \underline{E}_{ax}(x', y')\hat{y}
$$

$$\tag{C.1b}$$

where $\underline{E}_{ax}(y')$ is given by Eq. (4.9).

C.1 Far-field calculation

Now, the far field is derived using the aperture field with the aid of the aperture field integration method [Stu81]. That is,

$$\underline{E}_\theta \;=\; jk_0 \frac{e^{-jk_0 R}}{2\pi R}(\underline{P}_x \cos(\psi) + \underline{P}_y \sin(\psi)) \tag{C.2a}$$

$$\underline{E}_\psi \;=\; jk_0 \frac{e^{-jk_0 R}}{2\pi R}\cos(\theta)(\underline{P}_y \cos(\psi) - \underline{P}_x \sin(\psi)) \tag{C.2b}$$

where

$$\underline{P}_x = \int_{y'} \int_{-\frac{a'}{2}}^{\frac{a'}{2}} \underline{E}_{ax}(x',y') e^{jk_0(x' u_e + y' u_h)} dx' dy' \tag{C.2c}$$

$$\underline{P}_y = \int_{y'} \int_{-\frac{a'}{2}}^{\frac{a'}{2}} \underline{E}_{ay}(x',y') e^{jk_0(x' u_e + y' u_h)} dx' dy' \tag{C.2d}$$

$$\underline{E}_{ax}(x', y') = \cos\frac{\pi x'}{a'} \underline{E}_{ax}(y') e^{jk_0 (\rho_e - \sqrt{\rho_e^2 + x'^2})} \tag{C.2e}$$

$$\underline{E}_{ay}(x', y') = 0 \tag{C.2f}$$

$$u_e = k_0 \sin(\theta)\cos(\psi), \;\; u_h = k_0 \sin(\theta)\sin(\psi). \tag{C.2g}$$

With $\rho_e \gg a'$, $k_0(\rho_e - \sqrt{\rho_e^2 + x'^2})$ approximates to $\left(k_0 \frac{x'^2}{2\rho_e}\right)$. Thus,

$$\underline{P}_x = E_0 \underbrace{\int_{-\frac{a'}{2}}^{\frac{a'}{2}} \cos(\frac{\pi}{a'} x') e^{-jk_0 \frac{x'^2}{2\rho_e}} \cdot e^{jk_0 u_e} dx'}_{A} \cdot \underbrace{\int_{y'} \underline{E}_{ax}(y') e^{jk_0 u_h} dy'}_{B}. \tag{C.3}$$

To obtain $\underline{P}_x$, the entire integral is divided into two parts. First,

$$
\begin{aligned}
\underline{A} \;&=\; \frac{1}{2} \int_{-\frac{a'}{2}}^{\frac{a'}{2}} \left(e^{j\frac{\pi x'}{a'}} + e^{-j\frac{\pi x'}{a'}}\right) \cdot e^{-jk_0 \frac{x'^2}{2\rho_e}} \cdot e^{ju_e x'} dx' \\
&=\; \frac{1}{2}\sqrt{\frac{\pi \rho_e}{k_0}} \left[e^{j\frac{\rho_e}{2k_0}\left(\frac{\pi}{a'} + u_e\right)^2} \int_{t_2'}^{t_2} e^{-j\frac{\pi}{2}t^2} dt + e^{j\frac{\rho_e}{2k_0}\left(\frac{\pi}{a'} - u_e\right)^2} \int_{s_2'}^{s_2} e^{-j\frac{\pi}{2}s^2} ds \right]
\end{aligned}
\tag{C.4a}
$$

where

$$t_2 = \sqrt{\frac{k_0}{\pi \rho_e}} \left(\frac{a'}{2} - \frac{\rho_e}{k} \left(\frac{\pi}{a'} + u_e \right) \right) \tag{C.4b}$$

$$t_2' = \sqrt{\frac{k_0}{\pi \rho_e}} \left(-\frac{a'}{2} - \frac{\rho_e}{k} \left(\frac{\pi}{a'} + u_e \right) \right) \tag{C.4c}$$

$$s_2 = \sqrt{\frac{k_0}{\pi \rho_e}} \left(\frac{a'}{2} + \frac{\rho_e}{k_0} \left(\frac{\pi}{a'} - u_e \right) \right) \tag{C.4d}$$

$$s_2' = \sqrt{\frac{k_0}{\pi \rho_e}} \left(-\frac{a'}{2} + \frac{\rho_e}{k_0} \left(\frac{\pi}{a'} - u_e \right) \right). \tag{C.4e}$$

In Eq. (C.4a), Fresnel integrals are contained. Therefore, Eq. (C.4a) is expressed by

$$\underline{A} = \frac{1}{2} \sqrt{\frac{\pi \rho_e}{k_0}} \left[e^{j \frac{\rho_e}{2 k_0} \left(\frac{\pi}{a'} + u_e \right)^2} \left(C(t_2) - j S(t_2) - C(t_2') + j S(t_2') \right) + \right.$$
$$\left. e^{j \frac{\rho_e}{2 k_0} \left(\frac{\pi}{a'} - u_e \right)^2} \left(C(s_2) - j S(s_2) - C(s_2') + j S(s_2') \right) \right] \tag{C.5a}$$

where

$$C(v) - j S(v) = \int_0^v e^{-j \frac{\pi}{2} u^2} du = \int_0^v \cos \left(\frac{\pi}{2} u^2 \right) du - j \int_0^v \sin \left(\frac{\pi}{2} u^2 \right) du. \tag{C.5b}$$

As a result, from Eqs. (C.2), (C.3), and (C.5a), the E-plane radiation pattern is simply obtained by letting $\psi = 0°$. That is,

$$\underline{E}_\psi = 0 \tag{C.6a}$$

$$\underline{E}_\theta = j k_0 \frac{e^{-j k_0 R}}{2 \pi R} \underline{E}_0 \underline{A} \cdot \underline{B} \Big|_{\psi = 0°} \tag{C.6b}$$

where

$$\underline{A} = \frac{1}{2} \sqrt{\frac{\pi \rho_e}{k_0}} \left[e^{j \frac{\rho_e}{2 k_0} \left(\frac{\pi}{a'} + k \sin(\theta) \right)^2} \left(C(t_2) - j S(t_2) - C(t_2') + j S(t_2') \right) \right.$$
$$\left. + e^{j \frac{\rho_e}{2 k_0} \left(\frac{\pi}{a'} - k_0 \sin(\theta) \right)^2} \left(C(s_2) - j S(s_2) - C(s_2') + j S(s_2') \right) \right]_{\psi = 0°} \tag{C.6c}$$

$$\underline{B} = \int_{y'} \underline{E}_{ax}(y') dy'. \tag{C.6d}$$

Note that for the E-plane radiation pattern, $\underline{B}$ is independent of the angle θ since $\underline{E}_{ax}(y')$ has no component of the angle θ.

C.2   Approximation of the Fresnel integrals

The approximation of the Fresnel integrals [Abr72] is

$$C(v) = \begin{cases} \frac{1}{2} + A(v)\sin\left(\frac{\pi}{2}v^2\right) - B(v)\cos\left(\frac{\pi}{2}v^2\right) & \text{if } v \geq 0 \\ -C(-v) & \text{if } v < 0 \end{cases} \tag{C.7a}$$

$$S(v) = \begin{cases} \frac{1}{2} - A(v)\cos\left(\frac{\pi}{2}v^2\right) - B(v)\cos\left(\frac{\pi}{2}v^2\right) & \text{if } v \geq 0 \\ -S(-v) & \text{if } v < 0 \end{cases} \tag{C.7b}$$

where

$$A(v) = \frac{1 + 0.926v}{2 + 1.792v + 3.104v^2} \tag{C.7c}$$

$$B(v) = \frac{1}{2 + 4.142v + 3.492v^2 + 6.67v^3}. \tag{C.7d}$$

Appendix D

Derivation of the relation between dz and $d\zeta$

Using the parabolic equation, $x^2 = 4Fz$ and Fig. 6.6, the y and z components of the point Q are

$$
\begin{align}
x &= F + 2R_\mathrm{a}\sin(\zeta) \tag{D.1a} \\
z &= 2\sqrt{Fx} = 2\sqrt{F(F + R_\mathrm{a}\sin(\zeta))}. \tag{D.1b}
\end{align}
$$

Thus, the distance R_a is

$$
R_\mathrm{a}^2 = (x - F)^2 + z^2 = (R_\mathrm{a}\sin(\zeta))^2 + 4F^2 + 4FR_\mathrm{a}\sin(\zeta). \tag{D.2a}
$$

Simplifying the above equation results in

$$
R_\mathrm{a}^2\cos^2(\zeta) - 4R_\mathrm{a}F\sin(\zeta) - 4F^2 = 0. \tag{D.2b}
$$

By solving Eq. (D.2b) for R_a,

$$
R_\mathrm{a} = \frac{2F}{1 - \sin(\zeta)}. \tag{D.2c}
$$

From Eq. (D.2c), Eq. (D.1b) is

$$
z = 2F\frac{\cos(\zeta)}{1 - \sin(\zeta)}. \tag{D.3}
$$

Thus, dz is obtained as

$$
dz = \frac{2F}{1 - \sin(\zeta)}d\zeta. \tag{D.4}
$$

References

[Abe00]   A. Abele, *Realisierung von Linsenantennen im mm-Wellenbereich*, Diploma Thesis, Universität Karlsruhe, Germany, 2000.

[Abr72]   M. Abramowitz and I. A. Stegun, Eds., *Handbook of Mathematical Functions*, Dover Publications, New York, 9th ed., 1972.

[All98]   S. W. Alland, "Antenna requirements and architecture tradeoffs for an automotive forward looking radar", *IEEE National Radar Conference*, Dallas, USA, May 1998, pp. 367–372.

[Atn01]   ATNF SKA Working Document Index, Commonwealth scientific & industrial research organisation (CSIRO), Australia, http://www.atnf.csiro.au/SKA/techdocs/Catalogue.html, 2001.

[Bal97]   C. A. Balanis, *Antenna Theory*, John Wiley & Sons, NY, USA, 2nd ed., 1997.

[Bar01]   A. S. Barlevy and Y. Rahmat-Samii, "Characterization of electromagnetic band-gaps composed of multiple periodic tripods with interconnecting vias: concept, analysis, and design", *IEEE Transactions on Microwave Theory and Techniques*, vol. 49, no. 3, pp. 343–353, Mar. 2001.

[Bre00]   E. A. Bretz, "Technology 2000 Analysis & Forecast : Transportation", *IEEE Spectrum*, pp. 91–96, Jan. 2000.

[Bri48]   L. Brillouin, "Wave guides for slow waves", *Journal of Applied Physics*, vol. 19, pp. 1023–1041, 1948.

[Bro93]   E.R. Brown, C.D. Parker and E. Yablonovitch, "Radiation properties of a planar antenna on a photonic-crystal substrate", *Journal of the Optical Society of America B*, vol. 10, no. 2, pp. 404–407, Feb. 1993.

[Bul93]   D. L. Bullock, C.-C. Shih and R. S. Margulies, "Photonic band structure investigation of two-dimensional Bragg reflector mirrors for semiconductor laser mode control", *Journal of the Optical Society of America B*, vol. 10, no. 2, pp. 399–403, Feb. 1993.

[Chr95]   C. Christopoulos, *The Transmission-line Modeling Method: TRM*, IEEE Press, NJ, USA, 1995.

[Cla84]   P. J. B. Clarricoats and A. D. Olver, *Corrugated Horns for Microwave Antennas*, IEEE press, NY, USA, 1984.

[Col91]   R. E. Collin, *Field Theory of Guided Waves*, IEEE press, New York, USA, 2nd ed., 1991.

[Cul55]   L. F. Culbreth, M. W. Long and A. H. Schaufelberger, "Two-dimensional microwave Luneburg lenses", ASTIA No. 72211, Georgia Institute of Technology, Atlanta, 1955.

[Ehr75]   H. W. Ehrenspeck, "The short backfire antenna", *IEEE Proc.*, pp. 1138, Aug. 1975.

[Ell81]   R. S. Elliott, *Antenna Theory and Design*, Pentice-Hall, New Jersey, 1981.

[Eom01]   H. J. Eom, *Wave Scattering Theory*, Springer, Heidelberg, Germany, 2001.

[Gen98]   N. Geng and W. Wiesbeck, *Planungsmethoden für die Mobilkommunikation*, Springer, Ch2, 1998.

[Gon99]   R. Gonzalo, P. de Maagt and M. Sorolla, "Enhanced patch-antenna performance by suppressing surface waves using photonic-bandgap substrates", *IEEE Transactions on Microwave Theory and Techniques*, vol. 47, no. 11, pp. 2131–2138, Nov. 1999.

[Gre99]   A. D. Greenwood and J.-M. Jin, "A field picture of wave propagation in inhomogeneous dielectric lenses", *IEEE Antennas and Propagation Magazine*, vol. 41, no. 5, pp. 9–18, Oct. 1999.

[Han61]   P. W. Hannan, "Microwave antennas derived from the Cassegrain telescope", *IRE Transactions on Antennas and Propagation*, vol. AP-9, pp. 140–153, Mar. 1961.

[Han64]   R. C. Hansen, *Microwave Scanning Antennas (Volume 1)*, Academic Press, New York and London, pp. 224–233, 1964.

[Har61]   R. F. Harrington, *Time-Harmonic Electromagnetic Fields*, McGraw-Hill, 1961.

[Her00]   A. Herschlein, Y.-J. Park and W. Wiesbeck, "Parallel-plate Luneburg lens antenna with corrugated flares for ACC radar", *Diskussionsitzung über ANTENNEN für Mobile Systeme 2000*, Starnberg, Germany, Oct. 2000.

[Ing97]   P.G. Ingerson, "Luneberg lenses performance limitations due to fabrication process", *Proc. IEEE Int. Symp. on Antennas and Propagation AP-S'97*, Montreal, Canada, Jul. 1997, pp. 862–865.

[Ish91]   A. Ishimaru, *Electromagnetic Wave Propagation, Radiation, and Scattering*, Prentice Hall, NJ, USA, 1991.

[Joa95]   J. Joannopoulos, R. Meade and J. Winn, *Photonic Crystals:Molding the Flow of Light*, Princeton Univ. Press, Princeton, NJ, USA, 1995.

[Joh62]   R. C. Johnson, "The geodesic Luneburg lens", *Microwave Journal*, , no. 5, pp. 76–85, Aug. 1962.

[Joh84]   R. C. Johnson and H. Jasik, *Antenna Engineering Handbook*, New York, McGraw-Hill, 18-1 to 18-3, 1984.

[Joh93]   R. C. Johnson, *Antenna Engineering Handbook*, New York, McGraw-Hill, New York, USA, 3rd ed., 1993.

[Jon01]   W. D. Jones, "Keeping cars from crashing (cover story)", *IEEE Spectrum*, pp. 40–45, Sept. 2001.

[JOS93]   *Journal of the Optical Society of America B (Special Issue on photonic band gaps)*, vol. 10, no. 2, Feb. 1993.

[Kil90]   P.-S. Kildal, "Artificially soft and hard surfaces in electromagnetics", *IEEE Transactions on Antennas and Propagation*, vol. 38, no. 10, pp. 1537–1544, Oct. 1990.

[Kil00]   P.-S. Kildal, *Foundations of Antennas*, Studentliterature, Sweden, 2000.

[Kim98]   K.W. Kim and Y. Rahmat-Samii, "Spherical Luneburg lens antennas:engineering characterizations including air gap effects", *Proc. IEEE Int. Symp. on Antennas and Propagation AP-S'98*, Atlanta, Georgia, USA, Jun. 1998, pp. 2062–2065.

[Kin81]   R. J. King and K. S. Park, "Synthesis of surface reactances using a grounded pin bed structure", *Electronics Letters*, vol. 17, pp. 52–53, Jan. 1981.

[Kin83]   R. J. King, D. V. Thiel and K. S. Park, "The synthesis of surface reactance using an artificial dielectric", *IEEE Transactions on Antennas and Propagation*, vol. AP-31, no. 3, pp. 471–476, May 1983.

[Kli65]   M. Kline and I. Kay, *Electromagnetic Theory and Geometrical Optics*, Interscience, New York, USA, 1965.

[Kra88]   J. D. Kraus, *Antennas*, McGraw-Hill, NY, USA, 2nd ed., 1988.

[Kue64]   R. Kuehn, *Mikrowellenantennen*, Veb Verlag, Berlin, Germany, 1964.

[Law66]   R. E. Lawrie and JR. Leon Peters, "Modifications of horn antennas for low sidelobe levels", *IEEE Transactions on Antennas and Propagation*, vol. AP-14, pp. 605–610, Sept. 1966.

[Lee71]   S. Lee and W. Jones, "Surface waves on two-dimensional corrugated surfaces", *Radio Science*, vol. 6, pp. 811–818, 1971.

[Lee78]   S. W. Lee, Y. Rahmat-Samii and R. C. Menendez, "GTD, ray field, and comments on two papers", *IEEE Transactions on Antennas and Propagation*, vol. AP-26, no. 2, pp. 39–41, Mar. 1978.

[Lee94]   J. H. Lee, H. J. Eom, J. W. Lee and K. Yoshitomi, "Transverse electric mode scattering from rectangular grooves in parallel-plate", *Radio Science*, vol. 29, no. 5, pp. 1215–1218, 1994.

[Lee95]   Y.-H. Lee, K. W. Brown and A. Jr. Prata, *RASCAL version 2.1 manual*, Universtity of Southern California, CA, USA, 1995.

[Lo60]   Y. T. Lo, "On the beam deviation factor of a paraboloidal reflector", *IRE Transactions on Antennas and Propagation*, vol. AP-8, pp. 347–349, May 1960.

[Lov76]   A. W. Love, Ed., *Electromagnetic Horn Antennas*, IEEE Press, NY, USA, 1976.

[Lov78]   A. W. Love, Ed., *Reflector Antennas*, IEEE, NY, USA, 1978.

[Lun64]   R. K. Luneburg, *Mathematical Theory of Optics*, Berkeley: Univ. Califonia Press, Califonia, 1964.

[Mar51]   N. Marcuvitz, *Waveguide Handbook*, McGraw-Hill, New York, USA, 1951.

[McN90]   D. A. McNamara, C. W. I. Pistorius and J. A. G. Malherbe, *Introduction to the Uniform Geometrical Theory of Diffraction*, Artech House, Boston, USA, 1990.

[Mei95]   H. H. Meinel, "Commercial applications of millimeterwaves history, present status, and future trends", *IEEE Transactions on Microwave Theory and Techniques*, vol. 43, no. 7, pp. 1639–1653, Jul. 1995.

[Men74]   C. A. Mentzer and JR. Leon Peters, "Properties of cutoff corrugated surfaces for corrugated surfaces for corrugated horn design", *IEEE Transactions on Antennas and Propagation*, vol. AP-22, pp. 191–196, Mar. 1974.

[Men76]   C. A. Mentzer and JR. Leon Peters, "Pattern analysis of corrugated horn antennas", *IEEE Transactions on Antennas and Propagation*, vol. AP-24, no. 3, pp. 304–309, May 1976.

[Men99]   W. Menzel, D. Pilz and R. Leberer, "A 77-GHz FM/CW radar front-end with a low-profile low-loss printed antenna", *IEEE Transactions on Microwave Theory and Techniques*, vol. 47, no. 12, pp. 2237–2241, Dec. 1999.

[Miz76]   Y. Mizugutchi, M. Akagawa and H. Yokol, "Offset dual reflector antennas", *IEEE Antennas Propagat. Sco. Symp. Dig.*, Amherst, MA, Oct. 1976, pp. 2–5.

[Mos01]   H. Mosallael and Y. Rahmat-Samii, "Nonuniform Luneburg and two-shell lens antennas: radiation characteristics and design optimization", *IEEE Transactions on Antennas and Propagation*, vol. 49, pp. 60–69, Jan. 2001.

[MTT99]   *IEEE Transactions on Microwave Theory and Techniques*, vol. 47, Nov. 1999.

[MTT01]   *IEEE Transactions on Microwave Theory and Techniques (Special Issue on microwave and millimeter-wave photonics)*, vol. 49, no. 10, Oct. 2001.

[Olv92]   A. D. Olver, "Corrugated horns", *Electronics & Communication Engineering Journal*, pp. 4–10, Feb. 1992.

[Par00a]   A. J. Parfitt, J Graeme, J. Kot and P. Hall, "A case for the Luneburg lens as the antenna element for the square kilometre array radio telescope", *The Radio Science Bulletin*, , no. 293, pp. 32–37, Jun. 2000.

[Par00b]   Y.-J. Park, A. Herschlein and W. Wiesbeck, "Investigation and application of a photonic band gap structure for mm-wave antennas", *Diskussionsitzung über ANTENNEN für Mobile Systeme 2000*, Starnberg, Germany, Oct. 2000.

[Par01]   Y.-J. Park, A. Herschlein and W. Wiesbeck, "Application of rotationally symmetric corrugated flares to two-diemensional Luneburg lenses", *International Conference on Electromagnetics in Advanced Applications (ICEAA01)*, Torino, ITALY, Sept. 2001, pp. 459–462.

[Pee53a]   G.D.M. Peeler and D.H. Archer, "A two-dimensional microwave Luneberg lens", *IRE Transactions on Antennas and Propagation*, pp. 12–23, Jul. 1953.

[Pee53b]   G.D.M. Peeler, K.S. Kelleher and H. P. Coleman, *Virtual Source Luneburg Lens*, Nav. Res. Lab. Rep. 4115, 1953.

[Pee54]   G.D.M. Peeler, K.S. Kelleher and H.P. Coleman, "Virtual source Luneburg lenses", *IRE Transactions on Antennas and Propagation*, vol. AP-2, pp. 94–99, Jul. 1954.

[Per99]   M. Persson, F. Botling, E. Hesslow and R. Johansson, "Stop & go controller for adaptive cruise control", *IEEE International Conference on Control Applications*, Hawaii, USA, Aug. 1999, pp. 1692–1697.

[Pes01]   N. Yu Peskov and et al., "Electrodynamic properties of two-dimensional Bragg resonators of planar geometry", *Optics Communications 187*, pp. 311–317, Jan. 2001.

[Pho02]   Photonic & Sonic Band-Gap Bibliography, compiled by J. P. Dowling, JPL, et al., http://home.earthlink.net/ jpdowling/pbgbib.html, 2002.

[Poz93]   D. M. Pozar, *Microwave Engineering*, Addision-Wisley, ch. 2-4, 1993.

[Ra96]   J. W. Ra, *Electromagnetic Theory*, Daeyoung Sa, Seoul, Korea, 2nd ed., 1996.

[Raf96]   L. Raffaelli, "Millimeter-wave automotive radars and related technology", *IEEE Int. Microwave Symp. Dig.*, San Franciso, CA, USA, 1996, pp. 35–38.

[Rob98]   J. Robinson and et al., "A millimetric car radar front end for automotive cruise control", *IEE Colloquium on Automotive Radar and Navigation Techniques*, London, UK, Feb. 1998, pp. 9/1–9/8.

[Rud62]   R. C. Rudduck and C. H. Walter, "Luneberg lenses for space communications", *IRE Transactions on Space Electronics and Telemetry*, pp. 31–38, Mar. 1962.

[Rus73]   W. V. T. Rusch and A. C. Ludwig, "Determination of the maximum scan-gain contours of a beam-scanning paraboloid and their relation to the petzval surface", *IEEE Transactions on Antennas and Propagation*, vol. AP-21, pp. 141–147, Mar. 1973.

[Rus90]   W. Rusch, A. Jr. Prata and et al., "Derivation and application of the equivalent paraboloid for classical offset Cassegrain and Gregorian antennas", *IEEE Transactions on Antennas and Propagation*, vol. AP-38, no. 8, pp. 1141–1149, Aug. 1990.

[Ruz65]   J. Ruze, "Lateral-feed displacement in paraboloid", *IEEE Transactions on Antennas and Propagation*, vol. AP-13, pp. 660–665, Sept. 1965.

[San95]   J. Sanford and Z. Šipuš, "Sidelobe reduction with array fed spherical lenses", *Proc. IEEE Int. Symp. on Antennas and Propagation AP-S'95*, Newport Beach, CA, USA, Jun. 1995, pp. 670–673.

[Sch51]   S. A. Schelkunoff, *Electromagnetic Waves*, D. Van Nostrand Companny, New York, USA, 7th ed., 1951.

[Sch95]   H. Schrank and J. Sanford, "A Luneberg-lens update", *IEEE Antennas and Propagation Magazine*, vol. 37, no. 1, pp. 76–79, Feb. 1995.

[Sch98]   R. Schneider, *Modellierung der Wellenausbreitung für ein bildgebendes Kfz-Radar*, Ph.D. thesis, Universität Karlsruhe, Germany, 1998.

[Sco90]   C. Scott, *Modern Methods of Reflector Antenna Analysis and Design*, Artech House, 1990.

[Shu99]   J. D. Shumpert, W. J. Chappell and L. P. B. Katehi, "Parallel-plate mode reduction in conductor-backed slots using electromagnetic bandgap substrates", *IEEE Transactions on Microwave Theory and Techniques*, vol. 47, no. 11, pp. 2099–2104, Nov. 1999.

[Sie99]   D. Sievenpiper, L. Zhang, R.F. Jimenez Broas, N.G. Alexópolous and E. Yablonovitch, "High-impedance electromagnetic surfaces with a forbidden frequency band", *IEEE Transactions on Microwave Theory and Techniques*, vol. 47, no. 11, pp. 2059–2074, Nov. 1999.

[Sil49]   S. Silver, *Microwave Antenna Theory and Design*, McGraw-Hill, NY, USA, 1st ed., 1949.

[Sko80]   M. I. Skolnik, *Introduction to Radar Systems*, McGraw-Hill, Boston, USA, 2nd ed., 1980.

[Smi89]   A. C. Smith, S.E.J. Aglionby and D. A. Smith, "An innovative mobile satcom antenna", *Mechanical Aspects of Antenna Design, IEE colloquium*, 1989, pp. 9/1–9/7.

[Smi93]   D. R. Smith, R. Dalichaouch, N. Kroll and et al., "Photonic band structure and defects in one and two dimensions", *Journal of the Optical Society of America B*, vol. 10, no. 2, pp. 314–321, Feb. 1993.

[Sou96]   C. Soukoulis, Ed., *Photonic Band Gap Materials*, Kluwer, Norwell, MA, USA, 1996.

[Sta01]   Strassenverkehrsunfallbilanz 2000, Statistisches Bundesamt Deutschland, http://www.destatis.de/presse/deutsch/pm2001/p0620191.html,   Feb. 2001.

[Stu81]   W. L. Stutzman and G. A. Thiele, *Antenna Theory and Design*, John Wiley & Sons, New York, 1981.

[Stu98]   W. L. Stutzman, "Estimating directivity and gain of antennas", *IEEE Antennas and Propagation Magazine*, vol. 40, no. 4, pp. 7–11, Aug. 1998.

[Tai76]   C. T. Tai and C. S. Pereira, "An approximate formula for calculating the directivity of an antenna", *IEEE Transactions on Antennas and Propagation*, vol. AP-22, pp. 235–236, Mar. 1976.

[Tay55]   T. T. Taylor, "Design of lien source antennas for narrow beamwidth and low sidelobes", *IEEE Transactions on Antennas and Propagation*, vol. AP-3, pp. 16–28, Jan. 1955.

[Thu02]   Manfred Thumm, *Private Communication*, 2002.

[Ufi01]   P. Y. Ufimtsev and R. T. Ling, "New results for the properties of TE surface waves in absorbing layers", *IEEE Transactions on Antennas and Propagation*, vol. 49, no. 10, pp. 1445–1452, Oct. 2001.

[Vog82]   M. Vogel, *Theoretische und experimentalle Untersuchungen zur quasioptischen Abbildung mit Millimeterwellen, insbesondere mit Luneburg Linsen*, Fortschritt-Ber. VDI-Z., Reihe 10, no. 14, Germany, 1982.

[Vog83]   M. Vogel, "A new kind of planar waveguide Luneburg antenna for the mm-wave region", *Proc. European Microwave Conference EuMC'83*, 1983, pp. 413–418.

[Wal60]   C. H. Walter, "Surface-wave Luneburg lens antennas", *IEEE Transactions on Antennas and Propagation*, vol. AP-8, pp. 508–515, Sept. 1960.

[Wal65]   C. H. Walter, *Travelling Wave Antennas*, McGraw-Hill, New York, USA, 1965.

[Wen98]   J. Wenger, "Automotive mm-wave radar: status and trends in system design and technology", *IEE Colloquium on Automotive Radar and Navigation Techniques*, London, UK, Feb. 1998, pp. 1/1–1/7.

[Wie99]   W. Wiesbeck, *Hochfrequenztechnik II*, Universität Karlsruhe, Germany, *Hochfrequenztechnik II* lecture, 1999.

[Wie01]   W. Wiesbeck, *Automotive cruise control (ACC) and automotive microwaves*, Universität Karlsruhe, *Radar Systems* lecture, 2001.

[Woe98]   H. Woellmer, "Präzisionsguss von Mikroteilen aus Metall", *Nachrichten-Forschungszentrum Karlsruhe*, pp. 237–242, Mar. Jahrg.30, 1998.

[Wol97]   J. D. Woll, "Monopulse doppler radar for vehicle applications", *M & RF conference*, London, UK, 1997, pp. 234–238.

[Yab87]   E. Yablonovitch, "Inhibited spontaneous emission in solid-state physics and electronics", *Physical Review Letters*, vol. 58, no. 2, pp. 2059–2062, 1987.

[Yam96]   E. Yamashita, Ed., *Analysis Methods for Electromagnetic Wave Problems*, vol. 2, Artech House, Boston, USA, 1996.

[Yar84]   A. Yariv and P. Yeh, *Optical Waves in Crystals*, Wiley-Interscience, NJ, USA, 1984.

Curriculum Vitae

Persönliche Daten:

Name: Young-Jin Park

Geburtsdatum: 07. Januar 1971

Geburtsort: Ma-San, Südkorea

Staatsangehörigkeit: koreanisch

Familienstand: ledig

Schulbildung:

März 1977 - Feb. 1983   Grundschule in Ma-San, Südkorea

März 1983 - Feb. 1986   Gu-San Mittelschule in Ma-San

März 1986 - Feb. 1989   Chang-Shin High School in Ma-San

Wehr-oder Ersatzdienst:

April 1991 - Okt. 1992   Wehrdienst in Ma-San, Südkorea

Studium und Berufsweg:

März 1990 - Feb. 1997   Studium der Elektrotechnik an der Universität Chung-Ang, Seoul, Südkorea

März 1997 - Feb. 1999   Studium der Elektrotechnik zur Erlangung des Grades *Master of Science* am Korea Advanced Institute of Science and Technology (KAIST), Taejon, Südkorea

seit März 1999   Doktorand am Institut für Höchstfrequenztechnik und Elektronik der Universität Karlsruhe (TH) Stipendiat des *National Institute of International Education Development of Ministry of Education* Arbeitsgebiet:Kraftfahrzeug Radar und Entwicklung von Antennen für Kommunikation & Radaranwendungen in Millimeter-Bereich